

HYBRID GREEN COMPOSITES UTILIZING RENEWABLE LIGNOCELLULOSIC
FIBERS TO REINFORCE SOY-BASED RESINS

A Thesis

Presented to the Faculty of the Graduate School
of Cornell University

In Partial Fulfillment of the Requirements for the Degree of
Master of Science

by

Abdullah R A A Y Alkandary

August 2021

© 2021 Abdullah R A A Y Alkandary

ABSTRACT

Plant-based *green* composites have recently emerged as sustainable alternatives to petroleum-based polymer matrix composites (PMC) in applications such as transportation and packaging.

PMC techniques were employed to produce commercial-scale green composites made using one of the most wasted plant fibers, i.e., rice straw (RS). Thermoset resin sheets were prepared by denaturing soy protein isolate (SPI) and crosslinking it with glutaraldehyde. SPI resin was reinforced by hybrid RS/jute fabric (JFa) mats, to fabricate layered composites with high fiber content (up to 60%). Needle felting was used to interlace RS and JFa together and fabricate hybrid green PMC composites.

The hybrid composites were characterized for their moisture absorption, tensile properties, flexural properties, interfacial shear strength (IFSS), dynamic mechanical properties, fracture surface analyses, and thermal stability. The obtained results reflect the geometric complexity of these systems, their hygroscopic nature, and enable further utilization of fiber waste in low-mechanical resistant composites. Mechanical properties of all composites were affected by moisture absorption, except their ductility. Triple-layered composites with the lowest fiber content (40%) resulted in enhanced Young's modulus (E_y) and ultimate tensile strength (UTS), from 0.3 to 0.9 GPa and from 7.2 to 10.6 MPa, respectively, compared to pure resin. However, contrary to the logic, an inverse relationship was found between fiber content and each of the following: E_y and UTS; flexural modulus and ultimate flexural stress; and storage modulus. IFSS results as well as fracture analyses attributed this inverse relationship to the relatively weak fiber/resin interface, and to the deduction that fiber content has exceeded the resin's capacity of fully wetting the fibers. Moisture absorption in addition to the weak interfacial strengths were the primary reasons to lowering the mechanical resistance of the hybrid green composites. These hybrid composites can be used in many applications, from furniture to housing and from transportation to packaging.

BIOGRAPHICAL SKETCH

Abdullah was born in Bahrain on April 3rd, 1991, and raised in Kuwait City, Kuwait. He received his BS in nuclear engineering from Penn State, University Park, PA, in 2013. Later, he joined the Kuwait Institute for Scientific Research as a research associate in the Nanotechnology and Advanced Materials Program, where he worked on projects related to sustainable materials for energy and structural applications. After four years of research in materials science, he started his MS studies in materials science and engineering at Cornell University in August 2019. During his time at Cornell, he conducted his research on *green* composites in Netravali Research Group. He completed his MS in August 2021 and plans to pursue his PhD studies at Imperial College London, in the department of Aeronautics. There, he will be conducting research on advanced structural composites, particularly cellulose-reinforced lignin matrices, mimicking the chemistry of natural wood.

Dedicated to *Abdullah* 2013–2015;

ACKNOWLEDGMENTS

Cornell University is located on the traditional homelands of the Gayogohó:nø' (the Cayuga Nation). The Gayogohó:nø' are members of the Haudenosaunee Confederacy, an alliance of six sovereign Nations with a historic and contemporary presence on this land. The Confederacy precedes the establishment of Cornell University, New York state, and the United States of America. We acknowledge the painful history of Gayogohó:nø' dispossession, and honor the ongoing connection of Gayogohó:nø' people, past and present, to these lands and waters.

I wish to extend my gratitude to my advisor and mentor, Dr. Anil N. Netravali, for sharing his invaluable knowledge. Moreover, his guidance and never-ending support to my research, coursework, wellbeing, and academic career. I also want to thank my committee member, Dr. Shefford P. Baker, for the knowledge and skills I gained from his course entitled *Mechanical properties of materials, processing, and design*; in addition to the *SARS-CoV-2 Transmission Pathways* voluntary research activity. I appreciate all the support I have received from the Cornell community. Beginning with the faculty and administrators of both the Materials Science and Engineering (MSE) department and the Fiber Science department. The Digital Design and Fabrication Studio at the College of Human Ecology, particularly Charles V. Beach. Also, my colleagues at MSE and the Netravali Group.

I thank Kuwait Institute for Scientific Research for generously funding my master's degree. The Tata-Cornell Institute for funding all supplies needed to complete the Rice Straw research project and the Arizona State University Desert Arboretum Park for donating the palm fibers used in this research.

Last but not least, I want to thank my family, my chosen family, and my friends for their unconditional love and support from overseas.

TABLE OF CONTENTS

CHAPTER 1: INTRODUCTION	1
CHAPTER 2: BACKGROUND	7
2.1 Soy protein resins	7
2.2 Composition and structure of plant fibers	10
2.2.1 Cellulose	11
2.2.2 Hemicellulose	13
2.2.3 Lignin	14
2.2.4 Pectin	15
2.3 Treatment of natural fibers	15
2.4 Fibers used in this project	17
2.4.1 Jute	18
2.4.2 Rice straw fibers (RS)	19
2.4.3 Date palm tree fibers (DPT)	20
CHAPTER 3: EXPERIMENTAL METHODS	21
3.1 Materials	21
3.2 Preparation of SPI resins crosslinked by glutaraldehyde	21
3.2.1 SPI pH 12.5 resin	21
3.2.2 SPI pH 9.5 resins	23
3.3 Preparation of RS/JFa/SPI composites	23
3.4 Thermogravimetric analysis (TGA)	25
3.5 Differential scanning calorimetry (DSC)	26
3.6 Tensile properties	26
3.6.1 SPI resins	26
3.6.2 Rice straw fibers	27
3.6.3 Jute yarn and fabric	29
3.6.4 Date palm tree fibers	31
3.6.5 Composites	32
3.7 Interfacial shear strength (IFSS)	32
3.8 Flexural properties of composites	35
3.9 Scanning electron microscopy (SEM)	36
3.10 Dynamic mechanical analysis (DMA)	36
3.11 Treatment of DPT	37
3.12 Attenuated total reflectance Fourier-transform infrared (ATR-FTIR) spectroscopy	37
3.13 Moisture sorption	37
CHAPTER 4: RESULTS AND DISCUSSION	39
4.1 Moisture sorption	39
4.2 Tensile properties	41
4.2.1 Rice straw	41
4.2.2 Jute yarn and fabric	45
4.2.3 Date palm tree (DPT) fibers	47
4.2.4 SPI resins	49
4.2.5 Composites	52
4.3 Flexural properties	71
4.4 Interfacial shear strength (IFSS)	78
4.5 Dynamic mechanical analysis of composites	85
4.6 Fracture analysis by SEM	88
4.7 Thermal characterization	91
4.7.1 DSC of SPI resins	91

4.7.2	DSC of composites	94
4.7.3	TGA of RS, JF, and DPT fibers	95
4.7.4	TGA of resins	97
4.7.5	TGA of composites	100
4.7.6	ATR-FTIR analysis of alkali-treated DPT fibers	101
CHAPTER 5: CONCLUSIONS		103
CHAPTER 6: FUTURE SUGGESTIONS		107
REFERENCES		109

LIST OF FIGURES

Figure 1. Schematic showing the types of green resins available at present. ^{1,17-22}	4
Figure 2. Schematic of the types of plant fibers used as green reinforcement. ^{27,28}	5
Figure 3. Amine-glutaraldehyde crosslinking mechanism with peptide chains.	10
Figure 4. Plant cell wall structure a) overall structure, b) primary cell wall components, and c) secondary cell wall components. Note: recreated based on <i>Rytioja et al. (2014)</i> ⁶⁰ depiction.	11
Figure 5. Chemical structures of a) cellulose (β -D-glucose) and b) amylose/starch (α -D-glucose).	12
Figure 6. Chemical structures of constituent monomers of a) main hemicelluloses and b) other common hemicelluloses.	13
Figure 7. One possible depiction of the chemical structure of lignin and the three major monomers that make lignin. ⁷⁵	14
Figure 8. D-galacturonic acid, the main component of pectin.	15
Figure 9. Schematic illustration of the felting process.	24
Figure 10. Photographs of T-type RS/JFa/SPI composites a) before hot pressing, b) cured showing the bottom JFa layer, and c) cured showing the top RS layer.	25
Figure 11. Specimen preparation of fiber tensile test for a) cylindrical and b) rectangular fibers.	28
Figure 12. Examples of optical microscopic images of rice straw cross section.	29
Figure 13. Jute fabric tensile test specimen preparation according to ASTM 5035–11 strip test. Starting with a) fabric cut to equal widths of 30 mm and b) unravelling the side yarns to obtain 25 mm width.	30
Figure 14. Jute fabric under tension, clamped to a universal tensile testing machine as per ASTM 5035–11.	31
Figure 15. Date palm tree fiber fixed on universal tensile testing machine clamps prior to testing.	32
Figure 16. Resin droplet deposition on a plant fiber from an UHMWPE fiber.	34
Figure 17. Schematic of the microbond test setup.	34
Figure 18. Illustration of 3-point-bend test.	36
Figure 19. Visualization of green composite swelling mechanism, a) dry fiber/resin and b) swollen fiber/resin.	39
Figure 20. Water sorption data for JFa, RS, SPI resins, and their composites at different fiber loads.	41
Figure 21. Distribution of rice straw fiber properties a) Young's modulus and b) UTS obtained from fiber tensile test. $N = 53$ specimens.	42

Figure 22. Photographic image of a RS segment indicating an internode between two nodes.	43
Figure 23. Rice straw broken across its axis after the tension test on a universal Instron testing machine.	44
Figure 24. Typical stress-strain plot obtained from RS tensile test.	44
Figure 25. Typical stress-strain plots for woven JFa in warp and weft directions.	47
Figure 26. Typical stress-strain plots for untreated and NaOH treated DPT fibers.	48
Figure 27. Stress-strain plots for three SPI resins obtained from standard tensile tests.	52
Figure 28. Schematic of the separated RS/SPI and JFa/SPI composites for the purpose of hybrid composite theoretical analysis.	55
Figure 29. Stress-strain plots of three conditioned triple-layered composites (JFa/SPI, RS/JFa/SPI, RS/SPI) all made with 40 wt% fiber load.	59
Figure 30. Rouchan pyramid explaining the hierarchy of testing composite materials and structures. Note: recreated based on <i>Lopes et al. (2016)</i> ¹⁴² depiction.	62
Figure 31. Typical stress-strain plots of conditioned a) single-layered composites in warp direction, b) triple-layered composites in warp direction, c) single-layered composites in weft direction, and d) triple-layered composites in weft direction.	64
Figure 32. Tensile properties of six different RS/JFa/SPI composites in the warp direction before and after conditioning a) Young's modulus, b) ultimate tensile stress, and c) strain at maximum load.	68
Figure 33. Tensile properties of six different RS/JFa/SPI composites in the weft direction before and after conditioning a) Young's moduli, b) ultimate tensile stress, and c) strain at maximum load.	70
Figure 34. Unsuccessful four-point bend test of RS/JFa/SPI composites.	72
Figure 35. Side view of a stack of laser-cut RS/JFa/SPI flexural test specimens after conditioning.	73
Figure 36. RS/JFa/SPI T40 specimen fracture at the RS face under a three-point bend test, a) front view, b) bottom view.	74
Figure 37. Typical flexural stress-strain plots of RS/JFa/SPI composites obtained from three-point-bend test a) before conditioning and b) after conditioning.	75
Figure 38. Three-point-bend test results of three different RS/JFa/SPI composites before and after conditioning a) flexural modulus, b) ultimate flexural stress, and c) strain at maximum load.	77
Figure 39. SEM micrographs of a typical cured SPI resin droplet on jute fiber a) before and b) after microbond test.	79

Figure 40. Typical load vs displacement curves of microbond tests for RS/SPI and JF/SPI.	82
Figure 41. SEM micrographs showing surfaces of a) rice straw and b) jute fiber.	83
Figure 42. Interfacial shear strength with respect to contact area of a) JF/SPI and b) RS/SPI as obtained from microbond test.	85
Figure 43. DMA plots of T-type composites, showing a) loss modulus, b) storage modulus, and c) Tan δ plots with respect to temperature.	87
Figure 44. SEM micrographs for fracture surfaces of SPI12-140 resin taken from a 30° tilt angle where a) image taken at 1.5 mm width and b) magnified image of the area indicated with a yellow rectangle on (a).	88
Figure 45. SEM micrographs showing fracture surfaces of RS/JFa/SPI composites for a) and b) T40; c) and d) T50; and e) and f) T60. Note: the red \times marks denote SPI resin sites.	90
Figure 46. DSC thermograms of three SPI resins prepared at different chemical and/or thermal conditions.	92
Figure 47. DSC thermographs of RS/JFa/SPI composites with three different fiber loads (40, 50, and 60 wt%).	94
Figure 48. TGA thermograms of rice straw, jute, and date palm tree fibers, showing a) weight loss and b) derivative weight loss with respect to temperature.	97
Figure 49. TGA thermograms of the three hot pressed SPI resins, showing a) weight loss plot and b) derivative weight loss plot with respect to temperature.	99
Figure 50. TGA thermograms of RS/JFa/SPI composites, showing a) weight loss plot and b) derivative weight loss plots with respect to temperature.	100
Figure 51. ATR-FTIR spectra of untreated and alkali treated DPT fibers at different treatment times.	102
Figure 52. Experimental tensile properties (E_y and UTS) of T-type composites versus theoretical predictions based on ROHM, in two directions, warp (left) and weft (right).	105

LIST OF TABLES

Table 1.	Chemical composition of jute, rice straw, and date palm tree fibers.	17
Table 2.	Selected physical properties of jute, rice straw, and date palm tree fibers.	18
Table 3.	Rice straw tensile properties obtained from tensile test.	44
Table 4.	Tensile properties of JFa in warp and weft directions and twisted jute yarn.	46
Table 5.	Tensile properties of untreated and NaOH treated DPT fibers at different treatment times.	49
Table 6.	Tensile properties of SPI pH 12.5 resins at different plasticizer content.	50
Table 7.	Tensile properties of three different SPI resins denatured at different pH levels and/or cured at different temperatures.	51
Table 8.	Values of VC1 as calculated for the three different T-type composite systems.	54
Table 9.	Volume fractions of RS/JFa/SPI composites as calculated from mass-to-volume conversion.	56
Table 10.	Volume fractions of the theoretically separate RS/SPI and JFa/SPI composites.	57
Table 11.	Theoretical Young's moduli and UTS calculated according to ROHM.	58
Table 12.	Tensile properties of triple-layered and conditioned composites JFa/SPI, RS/JFa/SPI, and RS/SPI with 40% fiber loads each.	60
Table 13.	Tensile properties of dry RS/JFa/SPI composites in the warp direction.	69
Table 14.	Tensile properties of conditioned RS/JFa/SPI composites in the warp direction.	69
Table 15.	Tensile properties of dry RS/JFa/SPI composites in the weft direction.	71
Table 16.	Tensile properties of conditioned RS/JFa/SPI composites in the weft direction.	71
Table 17.	Flexural properties of dry RS/JFa/SPI composites.	77
Table 18.	Flexural properties of conditioned RS/JFa/SPI composites.	78
Table 19.	Microbond test results of SPI pH 12.5 bead on jute or RS fibers.	81
Table 20.	Dynamic mechanical analysis test results of T-type composites.	88
Table 21.	Onset temperatures of transitions (T1 and T2) and enthalpies of hot-pressed SPI resins.	92
Table 22.	Onset of melting temperatures of thermally cured SPI pH 12.5 resins.	93
Table 23.	Onset of melting temperatures of thermally cured SPI9 resins.	93
Table 24.	Onset temperature of degradation and enthalpies of RS/JFa/SPI composites.	95

Table 25. Onset temperatures of degradation (Td) and peak derivative weight losses of RS, JF, and DPT.	97
Table 26. TGA initial derivative weight loss peak and onsets of transition (Ti and Tii) of SPI resins.	99
Table 27. TGA Initial weight loss peak and onset of degradation (Td) of RS/JFa/SPI composites.	101

LIST OF SYMBOLS AND ABBREVIATIONS

D-sorb	D-sorbitol
DPT	Date palm tree
°C	Degrees Celsius
ε	Engineering strain
σ	Engineering stress
E_f	Flexural modulus
T_g	Glass transition temperature
GA	Glutaraldehyde
JF	Jute fiber
JFa	Jute fabric
IFSS	Interfacial shear strength
N	Number of specimens sampled
PMC	Polymer matrix composite
pH	Power of hydrogen
RS	Rice straw
ROHM	Rule of hybrid mixtures
ROM	Rule of mixtures
SEM	Scanning electron microscopy
SPI	Soy protein isolate
SPI12-120	Soy protein isolate resin pH 12.5 curing temperature 120°C
SPI12-140	Soy protein isolate resin pH 12.5 curing temperature 140°C
SPI9	Soy protein isolate resin pH 9.5
SD	Standard deviation of a sample
UFS	Ultimate flexural strength
UTS	Ultimate tensile strength
wt%	Weight percent
E_y	Young's modulus

PREFACE

CHAPTER 1: INTRODUCTION

Composites are multiphase materials that exhibit properties inherited from their dissimilar constituents. They are integral to applications where a single material (or constituent) in its native form would not suffice. Each distinct constituent contributes to the overall properties of a composite; hence, composite properties can be customized to fulfill wide variety of functions. Typically, composites comprise a continuous phase, matrix (or resin) that bonds and keeps in place the discontinuous phase material (i.e., dispersed phase or reinforcement).^{1,2} Composites may be classified according to the type of matrix used, that is, ceramic (CMC), metal (MMC), or polymer matrix composites (PMC); or according to reinforcement dimensions (e.g. nano- or micro-particles, flakes, fibers, yarns, fabrics, etc.). Mechanical properties of composites are determined by the properties of their constituents, their relative quantities, the geometry and architecture or arrangement of reinforcement, as well as the interfacial interaction between the distinct phases.

Fiber-reinforced PMCs are widely used in aerospace, automotive, structural, and other load-bearing applications.³ They are particularly useful for cases where reducing the component weight is critical. For example, in both aerospace and automotive industries reducing weight can significantly increase the fuel efficiency and, in many cases, the safety of the operation as well. Manufacturing and commercialization of PMCs developed concurrently with the booming petrochemical industry following World War II. Unlike their predecessor matrices (e.g., animal- or plant-derived glues), petroleum-derived polymer matrices have been proven to be highly resistant to degradation via both biological and radiative means. Reinforcing these nonbiodegradable matrices with strong

fibers (such as graphite/carbon, glass, or aramids) enabled the aforementioned applications to grow in the past four to five decades, which, in turn, attracted significant governmental and industrial funds toward PMC research, development, and cost reduction.³

With their high aspect ratio, fibrous materials allow for a high stress carrying ability that can be directed along one or more directions by arranging them accordingly. Among the most common fibers used to reinforce advanced PMCs are glass, carbon, aramid (e.g., Kevlar[®]), and ultrahigh molecular weight polyethylene (UHMPE) fibers (e.g., Spectra[®] and Dyneema[®]). All of them are primarily derived from petroleum. Common petroleum-derived polymer matrices include the thermosetting epoxy, polyester, phenol formaldehyde, vinyl ester, and polyurethane, as well as the thermoplastic polymers including polypropylene, polyethylene, polystyrene, and polyvinyl chloride.^{4,5} Fabricating composites from these non-biodegradable materials makes their end-of-life disposal and processing very complicated.

The PMC market remains dominated by petroleum-based materials⁶ due to their abundant supply, low cost, and unique properties. While a few biodegradable petroleum-based polymers do exist (e.g., polyvinyl alcohol) and eventually disintegrate to their monomers or other benign compounds, the process to get there could take much longer than the plant-derived polymers. All other polymers, however, take decades or even centuries to degrade.⁷ With this low rate of degradation, and the fact that less than 18% of global plastic waste is recycled,⁷ Earth's ecosystem is being threatened continually. Moreover, if the annual production of petroleum-based plastics stays the same, it will contribute 15% of the global carbon budget by 2050 and an estimated 12,000 Mt of plastic

waste would spread across the natural environment and landfills.^{8,9} At present, most of the plastic waste is discarded in landfills and that land may not be useful for any other purpose for several centuries.^{1,10}

In response to these threats, a global shift toward sustainable materials began a couple of decades before the end of the twentieth century. International entities such as the European Union began to act by obligating automobile manufacturers to produce vehicles with at least 95% of their mass to be reused or recycled at their useful life (Directive 2000/53/EC September 2000). As a result, sustainable materials have been in demand in the automotive industry. Similar trends have been increasing in other industries, such as packaging and textiles, since then.¹¹⁻¹³ In addition, many countries have enforced strict legislations such as banning single-use plastics and enforcing the use of sustainable materials, and a majority of the United Nations members have pledged to significantly reduce the use of plastics.¹⁴ Therefore, the shift from petrochemical-derived materials has become a global sociopolitical demand based on the necessity and relying less on manufacturers' ethical consciousness.

Composites are difficult to dispose of or efficiently recycle, compared to pure plastics, due to the need to separate constituents that are intentionally bonded for further processing. However, this problem could be completely avoided if the constituents were compatible with nature's carbon cycle to begin with.¹ In the 1990s, the term *green* composites emerged to describe resins and composite materials that are made from sustainably sourced non-petroleum materials, particularly those derived from plants.^{6,15,16} Thermoset green resins, which are the most common type of matrices employed in green composites, are mostly plant-based polymers that are crosslinked and plasticized by non-

petroleum-derived agents. **Figure 1** shows a schematic diagram of the types of green resins and some examples. They are generally classified into three categories based on their origin and production. Such resins may be prepared from extracts of raw plant biomass, roots, or seeds/grains such as protein or starch. They may also be indirectly produced from plant-derived sources via microbial fermentation or by the chemical synthesis of plant-derived monomers.¹

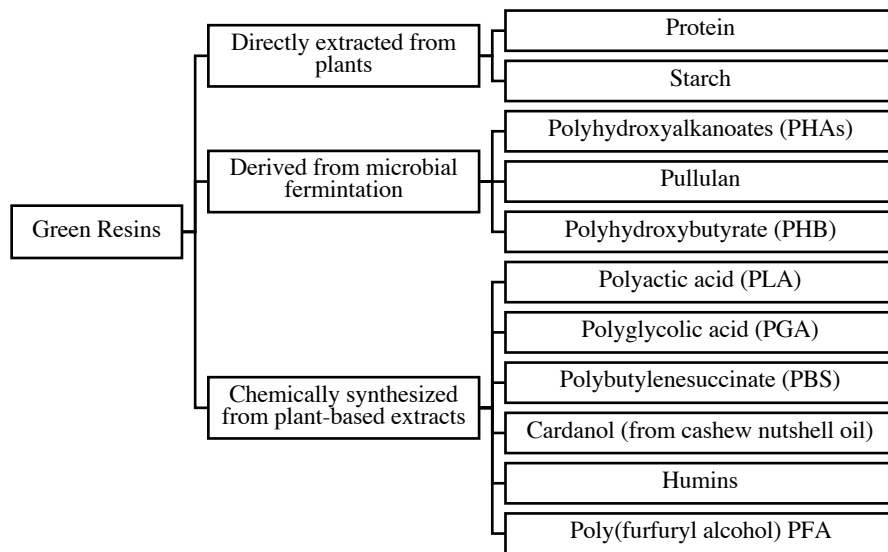


Figure 1. Schematic showing the types of green resins available at present.^{1,17-22}

Green reinforcement can be derived directly from wooden or non-wooden plant fibers. It can also be a reprocessed form of plant that is fully biodegradable, such as industrial biomass byproducts like the “silver skin” produced by coffee mills,²⁰ discarded wooden chopsticks,²³ recycled paper,²⁴ etc. **Figure 2** shows the most common forms of vegetable (plant) fibers that have been used to reinforce green composites. Due to their good specific mechanical properties, thermal/sound insulative hollowness, low cost,

widespread availability and renewability, plant based cellulosic fibers are the most used reinforcements in green composites.

The classification of green composites depends not only on the types of materials used, but also on how they were manufactured. Anastas and Warner first introduced the concept of *green chemistry* in the 1990s,^{25,26} putting forward the definition as the design of chemical products and processes to reduce or eliminate the use and generation of hazardous substances. This framework ensures the design of a production process that would lessen—or preferably eliminate—harmful byproducts. Employing the principles would assuredly complement the ecological cycle of green composites.

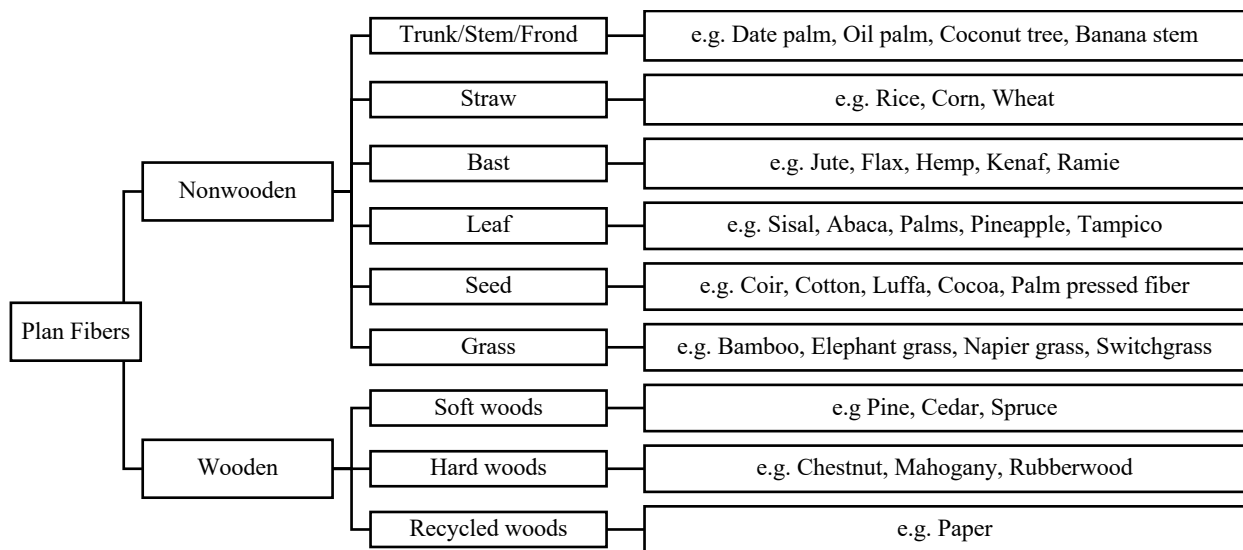


Figure 2. Schematic of the types of plant fibers used as green reinforcement.^{27,28}

In addition to resolving the issues related to material disposal, green composites sourced from agricultural waste would directly benefit the farming industry, and more importantly, the climate: today's greatest problem facing humanity. The emergence of synthetic fibers in the late 1920s has greatly reduced the demand on natural fibers.²⁹ What

was once a means to benefit from agricultural waste, has become a weak market which may not be of economic interest to farmers, leading farms to unhealthy practices such as open fire burning of residue—especially those with crops that are not primarily cultivated for their fibers or used as fodder for animals.

CHAPTER 2: BACKGROUND

2.1 *Soy protein resins*

Protein from soybean has been researched as a potential adhesive since the 1920s.³⁰ Consequently, soy-derived adhesives were widely commercialized in application. For instance, Henry Ford used soy protein-based resins in the manufacturing of some auto parts back in 1941.¹¹ Soy-derived bioplastics were also utilized in the plywood industry up until the 1960s, when synthetic formaldehyde-based adhesives were developed.^{31,32}

The coproducts of soybean processing are soy oil, soy flour (SF), soy protein concentrate (SPC), and soy protein isolate (SPI). Currently, soy protein is the world's most produced source of plant protein.³³ Its worldwide availability and low cost has placed it at an advantage for deriving inexpensive products on a commercial scale. SPI contains the highest protein weight percentage, with about 90%, followed by SPC and SF, with around 72% and 53-55%, respectively.^{34,35}

Soy proteins contain 20 different amino acids, of which glycinin 7S and β -conglycinin 11S (S stands for Svedberg unit)³⁶ comprise somewhere between 61 and 87% of the total protein content.³⁷⁻³⁹ The functional groups present on soy protein side chains are mainly hydroxyls, carbonyls, thiols, and aminos.⁴⁰ These groups determine the denaturing and treatment routes that SPI may undergo. The presence of these polar groups accounts for the high hydrophilicity of SPI. This is the feature that allows for surface compatibility and good hydrogen bonding capability between soy-based resins and cellulosic plant fibers used as reinforcements. However, at the same time, the hydrophilic groups also cause more water absorption by their composites, significantly affecting their properties.

To reduce the hygroscopic characteristic of SPI, its functional groups can be utilized as sites for self-crosslinking or by using external crosslinkers or modifiers of intramolecular interactions (i.e., hydrogen bonds).⁴¹ Improving water resistance begins by exposing hydrophilic/hydrophobic sites in the polypeptide chains and compatibilizing them either by blending hydrophobic polymers/monomers, enzymatic modification, or through crosslinking.^{39,40} Reducing their water absorbency, which degrades the fiber/resin interfacial bond and severely reduces the mechanical properties, is critical in composites. The functional or reactive groups can be exposed by changing the protein's conformation (or denaturing the protein), which can be induced thermally or chemically (i.e., modifying the pH environment). The conformation of proteins is very complicated, and denaturing produces secondary, tertiary, or even quaternary structures. These conformations directly affect the solubility, foaming, gelation, and viscosity of SPI.⁴² Moreover, the weight fraction of amino acids present in the SPI mix varies with varying pH levels. For instance, the 11S molecular weight fraction increases with an increased pH level.³⁷ 11S has a higher tendency to form disulfide bonds than 7S, and it is reported that films made from 11S show two to three multiples of tensile strength than those from 7S.³⁹

Neat SPI films (i.e., self-crosslinked resins) can be synthesized at pH levels away from SPI's isoelectric point. A point at which the charges on the protein are neutral and the entangled conformation leads to coagulation and poor solubility.⁴³ SPI's isoelectric point is calculated at about pH 4.5. Hence, to produce neat SPI films, the protein is denatured either below pH 4.5 (between 1 and 3) or at alkaline pH conditions (between 9 and 12). That treatment causes protein molecules to unfold and further solubilize.⁴⁴

However, at extreme pH levels (greater than 12 or lower than 1), the protein molecules exhibit strong repulsive forces that prevent the formation of neat (pure) SPI films.³⁹ Neat SPI resins tend to be too brittle to be employed in composites. Therefore plasticizers are commonly introduced to increase chain sliding, i.e., decreasing the accumulation of intermolecular forces between chains.^{39,44} As a result of plasticization, the resin exhibits lower stiffness and tensile strength but enhanced ductility, i.e., increased fracture strain. The most effective crosslinkers and plasticizers are those that are compatible with the SPI chemical structure, which, as mentioned earlier, is hydrophilic. That is the reason why water and alcohols have been used as soy protein plasticizers.³⁹ Crosslinking of SPI has been carried out by molecules with functional groups that can undergo imine-forming reactions, such as aldehydes (e.g., formaldehyde, glyoxal, and glutaraldehyde).^{41,45-50} Glutaraldehyde (GA) can link two peptide chains by forming methylene bridges through the reaction with amine groups that exist on the peptide chains.⁴⁵ It is an attractive crosslinker due to its high reactivity at room temperature and its ability to react with ϵ -amino, amino acid residue, and several other nucleophilic groups in protein.^{32,51} GA also has a boiling point of 187°C, which is much higher than the temperatures typically used to crosslink SPI resins. A visualization of the GA crosslinking mechanism in SPI via Maillard reaction is shown in **Figure 3**.^{32,52} Many other crosslinkers including glyoxal, sugar-aldehydes have also been used to crosslink soy protein and other proteins.^{36,45,48,50,53-}

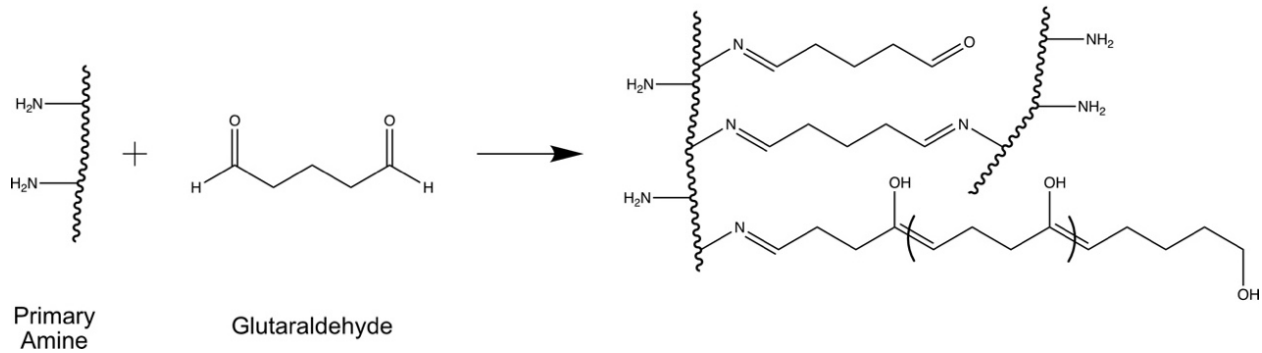


Figure 3. Amine-glutaraldehyde crosslinking mechanism with peptide chains.

2.2 Composition and structure of plant fibers

Plants have two types of cell walls, primary and secondary, as depicted in **Figure 4**. Primary cell walls are synthesized during plant growth and, in most plants, comprise cellulose, hemicellulose, pectins, and proteins, in different proportions depending on the plant variety. The secondary walls, which are usually thicker, are deposited after plant growth, providing functionality (water transportation and mechanical support) to the plant.⁵⁸ They also determine the shape of cells and mainly comprise of cellulose, lignin, and hemicellulose.^{58,59} Both walls are composites made up of an amorphous matrix reinforced with crystalline cellulose.

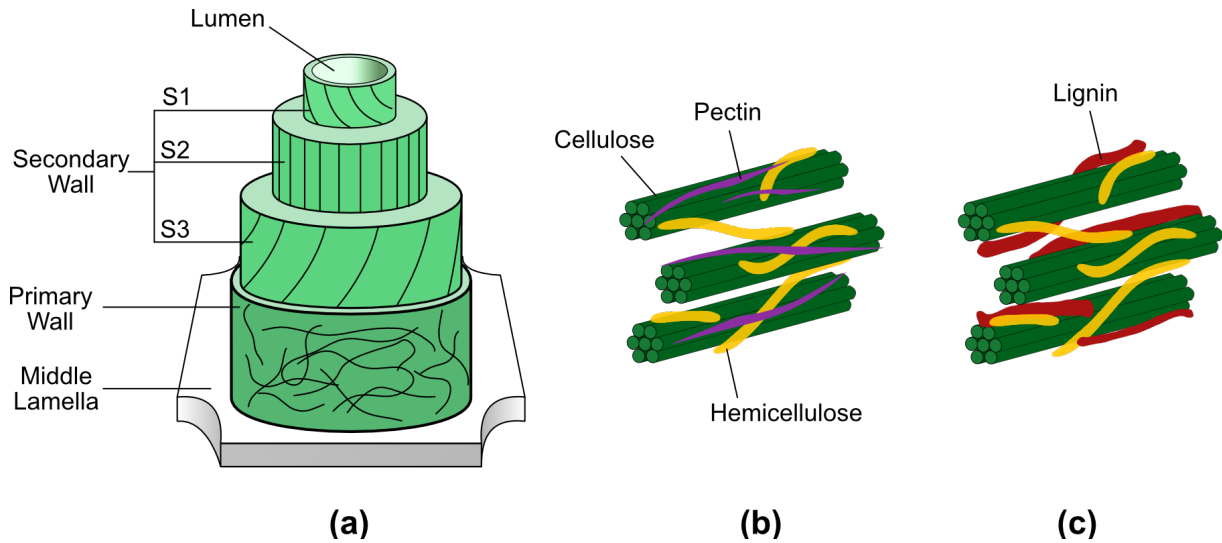


Figure 4. Plant cell wall structure a) overall structure, b) primary cell wall components, and c) secondary cell wall components. Note: recreated based on Rytioja *et al.* (2014)⁶⁰ depiction.

2.2.1 Cellulose

Cellulose is a linear polysaccharide with two D-glucopyranose molecules, called cellobiose, as its repeating unit.^{59,61} The orientation of the hydroxyl groups within the cellulosic ribbon segment, as well as their alignment between adjacent molecules, determines the crystallinity of the cellulose.⁶² **Figure 5** depicts the structural difference between β - and α -glucose linkages. Cellulose is made of 1,4 β -glucose links that keep the molecules in the chain 180° apart, as depicted in Figure 5a. Soluble starch shown in Figure 5b, however, comprises 1,6 and 1,4 α -glucose links leading to the polymer's high branching, high coiling, and low crystallinity. The β -type linkage which leads to the ordered conformation of cellulose is responsible for its insolubility. Additionally, it allows for higher packing of cellulose chains, leading to high crystallinity and longitudinal stiffness. Cellulose nanocrystals have Young's modulus values in the range

of 110–200 GPa and a theoretically predicted tensile strength of 2-8 GPa.^{63–65} The high specific mechanical properties of native cellulose are the reason plant fibers are being used to reinforce composites.

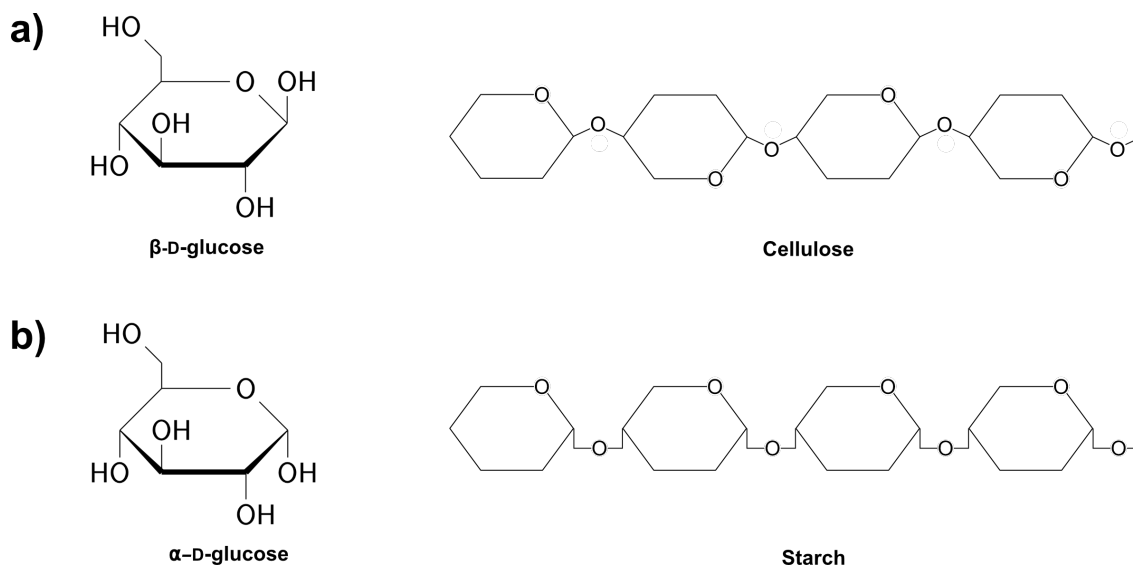


Figure 5. Chemical structures of a) cellulose (β -D-glucose) and b) amylose/starch (α -D-glucose).

Cellulose polymorphs include the native cellulose I and its derivatives II, III, and IV.⁶⁶ Cellulose I β , which is native to all plants, has a monoclinic structure with the two chains oriented parallel to each other.^{67,68} The chains' parallelism can be disrupted using chemical or thermal treatment to produce the other cellulose polymorphs, i.e., cellulose II, III, and IV.⁶⁶ Cellulose I's undisrupted orientation, theoretically, exhibits the highest mechanical properties that are suitable for composites,⁶⁹ while cellulose II possesses more thermal stability.⁶⁷ For example, cotton (cellulose I) is much stronger than viscose rayon (cellulose II).

2.2.2 Hemicellulose

The chemical species found in plants are not all as discernible and easy to identify as cellulose. Consequently, classifying plant cell wall constituents commonly follows the shared functionality of a group or the most dominant chemical identity. For instance, most plant biologists use the term “hemicellulose” to describe a family of amorphous cell wall polysaccharides that have type β -(1 \rightarrow 4)-linked backbones of glucose, mannose, or xylose, and that are neither cellulose nor pectin.⁷⁰ **Figure 6** depicts the main hemicelluloses, as well as other saccharide monomers that are commonly included in the hemicellulose family (e.g., galactose, arabinose, and glucuronic acid).^{70,28} The estimated Young’s modulus of nearly dry and nearly saturated hemicellulose have been reported to be around 8 GPa and 0.01 GPa, respectively.⁷¹

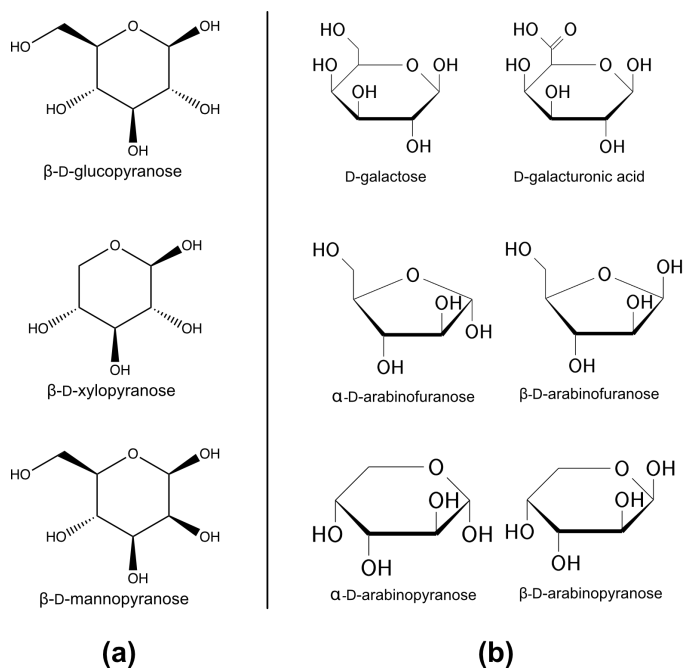


Figure 6. Chemical structures of constituent monomers of a) main hemicelluloses and b) other common hemicelluloses.

2.2.3 Lignin

Lignin is the second most abundant natural biopolymer after cellulose.⁷² As seen in Figure 4, it is another amorphous component of a plant cell wall. It is a highly branched phenolic compound that forms van der Waals and hydrogen bonds with cellulose microfibrils present in the secondary wall. Lignin plays the role of structural support by providing rigidity and cell-to-cell adhesion. Its hydrophobicity makes cell walls impermeable to water, and it also protects against pests and pathogens.^{59,73,74} The most common building units of lignin are the three monomers: *p*-hydroxyphenyl, guaiacyl, and syringyl,⁷⁵ which together form a complex structure similar to that illustrated in Figure 7.

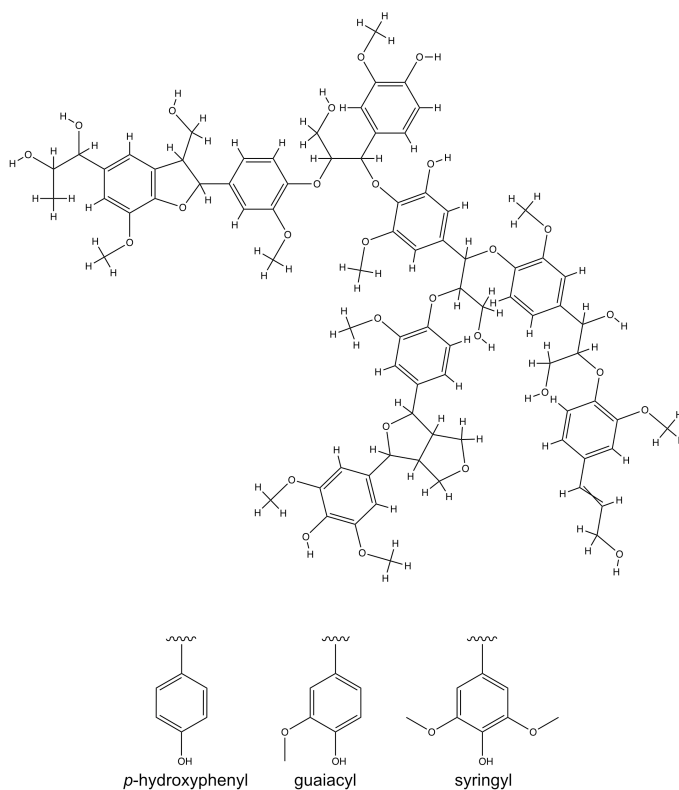


Figure 7. One possible depiction of the chemical structure of lignin and the three major monomers that make lignin.⁷⁵

2.2.4 Pectin

The middle lamella (the layer between cells, shown in Figure 4) is rich in other types of adhesive materials, and existing in high abundance are pectins. These are highly branched and heterogenous polysaccharides rich in galacturonic acid, as shown in **Figure 8**.^{59,76,77} They are also found within the primary cell wall and enhance crosslinking between cellulose and hemicellulose.⁶⁰ The complex structures of pectins primarily comprise homogalacturonan (shown in Figure 8), in addition to other pectic polysaccharides such as rhamnogalacturonan I, rhamnogalacturonan II, and xylogalacturonan.⁷⁷

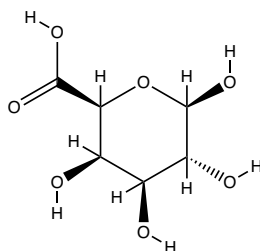


Figure 8. D-galacturonic acid, the main component of pectin.

2.3 Treatment of natural fibers

Plant fibers are primarily composites of cellulose-reinforced amorphous matrices. Incorporating these materials into a new matrix (i.e., resin) suppresses the utilization of cellulose as a mechanical reinforcement. The change in geometry or form, orientation, weight, or volume fractions of cellulose fibers affects the composite material's response to applied loads, and hence, its mechanical properties. As a result, many treatments have

been implemented to modify the surface and the morphology of plant fibers. These include mercerization,^{78–84} acetylation,^{78,79,85–88} silane treatment,^{23,78,86,89} acrylation,^{78,80,84,90} steam stabilization,⁹¹ corona treatment,^{5,90,92–94} and plasma treatment.^{90,93,95–97} Many of these treatments could be designed to increase the fraction of crystalline cellulose in the fibers, thereby enhancing the stiffness and strength of the fibers which will reflect on the composite properties. Moreover, the increased crystallinity is associated with less water absorption in plant fibers, an added benefit.⁹⁸ This is due to native crystalline cellulose having weak hygroscopic characteristics compared with the other chemical species found in plant cell walls. Exposing cellulose to plant-based resins also acts as an opportunity to enhance fiber/resin adhesion at the interface through hydrogen bonding. Obviously, covalent bonds—which cannot be disturbed or broken by water as compared to hydrogen bonds—are the most preferable. It is known that good adhesion results in better structural interlocking and, hence, results in better Young' modulus and strength.⁹⁹ Stronger fiber/resin interface can also prevent water transport through interfacial capillary routes and, thus, retain the mechanical properties of the composites. The fiber/resin adhesion mechanism is rather complex and has several contributing factors. Of these, the topography at the interface (mechanical), chemical bonding, acid-base reactions (pH levels), surface energies/wettability are mostly accountable for this adhesion.⁵ As a result, to coerce fibers and resins to better bond to each other, one or a combination of methods can be employed.¹⁰⁰ These include pretreatment of the fiber surfaces, pretreatment of the resin, and the incorporation of surface modifiers or compatibilizers.⁹⁴ Particularly in plant fiber-reinforced composites, the most easily implemented method is fiber surface treatment.

2.4 *Fibers used in this project*

Unlike synthetic fibers, vegetable fibers have highly inconsistent chemical compositions, though the constituents are same as discussed earlier. Their properties and quality of harvest depend on many factors, such as geographic region, weather, season, harvesting methods, plant age, etc.¹⁰¹ That is why plant fibers exhibit a wide range in mechanical properties, even if they were sourced from the same plant. Consequently, studying their physical properties relies on statistical significance and is often reported as a distribution of the studied characteristics. The work performed in this thesis utilized three different natural fibers: jute fibers, rice straw fibers, and date palm tree fibers. **Table 1** presents the weight fractions of cellulose, hemicellulose, and lignin present in these three fibers. **Table 2** presents some selected mechanical and physical properties that are common to fiber mechanics studies, i.e., Youngs modulus (E_y), ultimate tensile strength (UTS), elongation to break, density, and diameter.

Table 1. Chemical composition of jute, rice straw, and date palm tree fibers.

Fiber	Type	Cellulose (%)	Hemicellulose (%)	Lignin (%)	Refs.
Jute	Bast	61.0–73.2	13.6–20.4	12.0–16.0	⁶⁷
Rice straw	Straw	33.0–45.0	19.3–28.0	10.0–18.9	^{67,102,103}
Date palm tree	Leaf	33.9–46	18–26.1	20.0–27.7	^{67,104–106}

Table 2. Selected physical properties of jute, rice straw, and date palm tree fibers.

Fiber	Longitudinal E_y (GPa)	Longitudinal UTS (MPa)	Elongation to Break (%)	Density (kg/m ³)	Diameter (μm)	Refs.
Jute	10–60	393–860	1.2–1.8	1,300–1,520	25–250	82,107,108
Rice straw	3.3	75	–	60–450* 560–720 [†]	–	109–112
Date palm tree	2–12	60–275	2–19	900–1,200	100–1000	82,107,108

* *Baled rice straw.*

† *Pelleted rice straw.*

2.4.1 Jute

Jute (*Corchorus capsularis*) is the second most cultivated natural fiber in the world.¹⁰⁸ It is grown for its core (which was used for cooking) and its fibers in Eastern Asia, South America, and the Mediterranean; with India, Bangladesh, and China being the highest jute producing countries.^{67,108} The annual production of jute fibers by its major producing countries alone exceeds 2.85 Mt.¹¹³ Due to its good mechanical properties, jute fibers are conventionally spun into yarns and used in packaging, textile, footwear, and ropes.²⁸ Utilization of jute fibers for reinforcing resins dates back to the 1920s, when they were incorporated in shellac resins.¹¹⁴ Jute fibers (JF) and fabrics (JFa) are still commonly used as sustainable reinforcements for resins, and their utilization in automotive paneling has been on the rise since the 1990s.¹⁰⁸

2.4.2 Rice straw fibers (RS)

Rice straw is part of the rice plant (*Oryza sativa* L.) and is a byproduct of the gigantic rice farming industry. Rice farming produces the world's largest amount of crop residue,¹¹⁵ with approximately 800 Mt of dry biomass residue a year.¹⁰² Between India, Thailand, and the Philippines alone, 129.73 Mt of rice straw is produced annually.¹¹⁶ Rice straw fibers are known to have a very low density. As seen in Table 2, rice straws have densities of more than one order of magnitude lower than jute or date palm tree fibers. In fact, even pelletized (pressed) rice straw fibers have lower densities, ranging from 560 to 720 kg/m³.¹⁰⁹ Rice straw has a high silica content, which makes it a harsh material with low digestibility, thus, a less favored fodder for cattle.¹¹⁵

Many farmers in the northern states of India and other rice farming regions produce three crops a year. That leaves very little time after harvesting rice to prepare the land to plant new crops. Thus, farmers resort to open-field burning of rice straw to dispose dry waste and prepare the land for the next crop, control weeds and diseases, and to release nutrients in the soil.¹⁰² It is the quickest and least expensive means to achieve all of that, though it generates extremely high amounts of toxic gases such as CO and CO₂ and releases large amounts of particulate matter below 2.5 μm (PM_{2.5}). A remarkable amount of rice straw is burned annually, with percentages reaching as high as 95% (2002–2006), 62% (1999–2000 and 2004–2005), 62% (1995–2005), 53% (2013), and 48% (2002–2006) in the Philippines, India, China, Egypt, and Thailand, respectively.¹¹⁷ As mentioned earlier, this practice contributes to the release of greenhouse gasses as well as aerosolized black carbon. The utilization of rice straw, however, has been promisingly increasing since the beginning of the twenty-first century.¹¹⁷ While traditionally it has been used as pelletized

fuel, fertilizer, or reinforcing mud for hut walls, it has also been incorporated, in recent years, as PMC reinforcement on a small scale.¹¹⁸⁻¹²¹

2.4.3 Date palm tree fibers (DPT)

The date palm tree (*Phoenix dactylifera* L.) was most likely first domesticated in the Fertile Crescent.¹²² Nowadays, it grows in other regions, such as North Africa, Canary Islands, Pakistan, India, and the United States.^{67,123} Although the date palm tree is considered a low maintenance tree, dying fronds and leaflets are regularly pruned to ensure the tree's health and growth. In addition, old chlorotic fronds (i.e., pale or chlorophyll-deficient fronds) may detach from the tree and fall, causing a safety hazard. The date palm tree is farmed mainly for the sugary fruits it bears (i.e., dates),¹²⁴ and that industry results in an annual production rate of 4.2 Mt of date palm tree fibers.¹⁰⁴ Date palm fibers are traditionally used in rope making, basket and mat weaving, and in constructing shelter huts. These applications have largely been replaced by other modern-day materials. Hence, accumulating more fiber waste burdens farmers which has only encouraged them to burn those byproducts.¹²⁵

In this research, green composites were produced from sustainable plant sources. The focus was using high amounts of RS in simple minimal waste composite manufacturing techniques. With the analyses relying on mechanical properties that appeal to the interests of PMC and fiber-reinforced composite fields.

CHAPTER 3: EXPERIMENTAL METHODS

3.1 *Materials*

Soy protein isolate (SPI) was donated by the Archer-Daniels-Midland Company (Chicago, IL). Glutaraldehyde solution 25% in H₂O was purchased from Sigma-Aldrich (St. Louis, MO), and high-purity D-Sorbitol was purchased from VWR International, LLC (Solon, OH). NaOH pellets were purchased from Avantor Performance Materials, LLC (Radnor, PA). Untreated plain woven jute fabric (JFa) was purchased from JOANN Fabrics and Crafts (Ithaca, NY). Baled rice straw (RS) was purchased from Engine 109 The Bulk Depot (Hollister, CA). Date palm tree fibers were donated by the Arizona State University Arboretum (Tempe, AZ).

3.2 *Preparation of SPI resins crosslinked by glutaraldehyde*

All SPI resins in this thesis used glutaraldehyde as the crosslinker, D-sorbitol as the plasticizer, and NaOH as an alkali denaturing agent. Resins at two different alkaline pH levels: 9.5 and 12.5, were prepared and characterized. Of these, SPI 12.5 resin was used for fabricating hybrid SPI/RS/JFa.

3.2.1 *SPI pH 12.5 resin*

To prepare SPI 12.5 resins, SPI powder was dispersed in deionized water at a 3:20 SPI-to-water mass ratio and mixed to form a homogenous lump-free slurry. The protein in SPI was denatured by adding 4M NaOH to the SPI slurry in amounts that resulted in a 12.5 pH upon the addition of crosslinker. The pH levels were measured using an electronic pH meter (Starter 2100 pH Bench and an ST210 pH electrode, OHAUS® Corp.,

Parsippany, NJ). The high pH value was chosen specifically for the hybrid RS/JFa reinforced composites since it greatly enhances the solubility of SPI in water and requires less water to do so. This is important because the randomly distributed fiber length and orientation of rice straws are further randomized with needle-punching (felting). Hence, the resin must be low in viscosity to effectively impregnate the fiber complex and interlaced hybrid reinforcement geometry. Furthermore, using less water allows for fast and more uniform evaporation, less water entrapment within the complex hybrid structure of the reinforcement, and results in less warping. Denaturing was also assisted by thermal energy. The beaker containing alkali SPI slurry was placed in a water bath and maintained at 80°C for 30 min while being stirred using a magnetic stirrer at 600 rpm. Then, the plasticizer (D-sorbitol at 5 wt% of SPI) and crosslinker (glutaraldehyde with a fraction of 10 wt% of SPI) were added and left to stir for another 30 min.

The precured liquid resin was poured into Teflon® molds and allowed to evaporate in an open-vent convection oven (Thermo Fisher Scientific Co., Model No. PR305225M, Waltham, MA) at 46°C to bring the moisture content to 12–15%. The precured semidry resin sheet was then fully cured using a hot-pressing technique. A hot press (Carver Inc., model 3981-4PROA00, Wabash, IN) was employed at 1 MPa pressure. The resulting resin sheets had thicknesses of around 1.5 mm. Two different curing temperatures: 120°C and 140°C were used to prepare resin sheets, and they were pressed for 20 min and 5 min, respectively. The resin sheets were laser cut to dimensions compatible with the corresponding mechanical, physical, and thermal tests.

3.2.2 *SPI pH 9.5 resins*

The lower (9.5) pH denatured resin was fabricated following a similar procedure, except that the SPI-to-water ratio was 1:12. In addition, the lower pH made the resin mix highly viscous, hence, a mechanical stirrer (Kinematica Inc., Model No. PX-SR 90D, Bohemia, NY) was used instead of a magnetic stirrer to obtain uniform mixture.

3.3 *Preparation of RS/JFa/SPI composites*

Rice straw fibers were washed twice with pure tap water and left to dry for 3 h under 50°C. Plain woven jute fabric was used as received. The fabric was cut to 0.254 m × 0.254 m mats and weighed using a microscale. Their mass was matched with the mass of dry rice straws to maintain a 1:1 mass ratio between the two fibers. The rice straws were randomly spread on top of the square jute fabric. Then, the two-layered structure was sprayed with deionized water to soften the rice straw. After that, the fibers were passed through an automated felting (also known as needle punching) machine (FeltLOOM[®] PRO SERIES, Sharpsburg, KY), similar to the schematic illustration shown in **Figure 9**, to interlace the two fibers into one condensed mat. Felting was performed at 20% roller speed and 50% needle speed. Each mat was passed ten times through the felting machine to obtain thorough interlacing between jute fibers in the fabric and rice straw. The resulting mats were then placed in a Teflon[®] mold and left to dry under 50°C for 1 h before the precured resin was poured and massaged to obtain proper impregnation. The resin-soaked mats were placed in an open-vent convection oven under 46°C for ~45 h to evaporate the moisture and obtain resin with approximately 12% water content.

Following that, the semidry RS/JFa mats containing SPI resin were hot-pressed to cure the resin and further crosslink it.

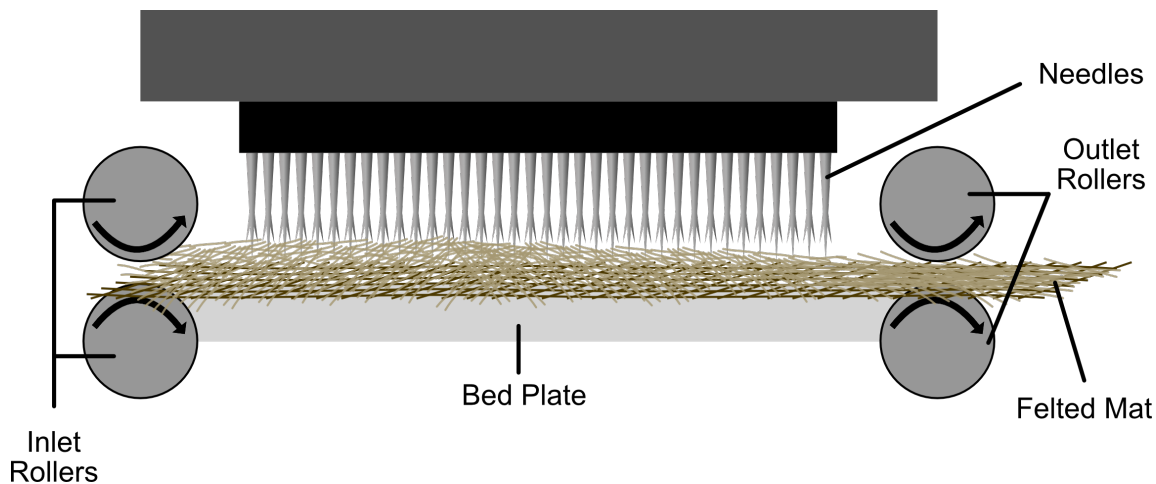


Figure 9. Schematic illustration of the felting process.

Three fiber contents (loads): 40%, 50%, and 60% by mass were used to fabricate the composites. For each fiber load, both single-layered and a triple-layered composites were produced. The composites are denoted by an “S” or a “T” for the single- or triple-layered composites, respectively, and are followed by the percent of fiber content. For example, the single-layered composite with a 40 wt% fiber content (RS + JFa) is shortened to S40. Similarly, the triple-layered composite with a fiber content of 50% is denoted as T50. The curing conditions using a hot press (Carver Inc., Model No. 3895.4NE0000, Wabash, IN) were 120°C under a pressure of 1.4 MPa for 20 min for the single-layered composites and 140°C under a pressure of 4.1 MPa for 5 min for the triple-layered composites.

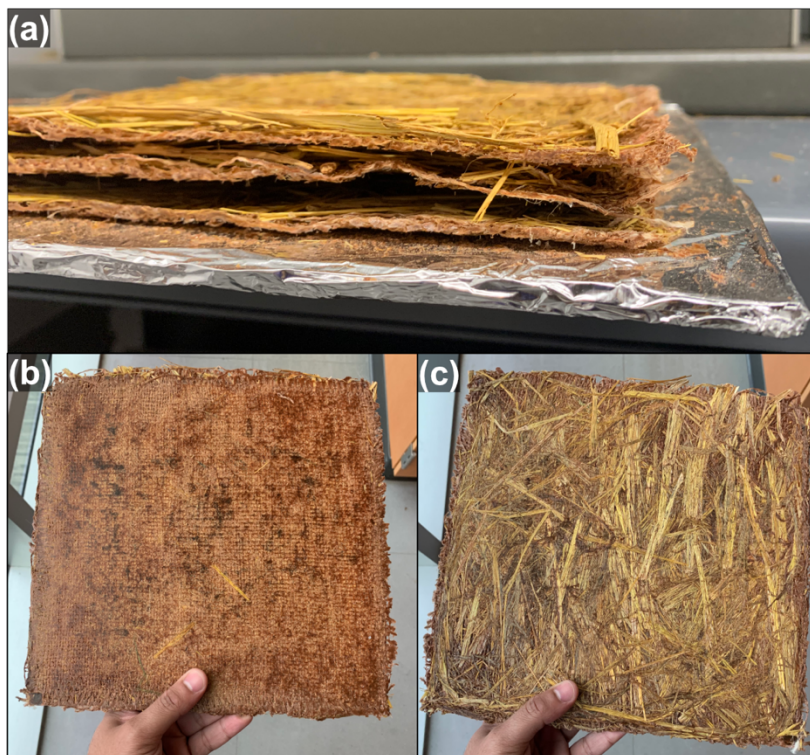


Figure 10. Photographs of T-type RS/JFa/SPI composites a) before hot pressing, b) cured showing the bottom JFa layer, and c) cured showing the top RS layer.

3.4 *Thermogravimetric analysis (TGA)*

A thermogravimetric analyzer (TA Instruments Inc., Model No. Q500, New Castle, DE) was used to analyze the thermal degradation characteristics of the fibers, resins, and the composites. Of particular interest were the percent weight losses at different temperatures, degradation onset temperatures, and char residue remaining at the end of the test. The testing conditions for all specimens were the same, under temperatures from 30 to 600°C at a rate of 20°C/min and under a constant 50 cc/min flow of nitrogen gas.

3.5 *Differential scanning calorimetry (DSC)*

Differential scanning calorimetry (TA Instruments Inc., Model No. Q500, New Castle, DE) was performed according to ASTM D5028–17 to determine the transition temperatures and enthalpies of transitions for the resins and composites. The testing conditions for all specimens (SPI resins or RS/JFa/SPI composites at different fiber contents) were the same, and were performed under a 50 ml/min nitrogen flow and a temperature range between 30 and 350°C at a rate of 5°C/min.

3.6 *Tensile properties*

The tensile properties of the fibers, resins, and their composites were characterized using an Instron universal testing machine (Instron Corp., Model No. 5566, Canton, MA). A 10 kN load cell was fixed for all tensile tests. The test particulars are detailed in the next sub-sections.

3.6.1 *SPI resins*

A preliminary resin tensile test was performed to determine ideal plasticizer content. The specimens were laser cut to rectangular shapes of 10 mm x 70 mm. The gauge length was 30 mm and the crosshead speed used was 10 mm/min (strain rate of 0.33 min⁻¹); except for the non-plasticized specimen where a 1.5 mm/min was used (strain rate of 0.05 min⁻¹).

As for the main resin tensile tests, rectangular resin specimens were laser cut to have a 6:1 ratio between gauge length and width. The gauge length was chosen to be 30 mm; hence, the resins were cut to a 5 mm width. The total length of each specimen was 70 mm.

All specimens were conditioned at the ASTM conditions of 21°C and 65% RH for 72 h prior to testing. Width and thickness measurements of each specimen were averaged from five different readings taken within the gauge length using a digital caliper (Fowler High Precision, Model No. Pro-Max PN 54-200-777, Auburndale, MA). Then the resin specimens were clamped directly to the tensile machine using a clamp pressure of around 0.5 MPa. A pretest cycle was added to straighten up the sample and omit readings from slack at the beginning of the test. The pretesting conditions were carried out at a crosshead speed of 2 mm/min up until a stress of 0.5 MPa. The tensile test was performed in compliance with ASTM D638–14 with the crosshead speed set to 5 mm/min (strain rate of 0.167 min⁻¹) to cause ductile rupture between 0.5–5 min. Specimens that exhibited ductile rupture outside of that timeframe were omitted.

3.6.2 *Rice straw fibers*

A total of 53 cylinder-like rice straws were slit longitudinally and unrolled to obtain a rectangular sheet. The edges of the fiber sheet were then glued using epoxy to a paper tab that had a pre-cut gap of 25 mm, representing the gauge length, as depicted in **Figure 11**. The width was determined by tracing out each fiber specimen on a piece of paper and then averaging the three width segments using a digital caliper. Due to the fragile nature of the rice straws, directly applying the caliper to the straws would crush most of them, and hence some weaker fibers would be eliminated. This would have defeated the purpose of this test, which aimed to find the distribution of the rice straw tensile properties. Moreover, the thickness of each specimen was measured after the tensile test using an optical microscope (Olympus Corp., Model No. BX51, Hamburg, Germany) and

a 10x/0.25 objective. The cross-sectional images of the rice straw, such as the ones shown in **Figure 12**, were taken from the areas closest to the paper tabs to avoid segments deformed from the load, or parts compressed from the clamps. An image processing software, ImageJ (Version 1.42q, National Institutes of Health, USA), was used to determine the mean and standard deviation of the 12 to 30 thickness measurements taken for each specimen. The fibers were conditioned at 21°C and 65% RH for 48 h as per ASTM D1776–04 before testing. The tensile test was performed using a 25 mm gauge length and a crosshead speed of 0.1 mm/min (strain rate of 0.004 min⁻¹) to achieve a break between 1 and 2 min. Pretest conditions were used to straighten up the fibers. The pretest stress varied from 1 MPa to 5 MPa based on the sample at a fixed crosshead speed equal to 1 mm/min.

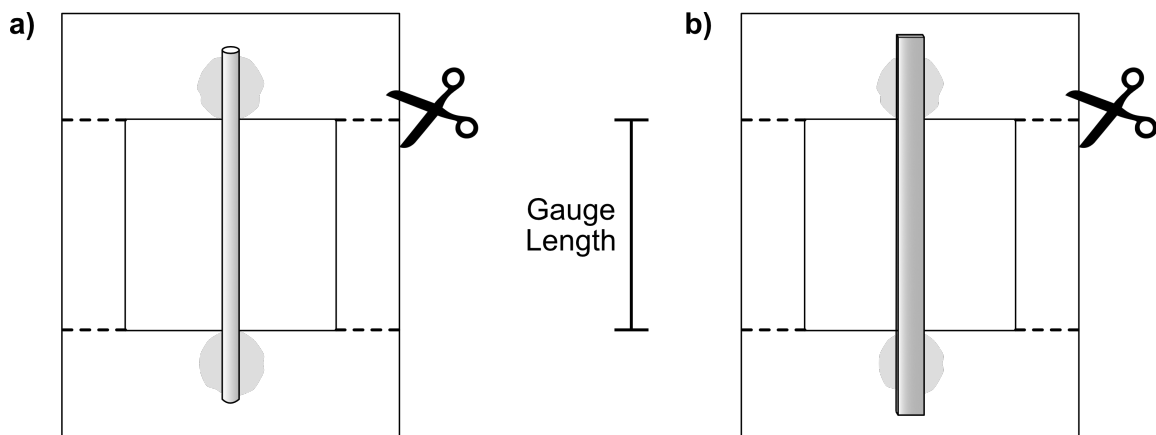


Figure 11. Specimen preparation of fiber tensile test for a) cylindrical and b) rectangular fibers.

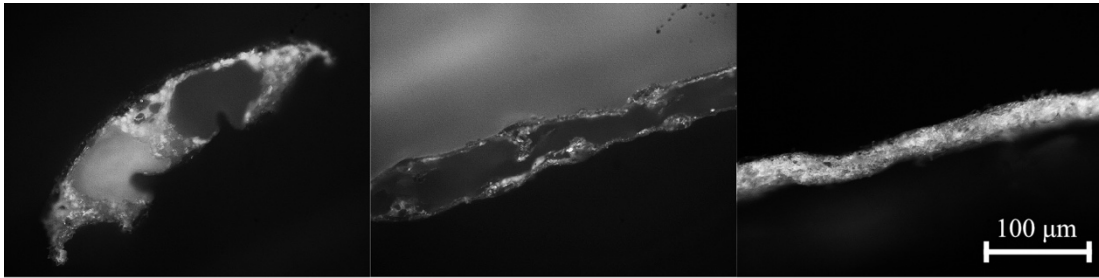


Figure 12. Examples of optical microscopic images of rice straw cross section.

3.6.3 *Jute yarn and fabric*

As mentioned earlier jute was received in the form of a woven fabric, and was tested according to ASTM 5035–11: the fabric “strip test” method (in the warp and weft directions); and as a yarn according to ASTM 2256–10: the “single strand” method. Prior to the tests, jute fabric or yarn specimens were conditioned at 21°C and 65% RH for 48 h. The thickness of the jute fabric was measured using a compressometer (Frazier Precision Instrument Company Inc., Hagerstown, MD) and a 9.525 cm (3/8 inch) diameter presser foot. Five measurements were taken for each specimen at a pressure of 17.2 ± 4.9 kPa. For the yarns, this thickness was assumed to equal the diameter of the outer *cylindrical sleeve* of the yarn geometry.

Yarns were unraveled from the jute fabric and fixed on paper tabs, similar to the fixture shown in Figure 11a. The test adopted a gauge length of 30 mm, and the crosshead speed was determined to be 4 mm/min (strain rate of 0.133 min^{-1}) to achieve a break at around 20 s according to ASTM 2256–02. A pretest cycle was set to 3 mm/min until 2 MPa to eliminate slack.

Woven jute fabric was tested in the two axes of weave, namely, warp (machine direction) and weft (also known as fill). The strip test dictates cutting a certain fabric

width and length and then unravelling the width from each side of the specimen as seen in **Figure 13**. The fabric specimens were cut to widths of 30 mm and then unraveled to 25 mm. They were then fixed in between the universal tensile machine's clamp as shown in **Figure 14**. Gauge length was set to 30 mm, and to achieve a break between 0.5–5 min according to ASTM 5035–11, a crosshead speed of 5 mm/min (strain rate of 0.167 min^{-1}) was used.

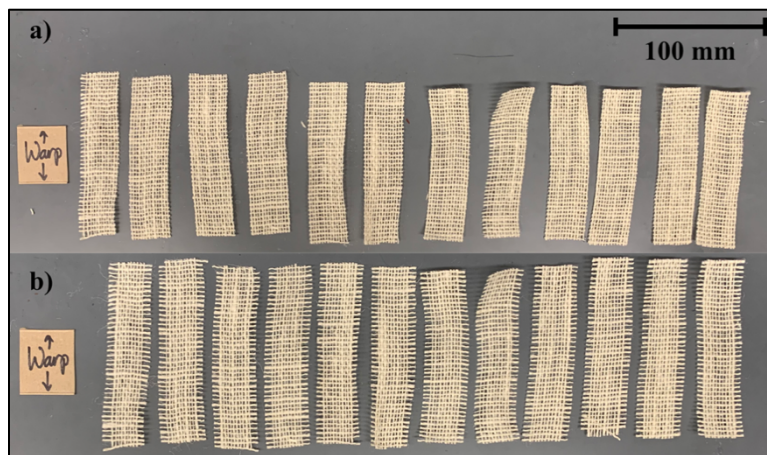


Figure 13. Jute fabric tensile test specimen preparation according to ASTM 5035–11 strip test. Starting with a) fabric cut to equal widths of 30 mm and b) unravelling the side yarns to obtain 25 mm width.

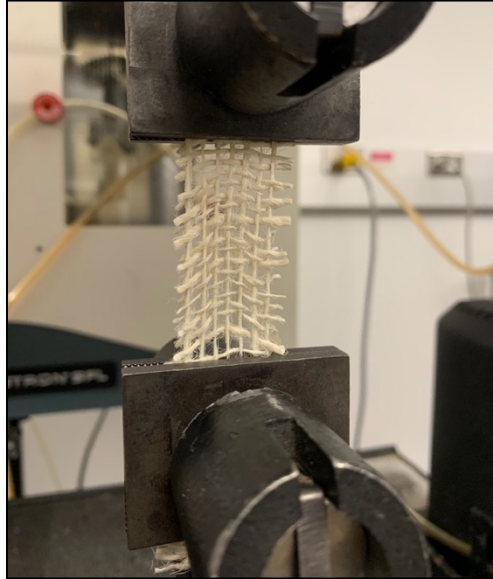


Figure 14. Jute fabric under tension, clamped to a universal tensile testing machine as per ASTM 5035–11.

3.6.4 *Date palm tree fibers*

Date palm tree (DPT) fibers were washed twice with pure tap water and dried in a forced-air convection oven (Thermo Fisher Scientific, Isotemp™, Waltham, MA) at 46°C overnight. They were then glued to paper tabs (similar to the illustration in Figure 11b) and conditioned at 21°C and 65% RH for 48 h prior to testing. A pretest setting at a rate of 1 mm/min up to 3 MPa was used to straighten the fiber strand. The fiber's tensile properties were obtained according to the "single-filament" test, ASTM D 3379–89 as seen in **Figure 15**, with a gauge length of 25 mm. For failure to occur at around 1 min and less than 2 min, the crosshead speed was determined to be 0.6 mm/min (strain rate of 0.025 min⁻¹).

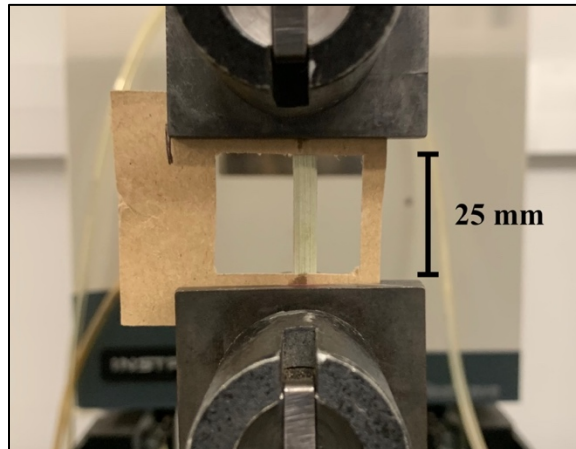


Figure 15. Date palm tree fiber fixed on universal tensile testing machine clamps prior to testing.

3.6.5 Composites

Each RS/JFa/SPI composite was tested in both warp and weft directions as well as before and after being conditioned at 21°C and 65% RH for 72 h, according to ASTM D638–14. The gauge length and crosshead speed were 30 mm and 1 mm/min (strain rate of 0.033 min⁻¹), respectively, to reach failure between 0.5–5 minutes. The failure criterion was chosen to be the strain at ultimate tensile stress (UTS), since crack propagation beyond that point occurred in a catastrophic fashion, as will be discussed in **Chapter 4**.

3.7 Interfacial shear strength (IFSS)

The interfacial forces between the dissimilar phases coexisting in a composite system are determining factors to the composite's overall properties. Many fiber/matrix interface characterization methods exist,^{36,100} but not all apply to the nature of the fibers discussed in this work. Discontinuities in natural fiber surfaces, for instance, would not return clear damping patterns in a single-fiber composite test. The most suitable method

was found to be a modified version of the fiber pullout test—the microbond (also known as microbead or microtension) test. The general idea of the test is to deposit a microdroplet of the resin on a fiber strand, covering the entire circumference of the fiber, i.e., all 360 degrees. Then the fiber is pulled at a fixed rate while the droplet is fixed in place using a micro-vice, as illustrated in **Figure 17**. The maximum force reached during the fiber pullout divided by the contact (interface) area between the fiber and resin is the maximum shear stress needed to debond the bead (τ_{\max}).

Resin droplets were deposited by dipping a hydrophobic ultrahigh molecular weight polyethylene (UHMWPE) fiber into the resin, allowing the resin to form a droplet at the bottom tip of the UHMWPE fiber, and then transferring the formed droplet onto the hydrophilic plant fibers, as seen in **Figure 16**. Following that, the resin droplet was dried and cured in an oven, along with the fiber. Because no pressure was applied to cure the microbeads, the curing temperature and time had to be adjusted. The curing conditions for the microbeads were determined based on DSC analyses of the hot-pressed resin sheets versus the thermally cured microbeads. The specimens were placed in a forced-air convection oven (Thermo Fisher Scientific, Isotemp™, Waltham, MA) at 110°C for 30 min. Before testing, the specimens were left to condition at 21°C and 65% RH for 72 h to equilibrate their water content.

Measuring the dimensions of interest (i.e., fiber/resin contact area) is critical to this delicate microbond test. An optical microscope and ImageJ image processor were used to measure jute/SPI contact area, as well as RS fiber thickness. While the RS/SPI contact length and the fiber width were measured using an electronic caliper, since the droplets coating RS exceeded the micron dimension.

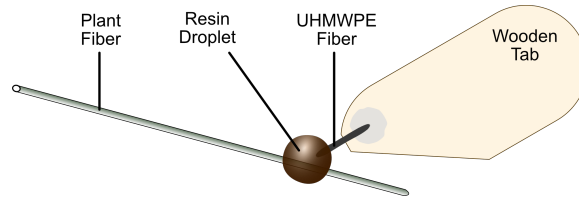


Figure 16. Resin droplet deposition on a plant fiber from an UHMWPE fiber.

A fiber with the microbead was clamped from one end to a universal tensile machine with a 100 N load cell. It was then passed between two blades of a horizontally fixed micrometer (micro-vice), with the microbead being held below the blades. The schematic of the microbond test setup is illustrated in **Figure 17**. These blades prevent the bead from passing through as the fiber is pulled upwards. The fiber was pulled up from the microbead at a crosshead speed of 0.2 mm/min. The results were recorded as force versus extension, and the maximum interfacial strength, or the maximum shear stress τ_{max} , was calculated according to the following equation:

$$\tau_{max} = \frac{F_{max}}{A} \quad (3.1)$$

where τ_{max} is the interfacial strength, F_{max} is the maximum force required to debond the microbead from the fiber, and A is the contact area between fiber and resin droplet.

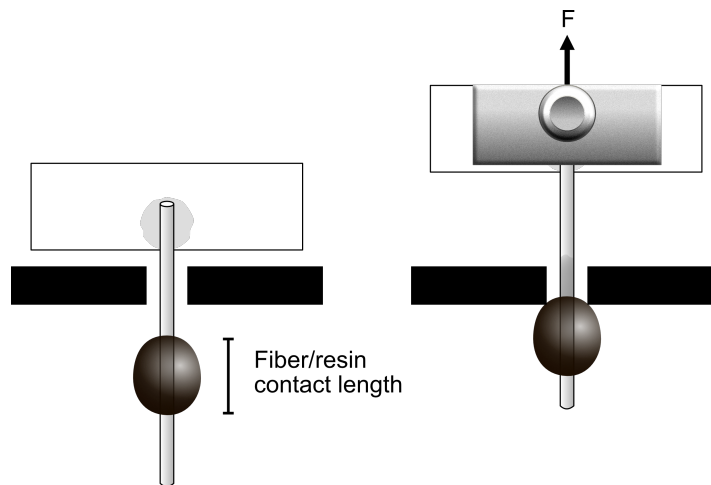


Figure 17. Schematic of the microbond test setup.

3.8 Flexural properties of composites

The flexural properties of the composites were tested using the same Instron universal testing machine as the tensile tests. A three-point-bend fixture provided by the manufacturer was set up and adjusted for each specimen to maintain a ratio of at least 1:16 and at most 1:20 between depth-to-support span (D:L seen in **Figure 18**). The specimens were laser cut to 120 mm × 12 mm rectangles and conditioned at 21°C and 65% RH for 72 h before being tested according to ASTM D790–03. The triple-layered composite specimens were placed on the two bottom loading forces shown in Figure 18 with the outer RS layer facing down. An increased testing rate of 10 mm/min was used as compared to the ASTM recommendation, that is, to observe rupture in the outer surface of the reinforced resin composites. At lower rates, the specimens were found to simply flex with force and not achieve fracture. The ultimate flexural strength (UFS) was found using Eqn. 3.2 and the flexural modulus (E_f) using Eqn. 3.3.

$$UFS = \frac{3PL}{2wD} \quad (3.2)$$

where P is the peak load, L is the support span, w is the width, and D the thickness of the specimen respectively.

$$E_f = \frac{L^3 m}{4wD^3} \quad (3.3)$$

where m is the slope of the initial linear portion of the load-deflection curve. As for the representative flexural test plots, the x -axis was converted from deflection to flexural strain. Thus, flexural stress-strain plots will be discussed in the results section and not stress-deflection.

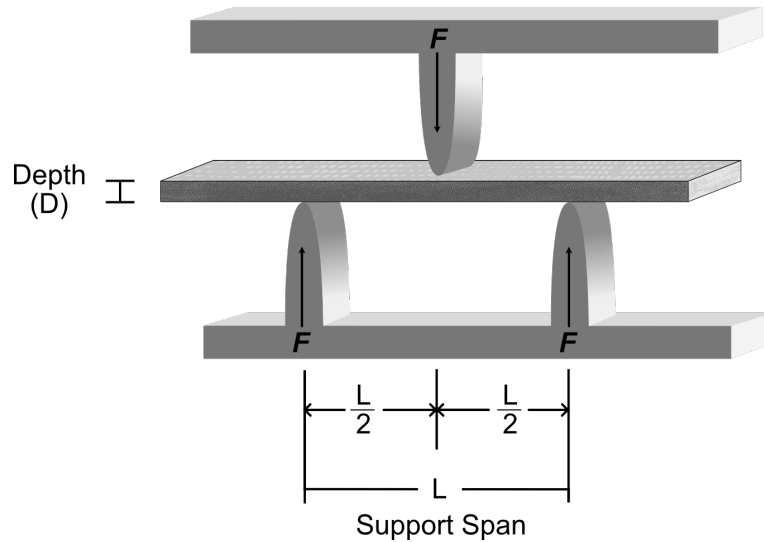


Figure 18. Illustration of 3-point-bend test.

3.9 Scanning electron microscopy (SEM)

This work made use of the field-emission scanning electron microscope (FESEM) (Zeiss, Model No. LEO 1550, Oberkochen, Germany) at the electron microscopy facility of the Cornell Center for Materials Research (CCMR) with support from the National Science Foundation Materials Research Science and Engineering Centers (MRSEC) program (DMR- 1719875). SEM was used to observe the morphology of fibers and resins, fracture surfaces of resins and composites, and the fiber surface topography at the fiber/resin interface.

3.10 Dynamic mechanical analysis (DMA)

Dynamic mechanical properties were characterized using a thermal dynamic mechanical analyzer (TA Instruments Inc., Model No. Q800, New Castle, DE). A strain sweep test was performed to roughly determine the viscoelastic region of the composites,

that is, the range at which a material's response to deformation is both elastic and viscous. This region was found to be below 200°C. In addition, a preliminary stress/strain test was performed to specify the value for the isostress setup.

Specimens were laser cut to dimensions of 5 mm x 60 mm and placed in a dual cantilever fixture. The stress was fixed at 0.1 MPa, frequency at 1 Hz, and amplitude at 1 μm . The test was performed under a temperature range from -10 to 200°C at a ramp rate of 5°C/min.

3.11 *Treatment of DPT*

Date palm fibers were soaked in 5% by volume NaOH (equivalent to 1.25 M) for different periods of time: 3, 6, 9, 12, and 24 h. The solution was prepared by mixing 50 g of NaOH pellets in deionized water and maintaining a 1 liter total volume by adding water until the exothermic reaction has cooled down.

3.12 *Attenuated total reflectance Fourier-transform infrared (ATR-FTIR) spectroscopy*

The effect of alkali treatment on date palm tree fiber surface chemistry was characterized using an FTIR spectrophotometer (Nicolet Magna-IR 560, Thermo Scientific, Waltham, MA). Spectra were taken in the range of 4000–600 cm^{-1} wavenumbers for 32 scans at a resolution of 2 cm^{-1} .

3.13 *Moisture sorption*

The moisture sorption capacities of the composites and their constituents were measured by weighing them using a microscale before and after placing them in a

conditioning room at 21°C and a RH of 65% for 72 h. The composite and resin specimens used in moisture sorption tests are the same laser-cut ones used for tensile and flexural tests, thereby exposing more surface area to humidity as compared to studies that use full composites/panels.

CHAPTER 4: RESULTS AND DISCUSSION

4.1 *Moisture sorption*

SPI resins and natural fibers can readily absorb water because of the polar chemical groups such as amine, hydroxyl and carboxy groups they contain, which give them their hydrophilic characteristic. Water molecules surrounding green composites may also enter through the voids present in resins or at filler/resin interfaces. Once entered, water diffusion then continues through microcracks existing in the resin as well as along microcracks, if present at the filler/resin interface. Water molecules diffused inside the system can settle within those microcracks in the resin or voids through surface adsorption interactions or possibly undergo a capillary motion induced by the flaws in fiber/resin interface. Those pathways direct water molecules toward the water-fostering hydrophilic fibers. The swelling of fibers after moisture absorption illustrated in **Figure 19** induces internal stresses and results in additional micro-cracks in the resin¹²⁶ which, in turn, further enhances water diffusion and destroys the structural integrity of the green composite.¹²⁷

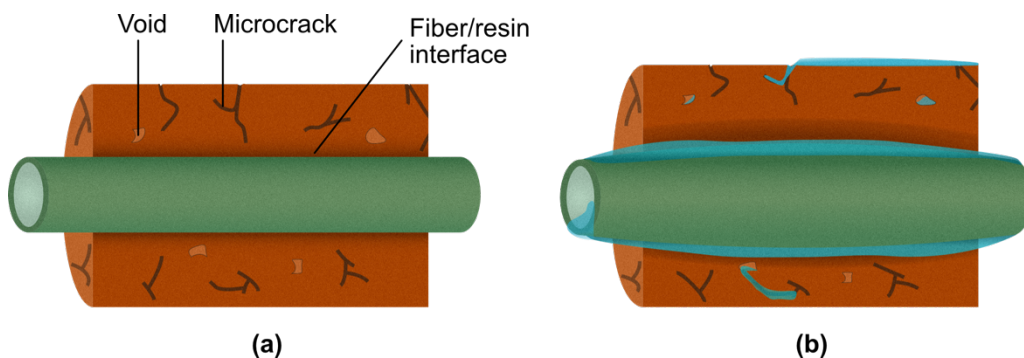


Figure 19. Visualization of green composite swelling mechanism, a) dry fiber/resin and b) swollen fiber/resin.

Water sorption capabilities of RS/JFa/SPI composites were measured as gain in mass and dimensions after conditioning at 21°C and a RH of 65% for 72 h. In addition, separate constituents' mass gains were recorded. **Figure 20** presents values of these gains for composites and their constituents. The results show that RS gained a slightly higher mass than JFa after conditioning (5.5 and 4.1%, respectively) which could be attributed to latter's higher crystalline cellulose content. Both the SPI 12.5 resins used in single- and triple-layered composites showed mass gains of around 9.5%, which is 72% and 132% higher than RS and JFa, respectively. Consequently, all composites (whether S- or T-type) and regardless of fiber load, had gained between 9.5–11.8% of mass, indicating the dominant effect of resin water absorption in the composites. The gain in composite width was negligible and ranged from 0.6% to 1.1% since the fibers were placed with their longitudinal dimension perpendicular to the composite thickness. On the other hand, the thickness showed a significant increase in gain as fiber content increased. In the case of S60, delamination of felted RS from JFa was prominent. This introduced difficulties in precisely measuring thickness and width gains for S60 specimens. T-type composites produced relatively more intact panels and their dimensional analyses were more reliable. T40, T50, and T60 gained a remarkable 10.4, 12.9, and 22.6%, respectively, in thickness. Given their statistically similar mass gains, increasing fiber load seems to significantly harm the composites' structures. This is one indication of the resins being overloaded with fibers.

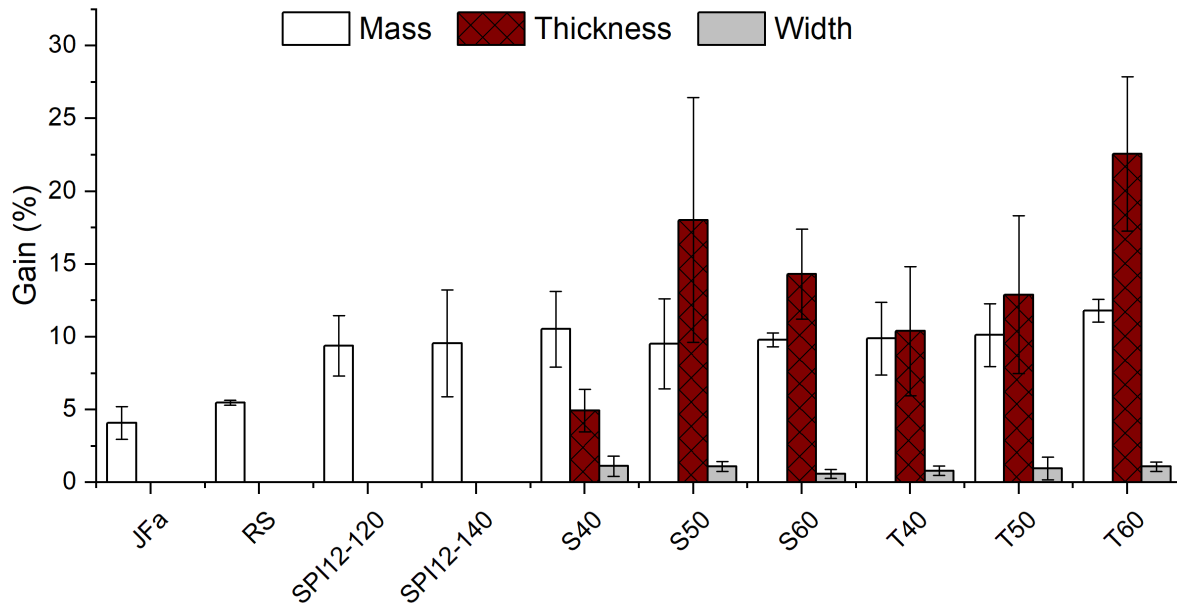


Figure 20. Water sorption data for JFa, RS, SPI resins, and their composites at different fiber loads.

4.2 Tensile properties

To predict the theoretical tensile properties of composites, each constituent was experimentally characterized according to the appropriate ASTM standard. The tensile property data for rice straw, jute fabric, jute yarn, date palm fibers, various SPI resins, and their composites at different fiber contents are presented in the following subsections.

4.2.1 Rice straw

Rice straw fibers (RS) show a broad range in density, diameter, and mechanical properties. The statistical approach to determine the tensile properties of interest resulted in a wide distribution of Young's moduli (E_y) and ultimate tensile strengths (UTS). These

test results are presented in **Figure 21**. The mean values of E_y and UTS for RS were 2.18 ± 1.71 GPa and 31.35 ± 25.19 MPa, respectively. While the standard deviations (SD) of the two characteristics was very high, the density plots help visualize the right-skewness of the data points. In both cases, E_y and UTS, datapoints accumulate reasonably near their means.

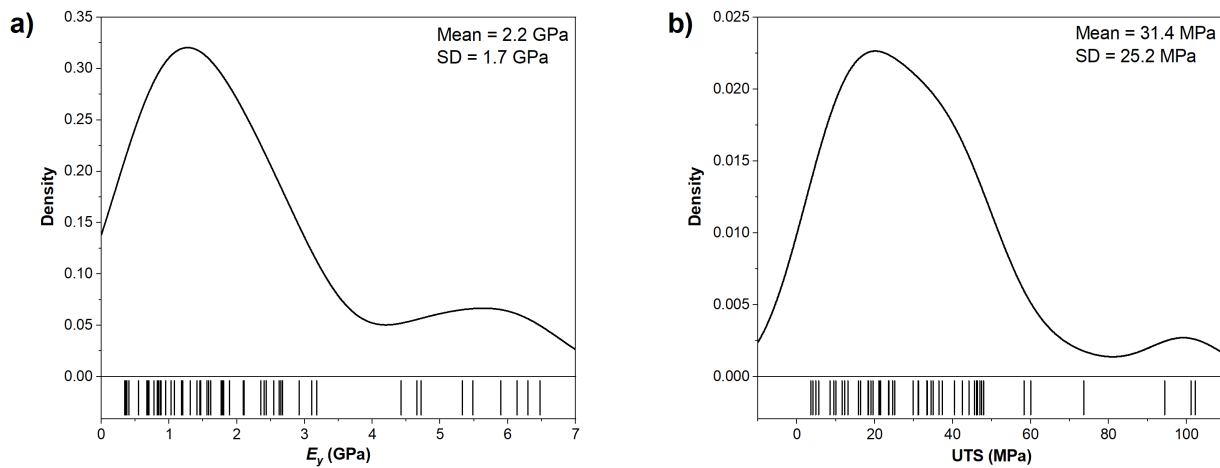


Figure 21. Distribution of rice straw fiber properties a) Young's modulus and b) UTS obtained from fiber tensile test. $N = 53$ specimens.

In addition to the reasons discussed in **Section 2.4** explaining why the properties of natural fibers vary widely, the variability seen here can also be associated with the architecture of RS. A photographic image of a RS segment is shown in **Figure 22**. The nodes seen in Figure 22 are stiff and strong, they are critical to the plant's mechanical support to stay upright, similar to bamboo, and they work as growth reinforcement sites. The region between two nodes, i.e. the internode, is less of a mechanical support region and rather a water and nutrient transport unit. Consequently, it is more compliant and weaker.

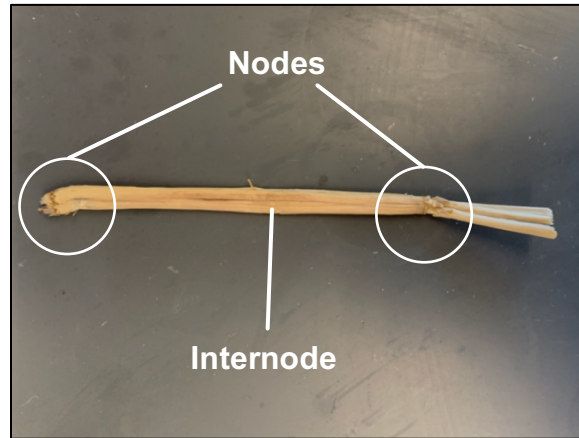


Figure 22. Photographic image of a RS segment indicating an internode between two nodes.

Figure 23 shows a photographic image of a RS after tensile break. **Figure 24** presents a typical stress-strain plot for a RS tensile test and **Table 3** presents the results of 53 RS tensile tests. The brittle nature of RS can be clearly seen in the image, where a post-tensile tested specimen has exhibited an almost ideal brittle fracture propagation across the fracture axis. The brittle nature of the RS is also clear from the strain response to stress seen in the typical stress-strain plot presented in Figure 24. A rapid, almost instantaneous, drop in stress is observed immediately after reaching the UTS, with a few step-like decrements indicating the fracture propagation along fibrils. RS specimens under these testing conditions also showed a low strain at break (mean = 1.7 ± 0.9 %) as presented in Table 3.

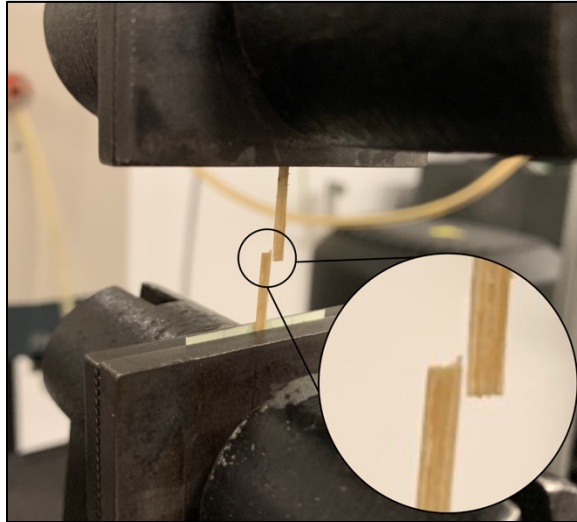


Figure 23. Rice straw broken across its axis after the tension test on a universal Instron testing machine.

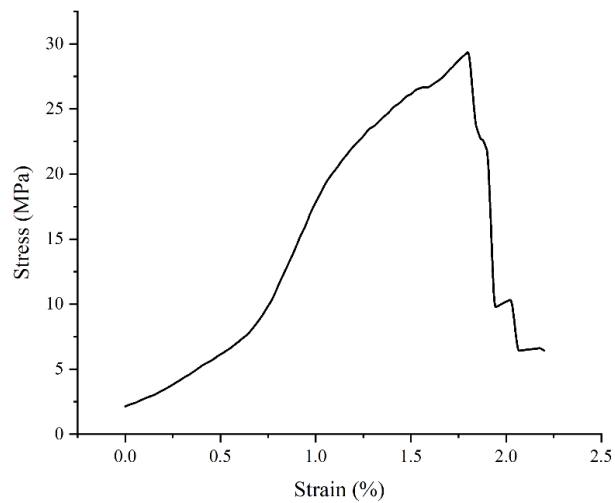


Figure 24. Typical stress-strain plot obtained from RS tensile test.

Table 3. Rice straw tensile properties obtained from tensile test.

E_y (GPa)	UTS (MPa)	Width (mm)	Thickness (mm)	Strain at Break (%)
2.2 ± 1.7	31 ± 25	2.4 ± 1.2	0.2 ± 0.1	1.7 ± 0.9

$N= 53$.

4.2.2 *Jute yarn and fabric*

The tensile properties of fibrous assemblies and composites primarily depend on the fiber properties and the geometry of the assembly. Ideally, fibers would be axially aligned with the load axis and cohesively assembled resulting in a high packing density to obtain the full loading efficiency. However, this is rarely the case in most applications. Twisting short staple fibers into continuous yarns is the most common way to overcome many of the shortcomings of natural fibers (e.g. inhomogeneity and random distribution of volume/density/length). While twist provides friction and cohesiveness through which strength of the yarn is realized (this is especially true with staple fibers such as JF used in this research), it has its implications on the assembly's mechanics. Starting from Gegauff's simple cosine-squared rule that relates the Young's moduli of straight fibers to those of twisted yarns of the same fibers, and up to the more sophisticated models thereof; they all agree on the loss of stiffness (Young's modulus) from fiber to twisted yarn.^{128,129} Weaving yarns into fabric introduces even more deviations to the perfect axial alignment of fibers. Pierce introduced a very simple and limited model for plain weave mechanics, yet it identified critical parameters.¹³⁰ Of these parameters which are known to affect stiffness and strength are crimp, thread spacing, and thread height (diameter).

Table 4 presents the experimental results of jute fabric and yarn tensile tests. As seen in the results, twisted jute yarns have a E_y close to two orders of magnitude higher than JFa, and UTS of approximately one order of magnitude higher than JFa, but only half the elongation at break. It is also evident that the fabric in warp direction is stiffer and stronger than the weft direction. Most commonly, the warp (or machine) direction is intentionally made stronger because of the high cyclic tension the yarns undergo during

the weaving process. Weft yarns, on the other hand, are simply laid in and do not have much tension during fabric manufacturing. The higher tension on warp yarns causes straightening of the yarns and a lower crimp along that axis, which also reflects on the higher stiffness it exhibits.

Table 4. Tensile properties of JFa in warp and weft directions and twisted jute yarn.

Jute Specimen	Thickness (mm)	E_y (GPa)	UTS (MPa)	Strain at Break (%)
Fabric-warp	0.90 ± 0.06	0.35 ± 0.04	20 ± 2.8	9.0 ± 1.3
Fabric-weft	0.91 ± 0.04	0.23 ± 0.03	14.8 ± 2.1	10.6 ± 0.9
Twisted yarn	0.41 ± 0.02	14.9 ± 2.8	323 ± 57	5.8 ± 1.5

N = 12 for each fabric direction and 7 for twisted yarn.

Figure 25 shows typical plots of the strain responses to stress from uniaxial tensile tests performed on JFa in warp and weft directions. Both plots follow a typical woven fabric stress-strain plot, starting with straightening of the crimp region,¹³¹ where a relatively large strain (up to about 2% in this case) is observed at very low stresses. It is at the point where the yarns are getting straightened, overcoming the crimp, which does not require large stresses. As the yarns are straightened at the end of this region, the crimp approaches zero. The straightened yarns then start to take up more load and enter the elastic region, although there is some fiber slippage within the yarns. After reaching UTS, catastrophic failure of yarns and some fibers can be witnessed, which is accompanied by rapid decrease in stress. This is followed by a stepwise fall in stress that can be correlated to progressive breaking of yarns.

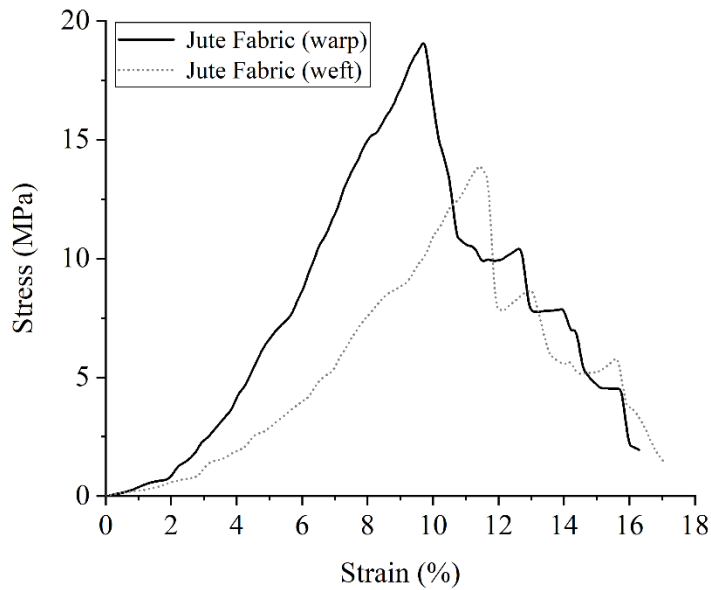


Figure 25. Typical stress-strain plots for woven JFa in warp and weft directions.

4.2.3 *Date palm tree (DPT) fibers*

The tensile properties of untreated and alkali (NaOH) treated DPT fibers are presented in **Table 5**, and their typical stress-strain plots are illustrated in **Figure 26**. As expected, the alkali treatment enhanced stiffness and strength of the fibers. With increased treatment time, the slope of the stress-strain plot in the region prior to UTS increased. Also, the step-like failure seen in the 0 h specimen does not appear in any of the treated fibers, indicating an enhancement in their brittleness. Alkali treatment (commonly called mercerization in cotton) is known to remove the soluble amorphous components of plant cell walls, namely, lignin, hemicellulose, pectin, and some dirt residue.^{82–84,105,123} This leaves the fibers with a higher crystalline cellulose content. In the present study, a low NaOH concentration was used to avoid any alteration to the native cellulose I crystal structure.¹³² Treating DPT with 1.25 M NaOH for 12 h was determined

to be the best condition for the tested batches. The alkali treatment resulted in over 100% improvement in both E_y and UTS as compared to untreated fibers. At the same time, the elongation at break stayed within one SD range throughout the samples and did not seem to change a lot. The reason could be that as alkalization enhanced the crystallinity,¹³³ it also exposed cellulose to plasticization during the humidity conditioning step.⁶²

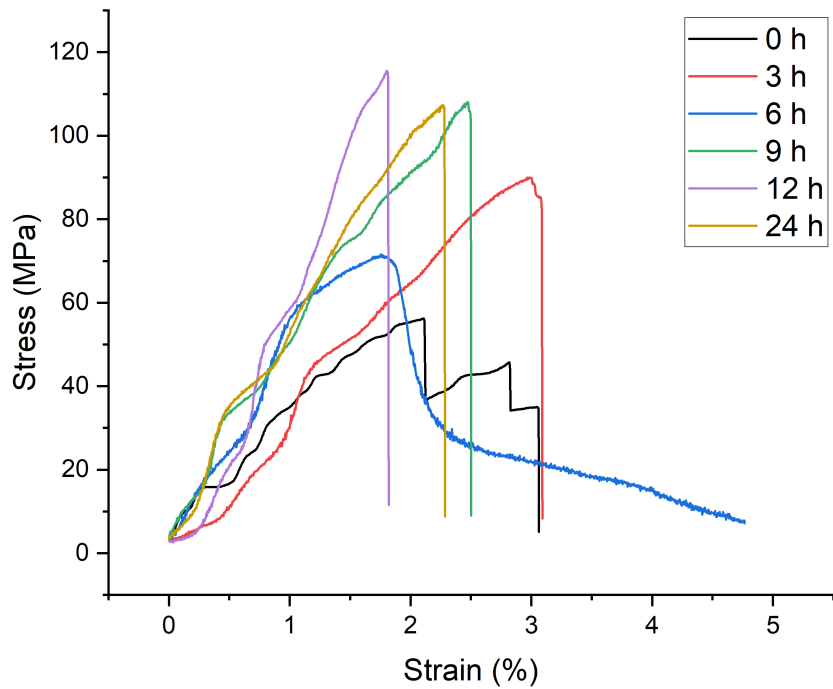


Figure 26. Typical stress-strain plots for untreated and NaOH treated DPT fibers.

Table 5. Tensile properties of untreated and NaOH treated DPT fibers at different treatment times.

Treatment Time (h)	E_y (GPa)	UTS (MPa)	Strain at Break (%)
0	6.5 ± 2.5	51.9 ± 12.7	2.5 ± 0.9
3	10.2 ± 4.3	80.1 ± 28.0	2.8 ± 1.1
6	14.5 ± 4.6	85.8 ± 28.3	2.1 ± 0.7
9	12.3 ± 4.7	73.0 ± 30.0	1.7 ± 0.5
12	17.1 ± 9.1	107 ± 44.6	2.3 ± 0.7
24	14.3 ± 7.1	95.2 ± 32.5	2.0 ± 0.7

$N = 12-22$ specimens for each sample.

4.2.4 SPI resins

Crosslinked SPI resins have been thoroughly studied by the group.^{36,49-52,54,55,134} However, preliminary tests were performed in this study to determine the optimal amount of D-sorbitol plasticizer to be used. **Table 6** presents the tensile test results of crosslinked SPI resins with different D-sorbitol contents. The main criterion set in choosing the resin was for it to have at least twice the strain at break for the least brittle reinforcement, i.e., JFa. Thus, the resin with 0% D-sorbitol content was eliminated since it fractured at strains lower than those of jute fabrics. The 5% plasticizer content resin resulted in the highest E_y as well as one of the highest UTS values. The decrease in strength and stiffness with increased plasticization seen in Table 6 is a response to increased chain sliding caused by the significant amount of free volume brought in by the plasticizer. It is also noted that beyond the 10% plasticizer content, the ductility begins to deteriorate. This indicates that plasticizer molecules may have agglomerated between the polymer chains and caused soft points (defects).

Table 6. Tensile properties of SPI pH 12.5 resins at different plasticizer content.

D-sorbitol Content (wt%)	E_y (GPa)	UTS (MPa)	Strain at Max. Load (%)	Strain at Break (%)
0%	0.51 ± 0.18	5.37 ± 2.51	5.04 ± 3.29	8.89 ± 11.64
5%	0.42 ± 0.08	6.90 ± 0.74	11.82 ± 1.27	68.49 ± 19.80
7.50%	0.32 ± 0.04	7.15 ± 0.51	11.97 ± 0.98	89.93 ± 39.77
10%	0.35 ± 0.04	6.84 ± 0.65	13.17 ± 1.11	102.83 ± 16.74
12.50%	0.35 ± 0.04	6.03 ± 0.33	14.46 ± 2.38	59.39 ± 36.08
15%	0.36 ± 0.03	6.49 ± 0.54	14.95 ± 1.04	86.81 ± 19.69

$N=7$ for each resin.

Using the same plasticizer and crosslinker content, three SPI resins were produced and characterized. The first two SPI resins were denatured at 12.5 pH and cured at 120°C (SPI12-120) and 140°C (SPI12-140). The third resin was denatured at 9.5 pH and cured at 120°C (SPI9). **Table 7** presents the results of tensile tests performed on these resins and **Figure 27** illustrates the stress-strain plots of these tests. Typical strain hardening was observed for the SPI9 resins during the tensile tests. The stress-strain plots show bell-shaped regions after the yielding point, as seen in Figure 27. This mechanical response is due to possible orientation of polymer molecules under large strain-induced deformation. When the molecules are oriented to their maximum possible under these test conditions, UTS is observed as the peak of that bell curve. After which, uniaxial tension overrides the resin, and the ductility of the resin determines the ductile fracture point. For the two 12.5 pH resins (SPI12-120 and SPI12-140), the bell shapes are not quite discrete. Instead, they follow a typical ductile material's response to load. In these cases, the stress required to yield is much lower than UTS. Also, their lower stiffness, described by E_y , accounted for shifting UTS to a higher strain value. As seen in Table 7, the SPI12-

120 and SPI12-140 resins are weaker, more compliant, but more ductile than the SPI9 resins.

Table 7. Tensile properties of three different SPI resins denatured at different pH levels and/or cured at different temperatures.

Resin	E_y (GPa)	UTS (MPa)	Strain at Max. Load (%)	Strain at Break (%)
SPI9	0.72 ± 0.12	16.78 ± 0.73	6.69 ± 0.52	25.45 ± 4.32
SPI12-120	0.35 ± 0.10	5.92 ± 1.18	11.12 ± 2.24	46.37 ± 24.40
SPI12-140	0.32 ± 0.04	7.19 ± 1.19	9.16 ± 2.14	36.46 ± 14.83

N= 7 for pH 9.5 resin and 16–17 for pH 12.5 resins.

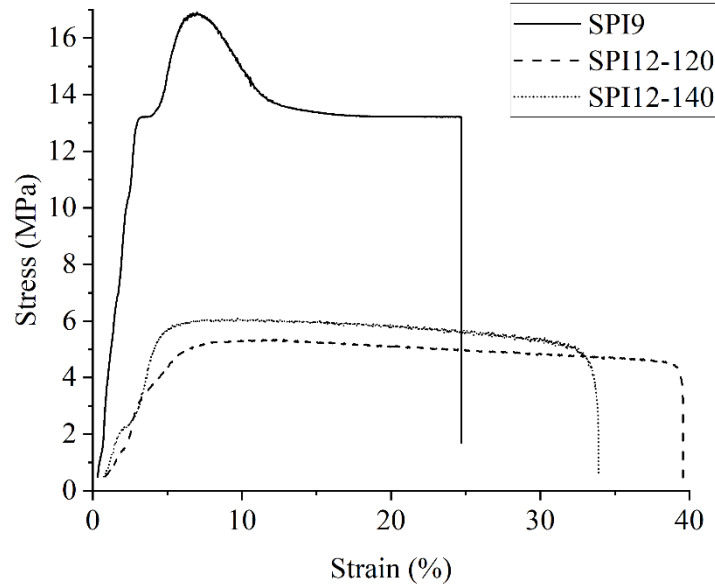


Figure 27. Stress-strain plots for three SPI resins obtained from standard tensile tests.

4.2.5 Composites

From previously obtained tensile properties of the components, hybrid composites' theoretical tensile properties were predicted following the widely used rule of hybrid mixtures (ROHM),¹³⁵⁻¹³⁷ which is a modified version of the simple rule of mixtures (ROM). Theoretical and experimental RS/JFa/SPI composite tensile properties are discussed in the next two sections.

4.2.5.1 Hybrid composites – theoretical tensile properties

The main assumption in the ROHM is that reinforcements work independent of each other, as if there were two separate composites. Consequently, it assumes no interaction between the separated composite systems. Obviously, that is not the case for the composites prepared in the present study, especially since the fibers were felted

together into a cohesive fabric. To find Young's modulus of the RS/JFa/SPI composite (E_C) according to ROHM, the general equations 4.1 and 4.2 were used:

$$E_C = E_{C1}V_{C1} + E_{C2}V_{C2} \quad 4.1$$

$$V_{C2} = 1 - V_{C1} \quad 4.2$$

where E_{C1} and V_{C1} are Young's modulus and volume fraction of RS/SPI composite system, respectively, and E_{C2} and V_{C2} are Young's modulus and volume fraction of JFa/SPI composite system, respectively. The values of E_{C1} and E_{C2} are found using ROM equations 4.3 and 4.4:

$$E_{C1} = E_{f1}V_{f1} + E_mV_{m1} \quad 4.3$$

$$E_{C2} = E_{f2}V_{f2} + E_mV_{m2} \quad 4.4$$

where E and V are Young's modulus and the volume fraction, and the subscripts $f1$, $f2$, $m1$, and $m2$ refer to rice straw, jute fabric, and resin (matrix) of RS/SPI composite, and resin of JFa/SPI composite, respectively. Using Eqns. 4.3 and 4.4, Eqn. 4.1 can be rewritten as Equation 4.5:

$$E_C = (E_{f1}V_{f1} + E_mV_{m1})V_{C1} + (E_{f2}V_{f2} + E_mV_{m2})(1 - V_{C1}). \quad 4.5$$

To find volume fraction of the RS/SPI composite (V_{C1}), the relation between SPI resin and RS was found through mass and density conversions using Eqn 4.6:

$$V_{C1} = \frac{\frac{m_m + m_1}{\rho_m} + \frac{\rho_1}{\rho_2}}{\frac{2m_m + m_1 + m_2}{\rho_m} + \frac{m_1}{\rho_1} + \frac{m_2}{\rho_2}} \quad 4.6$$

where ρ stands for density and subscripts 1, 2, and m are for RS, JF, and SPI resin, respectively. The mean density values of rice straw and jute fibers were found in the

literature to be 0.51 g/cm³* and 1.41 g/cm³, respectively (refer to Table 2).^{82,107-112} The mass of resin m_m with different fiber load x_f (i.e., 0.4, 0.5, and 0.6) can be calculated according to Eqn. 4.7. Putting Eqn. 4.7 in Eqn. 4.6 produces the relation found in Eqn. 4.8.

$$m_m = \frac{2m_1(1-x_f)}{x_f} \quad 4.7$$

$$\therefore V_{C1} = \frac{\left[\frac{\left(\frac{2m_1(1-x_f)}{x_f} \right)}{\rho_m} \right] + \frac{m_1}{\rho_1}}{4 \left[\frac{\left(\frac{m_1(1-x_f)}{x_f} \right)}{\rho_m} \right] + \frac{m_1}{\rho_1} + \frac{m_2}{\rho_2}} \quad 4.8$$

The values for V_{C1} at the different fiber loads are tabulated in **Table 8**.

Table 8. Values of V_{C1} as calculated for the three different T-type composite systems.

Composite System	V_{C1}
T40	0.58
T50	0.60
T60	0.63

Equation 4.5 represents the upper bound of the composite's Young's modulus. That is because it describes an isostrain case, where the stiffness in the elastic region is dictated

* This value is the average between the upper bound of bale RS density and the lower end of pelleted RS density, since RS in this study was received as bale, felted, and then hot-pressed.

by the relatively brittle material.¹³⁸ This would result in a higher Young's modulus according to the relation:

$$E_y = \frac{\sigma}{\varepsilon} \quad 4.9$$

where σ is the stress and ε is the strain. Since jute was a plain weave fabric, the isostrain scenario was applied to both warp and weft directions. **Figure 28** illustrates a schematic of the separated hybrid composite systems under load, with the two isostrain and one isostress axes indicated. It is important to mention the additional assumptions associated with such a fixture; laminae are assumed to have equal (same) Poisson ratios and null force interactions in between, and all fibers are assumed to be axially aligned with the load axis.

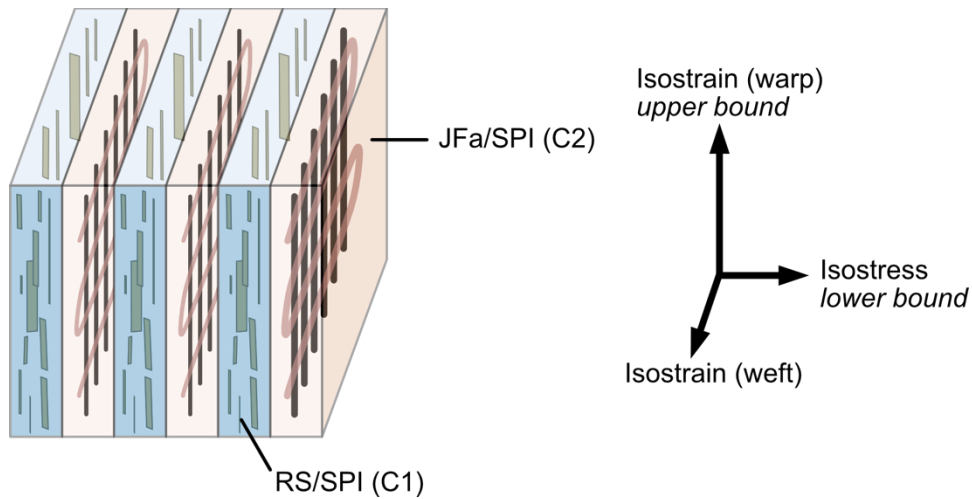


Figure 28. Schematic of the separated RS/SPI and JFa/SPI composites for the purpose of hybrid composite theoretical analysis.[†]

[†] For demonstrational purposes, RS is shown aligned in the warp direction. This is true for the isostrain warp case. However, and since the ROHM assumes separate composites, RS is also aligned in the weft direction in the weft isostrain calculations.

The experimental preparation of the composites was carried based on mass ratio measurements between fiber and resin. A conversion to volume fractions is required to apply the ROHM. The density of the resin (ρ_m) was calculated (at a water content of 12%) as follows:

$$\begin{aligned}\rho_m &= \chi_{SPI}\rho_{SPI} + \chi_{GA}\rho_{GA} + \chi_{D-SORB}\rho_{D-SORB} + \chi_{NaOH}\rho_{NaOH} \\ &+ \chi_{DI-H_2O}\rho_{DI-H_2O} = \left(\frac{15g}{45.25g}\right)_{SPI} \left(\frac{1.3g}{cm^3}\right) + \left(\frac{6g}{45.25g}\right)_{GA} \left(\frac{1.062g}{cm^3}\right) \\ &+ \left(\frac{0.75g}{45.25g}\right)_{D-sorb} \left(\frac{1.596g}{cm^3}\right) + \left(\frac{11.5g}{45.25g}\right)_{NaOH} \left(\frac{1.15g}{cm^3}\right) + \left(\frac{12g}{45.25g}\right)_{H_2O} \left(\frac{1g}{cm^3}\right) \\ &= 1.156 \frac{g}{cm^3}\end{aligned}$$

where χ is the mass fraction of the component in the resin. As mentioned in the experimental section, mass ratio between the two fibers was held at 1:1 during preparation, and thus volume fractions of the composite constituents at different fiber loads were calculated. Mass and volume fractions of composite components are presented in **Table 9**.

Table 9. Volume fractions of RS/JFa/SPI composites as calculated from mass-to-volume conversion.

Composite System	V_m	V_{f1}	V_{f2}
T40	0.49	0.37	0.13
T50	0.39	0.45	0.16
T60	0.30	0.51	0.19

As for the isostress case, ROHM is given by Eqn. 4.10:

$$E_C = \left[\frac{V_{C1}}{E_{C1}} + \frac{V_{C2}}{E_{C2}} \right]^{-1} \quad (4.10)$$

The relation given by Eqn. 4.10 represents the theoretical lower bound of Young's modulus that the composite would exhibit.¹³⁸ The constant stress allows for the relatively ductile material to elongate to its maximum capabilities, hence lowering stiffness in the elastic region.

As mentioned earlier, ROHM assumes two separate composites given by 1) RS/SPI and 2) JFa/SPI. **Table 10** presents the parameters, i.e., volume fractions, needed to solve for Eqn. 4.3–4.5.

Table 10. Volume fractions of the theoretically separate RS/SPI and JFa/SPI composites.

Composite System	V_{m1}	V_{m2}	V_{f1}	V_{f2}
T40	0.57	0.79	0.43	0.21
T50	0.47	0.71	0.53	0.29
T60	0.37	0.62	0.63	0.38

The hybridization of PMC reinforcement has its implications on the UTS of the hybrid composites. Generally in hybrid composites, UTS does not exactly obey the ROM.¹³⁹ This is simply because the reinforcing material that is more brittle breaks first at its fracture strain, meaning that its support for carrying load is lost at a lower strain which overloads the other materials.¹³⁹ This results in a complex stress sharing mode between the two fibers. Despite that, UTS of the composite is bound by the components' UTS values as well as their fiber loading %. Furthermore, ROM can be modified to produce an empirical ROHM relation for the strength of hybrid composites, similar to the logic followed for elastic modulus.^{136,140} UTS was accounted as the sum of the volumetric fractions of the two theoretically independent composites. Hence, theoretical UTS for the

hybrid composites was predicted as per the equations 4.11 to 4.14, to observe its deviation from experimental values:

$$UTS_C = UTS_{C1}V_{C1} + UTS_{C2}V_{C2}, \quad 4.11$$

$$UTS_{C1} = UTS_{f1}V_{f1} + UTS_mV_{m1}, \quad 4.12$$

$$UTS_{C2} = UTS_{f2}V_{f2} + UTS_mV_{m2}, \quad 4.13$$

$$UTS_C = (UTS_{f1}V_{f1} + UTS_mV_{m1})V_{C1} + (UTS_{f2}V_{f2} + UTS_mV_{m2})(1 - V_{C1}) \quad 4.14$$

where V is the volume fraction, and subscripts C , $C1$, $C2$, and m denote the hybrid composite, RS/SPI composite, JFa/SPI composite, and SPI resin, respectively.

Table 11 presents a summary of the Young's moduli and UTS values that were theoretically predicted following ROHM for the hybrid RS/JFa/SPI composites, in both warp and weft directions, and at three different fiber contents, 40, 50 and 60%.

Table 11. Theoretical Young's moduli and UTS calculated according to ROHM.

Composite System	Theoretical E_y (GPa)			Theoretical UTS (MPa)	
	Isostrain (warp)	Isostrain (weft)	Isostress	Isostrain (warp)	Isostrain (weft)
T40	1.23	1.22	0.259	20.20	19.73
T50	1.32	1.31	0.255	21.65	21.04
T60	1.40	1.38	0.250	23.00	22.26

4.2.5.2 Hybridization effect from an experimental uniaxial point of view

To better understand the effect of reinforcement hybridization on the tensile properties of the hybrid RS/JFa/SPI composites, nonhybrid (single reinforcement) RS/SPI and JFa/SPI composites were fabricated separately and tested for their tensile properties. **Figure 29** shows stress-strain plots of conditioned triple-layered nonhybrid JFa/SPI and RS/SPI, and triple-layered hybrid RS/JFa/SPI and composites. **Table 12** presents the results of the same tensile tests.

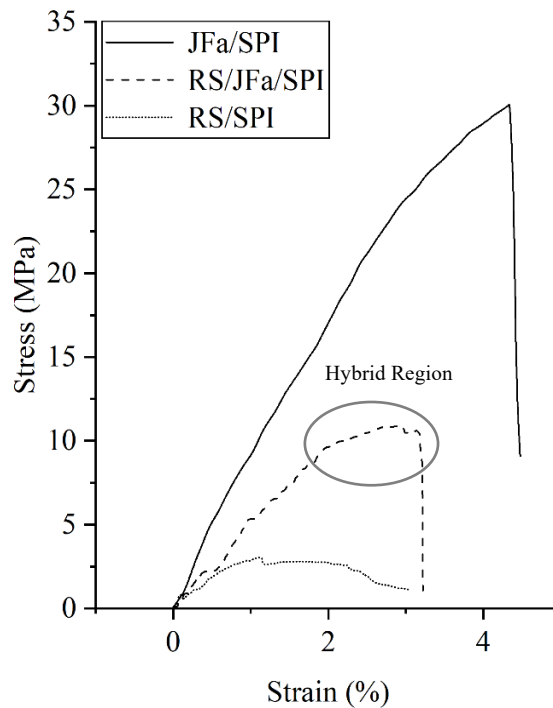


Figure 29. Stress-strain plots of three conditioned triple-layered composites (JFa/SPI, RS/JFa/SPI, RS/SPI) all made with 40 wt% fiber load.

Typical stress-strain plots of fabric reinforced PMC (like the one seen in Figure 29 for JFa/SPI) start with a linear increase in load until UTS, followed by rapid (brittle) drop in stress. Hybrid composites, on the other hand, show a plateau known as the “hybrid

region"¹³⁹ (circled in Figure 29) at strains preceding UTS. In this region, the premature consecutive crack propagations occurring primarily in the brittle fiber (RS) cause loads to transfer to the other fiber (JFa). This creates concentrated stress points on the stronger fibers causing them to fail at a lower strain. Beyond the hybrid region, the stress begins to exhibit a stepwise stress change: repetitive steep falls followed by sustained stresses under increasing strain. This behavior indicates successive failure of different parts and components.

Young's modulus and UTS values of hybrid RS/JFa/SPI composites fall in between nonhybrid RS/SPI and JFa/SPI composites as can be seen in Table 12. The strain to achieve UTS decreased from 4.14% in JFa/SPI to 2.68% in the hybrid RS/JFa/SPI. Looking at the RS/SPI plot, the effect of randomized fiber lengths and orientations can be observed by the arch-shaped stress-strain plot. Since RS fibers were non-directional, or random, the stress sharing between RS fibers did not fail consecutively in a rapid fashion. Broken oriented fibers would instead transfer the stress onto other fibers through the matrix causing the stress-strain curve to exhibit stepwise fall in stress. Whereas those not aligned RS fibers straightened up to the extent possible.

Table 12. Tensile properties of triple-layered and conditioned composites JFa/SPI, RS/JFa/SPI, and RS/SPI with 40% fiber loads each.

Type of Composite	E_y (GPa)	UTS (MPa)	Strain at Max. Stress (%)
JFa/SPI	1.01 ± 0.06	27.49 ± 2.71	4.14 ± 0.28
RS/JFa/SPI	0.88 ± 0.27	10.55 ± 3.40	2.68 ± 0.65
RS/SPI	0.48 ± 0.13	3.81 ± 1.07	1.75 ± 0.56

N= 6 for JFa/SPI, 38 for RS/JFa/SPI, and 10 for RS/SPI.

4.2.5.3 Hybrid composites – experimental tensile properties

The tensile tests of RS/JFa/SPI composites were performed in both warp and weft directions as well as before and after conditioning the specimens. In addition to observing the hybrid composites' mechanical response in tensile, the goal was to characterize the effect of moisture sorption on mechanical properties, including the structural disturbances it may cause to the composites.

In the wood fiber-based composite industries (e.g., the plywood industry), there are certain mechanical properties used to characterize composites and panels. Typically, stiffness, tensile strength, elongation to break, and sometimes toughness are the parameters most used to describe a panel's tensile characteristics. It is important to identify the design stage / scale that the composite tests characterize. From an engineering viewpoint and according to the *Testing Pyramid* (or the *Rouchan Pyramid*) shown in **Figure 30**, mechanical characterization of materials can start at a coupon (specimen) level, and scale up to partial structural elements, structural sub-components and components, and end with a full-scale test of the final engineered structure.^{141,142} The tests of course could go down in scale, to a crystal (micromechanical) or even an atomic level. As much as researchers would appreciate a sequential hierarchical translation in mechanical properties from one scale to another, it is very difficult to achieve. Hence the crucial distinction between 'mechanics of materials' and 'mechanics of structures' often arises. For instance, elastic properties obtained from a macro-scale bulk-material mechanical test under very specific testing parameters could not possibly describe, or even imply the micromechanical characteristic of a material or a component. While this research work

produced structural elements, i.e., composite sheets (*Level 2* in Figure 30), tests were performed only at the specimen scale (*Level 1* in Figure 30).

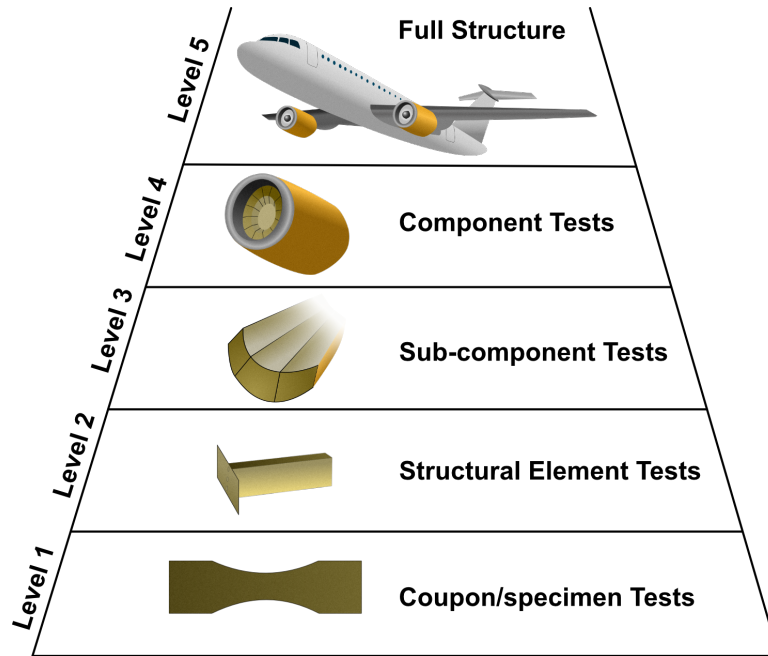


Figure 30. Rouchan pyramid explaining the hierarchy of testing composite materials and structures. Note: recreated based on *Lopes et al. (2016)*¹⁴² depiction.

Since commercial-scale low mechanical resistance composites were produced in this work, the analysis was focused on the engineering elastic properties, with insights borrowed from the materials science and fiber science fields. E_y was measured from the slope of the stress-strain plots and was determined as the slope of the initial linear region. The start point of the slope calculation was taken after 0.5% strain value, to avoid noise due to specimen straightening while removing possible slack and/or crimp. Then a representative linear region was chosen with the end point not exceeding 50% UTS. The reason being that hybrid green composites may exhibit several linear regions prior to UTS

because of various components having different stiffnesses as well as fracture strains. They also have inconsistent yielding points, that is, if there is a clearly identifiable point.

Particularly for the composites presented in this study, the stress-strain plots were seen to be closer to the definition of brittle materials than ductile. **Figure 31** illustrates typical stress-strain plots for composites S40, S50, S60, T40, T50, and T60 obtained from ASTM standard tensile tests performed in the warp and weft directions. The brittle-like behavior is clear from these plots. It is also obvious how UTS could also be the yielding point, and that fracture propagation happens rapidly afterwards.

Hybridization as well as random orientation and the presence of RS in random geometries divert the applied uniaxial stress along the fibers in shear, leading to extended stress bearing at lower loads. This behavior could be seen for instance in Figure 31b for T40 composites. All plots in Figure 31 show a stepwise stress incline behavior right until UTS is reached, as well as a random-fashioned rapid decline beyond that point. This behavior is similar to the tensile response obtained for the jute fabric. In fact, looking closely at T60 in the weft direction, Figure 31d, beginning from ~4% strain and until strain at UTS, the stress-strain response is very close to that seen for JFa in the weft direction (Figure 25). Prior to that region, a compliant elastic region followed by a flat segment can be observed. This can be attributed to the minimal amount of resin holding the fibers in place until a certain load (~2 MPa). After that load is exceeded, yarns/fibers begin to straighten and uncrimp, and the response begins to seem close to that obtained for JFa, as most load is taken up by the JFa—the strongest element in the composite.

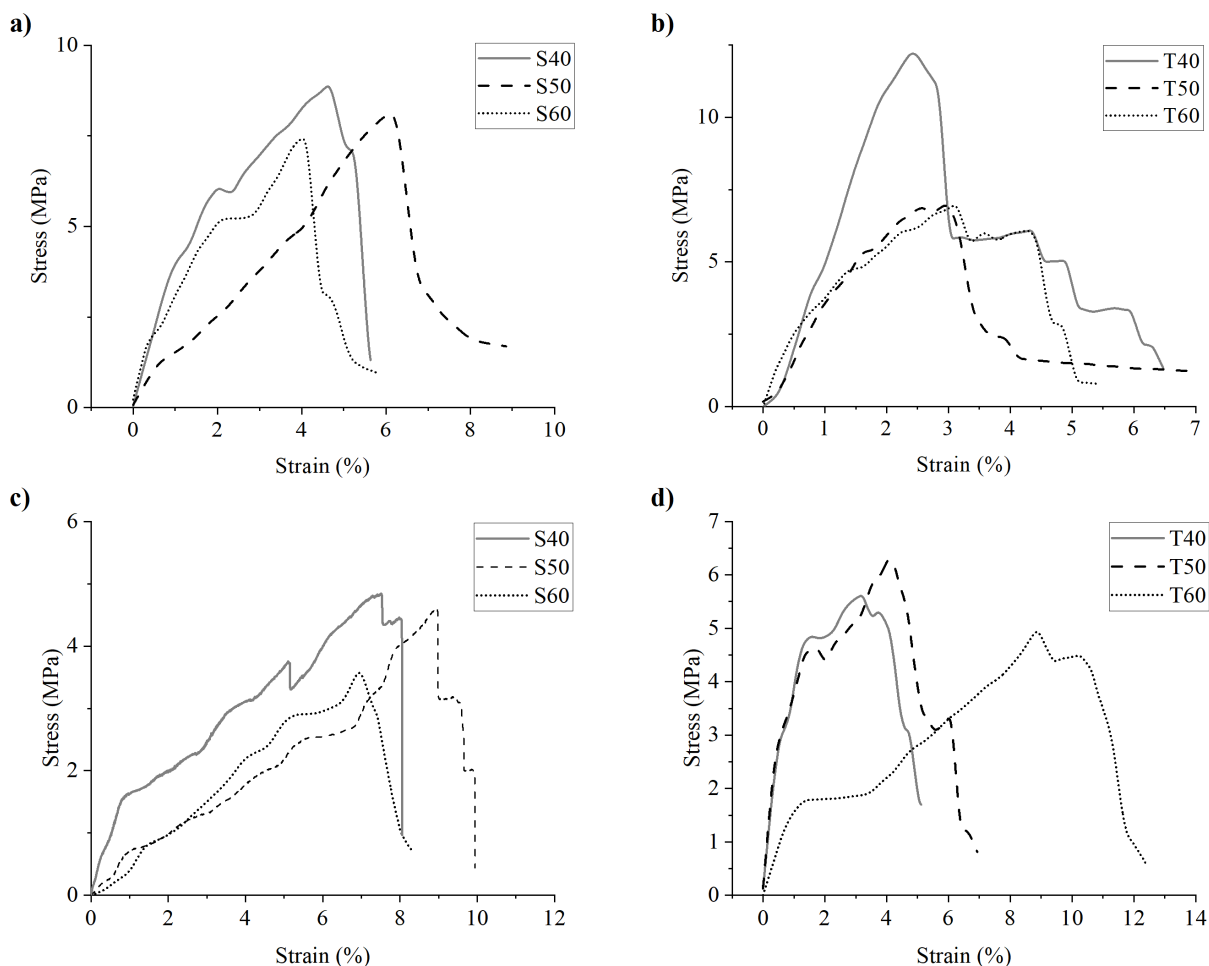


Figure 31. Typical stress-strain plots of conditioned a) single-layered composites in warp direction, b) triple-layered composites in warp direction, c) single-layered composites in weft direction, and d) triple-layered composites in weft direction.

Although higher toughness was considered when plasticizing the SPI resins, the key parameters of interest for the RS/JFa/SPI composites were E_y , UTS, and fracture strain (strain at UTS). The latter parameter was chosen as the fracture point as opposed to the more common “elongation at break”. This is because of the highly randomized failure mode of these types of composites. For example, in Figure 31b, T40 complete failure can

be seen to occur after five distinct step drops in stress. T50, on the other hand, has a single step failure mode, yet beyond that point, the specimen continues elongating under low stress. While the stress applied on T60 seems to fail in three steps. As a result of this inconsistency, the composite failure in terms of elongation at break point can be difficult to determine.

Figure 32 visualizes datapoints for E_y , UTS, and strain at UTS for S- and T-type composites in the warp direction. **Table 13** and **Table 14** present the parameters of interest for dry and conditioned composites, respectively, in the warp direction. Statistical significance of the results in this section were examined using a conservative t -test with significance level $\alpha = 0.05$, especially since the SD error bars in Figure 32 often overlap. S-type composites showed higher SD values for all measured parameters reported as can be expected. The lack of volume in such composites exposes their defects. Additionally, the higher surface area per unit volume that is exposed to humidity during conditioning leads to lower stiffness and perhaps more structural defects.

Dry S-type composites in warp direction lose stiffness (with statistical significance) at increased fiber load. This may be an indication of weak fiber/resin interfacial interaction,¹⁴³ or possibly a lack of uniform resin impregnation in the system, or dry resin being more brittle which develops microcracks. Between the conditioned S-type composites in the warp, the only statistically significant difference found between E_y values (means) was between those of S40 and S50 ($P = 0.0002$), while each of these overlapped with S60. This *no-trend* result confirms the inconsistency of S-type composite properties. In terms of UTS, however, both dry and conditioned S-type composites have almost identical strengths. The strain at maximum load increased after conditioning by

207, 168, and 114% for S40, S50, and S60 composites, respectively. This behavior was expected since water plasticizes the resin rather than the fibers, and thus the effect water would have on a composite would increase with higher resin content.

The moduli of dry T-type composites in the warp direction had averages and SD within the same range but were statistically distinct as per the *t*-test. That distinction applied to comparing data sets of dry and conditioned, as well as comparing the three different fiber loads. The standard deviations were much smaller than S-type composites as was expected because of the increased overall volume and mass of composites which averages out the random defects. This allows for more stress transfer to occur as well as to provide support to defects found in resins and fibers. When conditioned, T-type composites also lose some degree of stiffness. The percent loss in E_y values for T40, T50, and T60 after conditioning was 17%, 33%, and 64%, respectively. There seems a significant deterioration of E_y with increased fiber content, a clear indication of the weakness of fiber/resin interface. Nevertheless, these composites show a higher resistance to E_y drop than S-type composites. The drops in E_y values were 129%, 155%, and 18% for S40, S50, and S60 composites, respectively. Notably, S60 showed the least drop in E_y because its mean under dry condition was very low to begin with (0.58 GPa).

UTS was remarkably preserved for all composites after conditioning and falls within a similar range for all, with an average of the means equal to 8.70 ± 1.42 MPa for the six dry composites, to 8.79 ± 1.14 MPa for conditioned. The locations of UTS in terms of strain were shifted to higher values when the composites were conditioned, due to plasticization effect of water mentioned earlier. Also, while 72 h (three days) at 65% RH may not be sufficient to reach the asymptotic value for moisture absorption, fibers

swollen to any extent are expected to lose some of their brittleness. The increase in values for strain at maximum load after conditioning were 27, 82, and 71% for T40, T50, and T60 composites, respectively. This result contradicts the expected increase in plasticization behavior with increase of conditioned resin content. However, the location or strain at UTS is not very consistent as seen from values of T50 after conditioning in Table 14, i.e., $3.6 \pm 1.23\%$. This high SD extends up to 34% away from the mean. Furthermore, the percent increase in strains is an indication of the lower bound of the hybridization effect, i.e., amount of deviation from maximum elongation.¹³⁹ Thus, intuitively, increasing fiber content magnifies the hybridization effect. Regardless of the reason, it should be noted that the location of UTS on the strain axis is not to be mistaken as a ductility measure for these random RS-reinforced hybrid composites. Since within the hybrid region, stronger fibers may carry the load and *spike* the stress response at locations where this situation occurs.

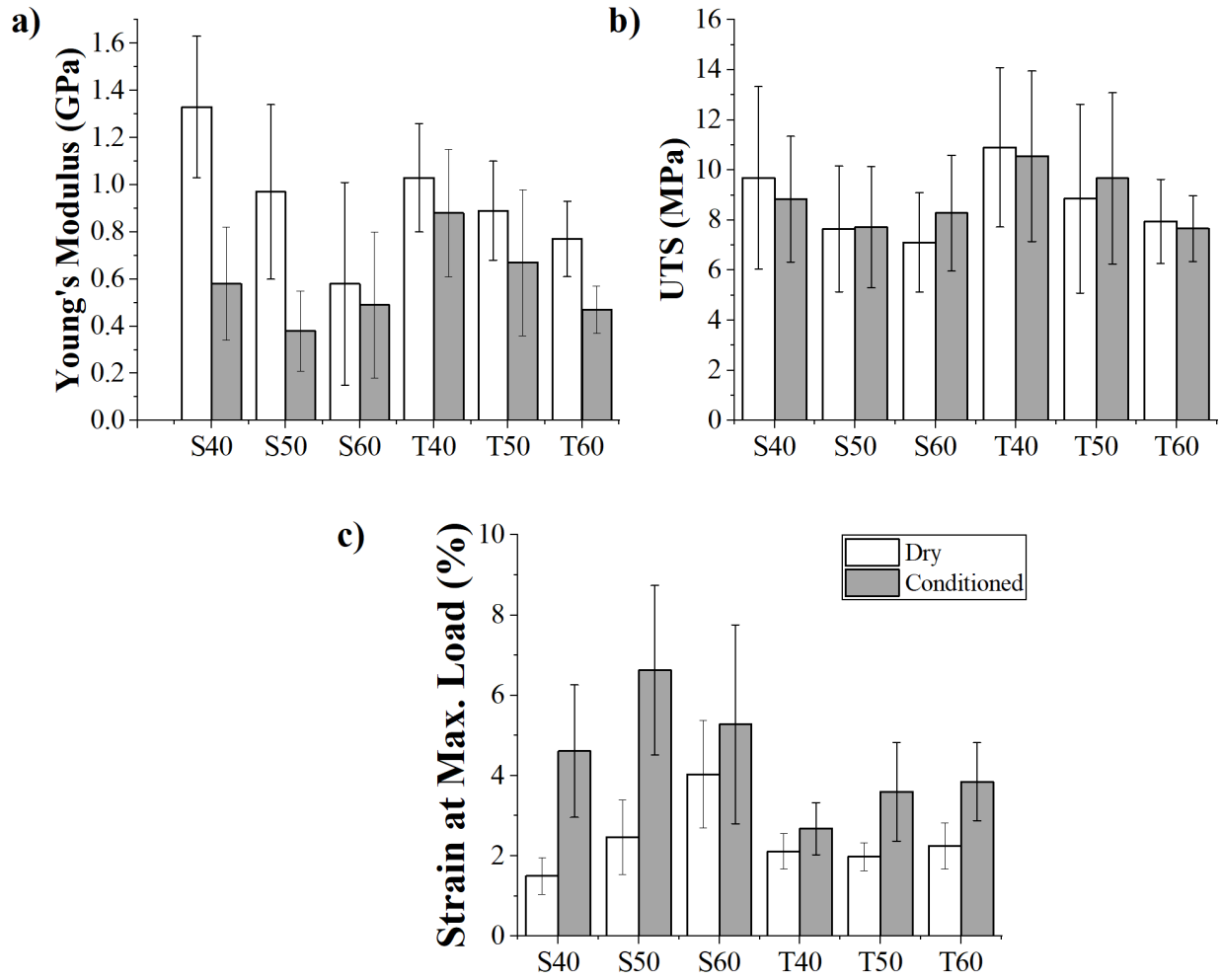


Figure 32. Tensile properties of six different RS/JFa/SPI composites in the warp direction before and after conditioning a) Young's modulus, b) ultimate tensile stress, and c) strain at maximum load.

Table 13. Tensile properties of dry RS/JFa/SPI composites in the warp direction.

Dry Composites	E_y (GPa)	UTS (MPa)	Strain at Max. Load (%)
S40	1.33 ± 0.30	9.69 ± 3.64	1.50 ± 0.46
S50	0.97 ± 0.37	7.65 ± 2.51	2.47 ± 0.93
S60	0.58 ± 0.43	7.11 ± 1.98	4.03 ± 1.34
T40	1.03 ± 0.23	10.91 ± 3.18	2.11 ± 0.44
T50	0.89 ± 0.21	8.86 ± 3.77	1.98 ± 0.35
T60	0.77 ± 0.16	7.95 ± 1.68	2.25 ± 0.57

N= 32–37 specimens for each type of composite.

Table 14. Tensile properties of conditioned RS/JFa/SPI composites in the warp direction.

Conditioned Composites	E_y (GPa)	UTS (MPa)	Strain at Max. Load (%)
S40	0.58 ± 0.24	8.84 ± 2.51	4.61 ± 1.65
S50	0.38 ± 0.17	7.72 ± 2.42	6.63 ± 2.11
S60	0.49 ± 0.31	8.28 ± 2.31	5.28 ± 2.48
T40	0.88 ± 0.27	10.55 ± 3.40	2.68 ± 0.65
T50	0.67 ± 0.31	9.67 ± 3.42	3.60 ± 1.23
T60	0.47 ± 0.10	7.66 ± 1.31	3.85 ± 0.97

N= 31–38 specimens for each type of composite.

Figure 33 visualizes datapoints of E_y , UTS, and strain at UTS for S- and T-type composites, dry and conditioned, in the weft direction. **Table 15** and **Table 16** present the results of the same tests for dry and conditioned composites, respectively. Stiffness and UTS in the weft direction were not only lower than those in the warp direction for all composites, but they also suffered from higher SD. Since the weft direction of the jute fabric supports less load than that of the warp, composites are subsequently expected to have the same characteristic. Furthermore, felting may be responsible for disorienting the jute yarns away from their original aligned geometry. The higher standard deviations can

be seen on Figure 33 for both S-type and T-type composites. However, they are much lower for the T-type composites, as expected. The weft direction also has higher strains at maximum load. As mentioned earlier, the un-tensioned weft yarns acquire significantly increased crimp (ratio of fabric length to yarn length) than warp yarns. This means there is more of weft yarn length to 'straighten' in the elastic region prior to UTS and break. This obviously results in higher strains.

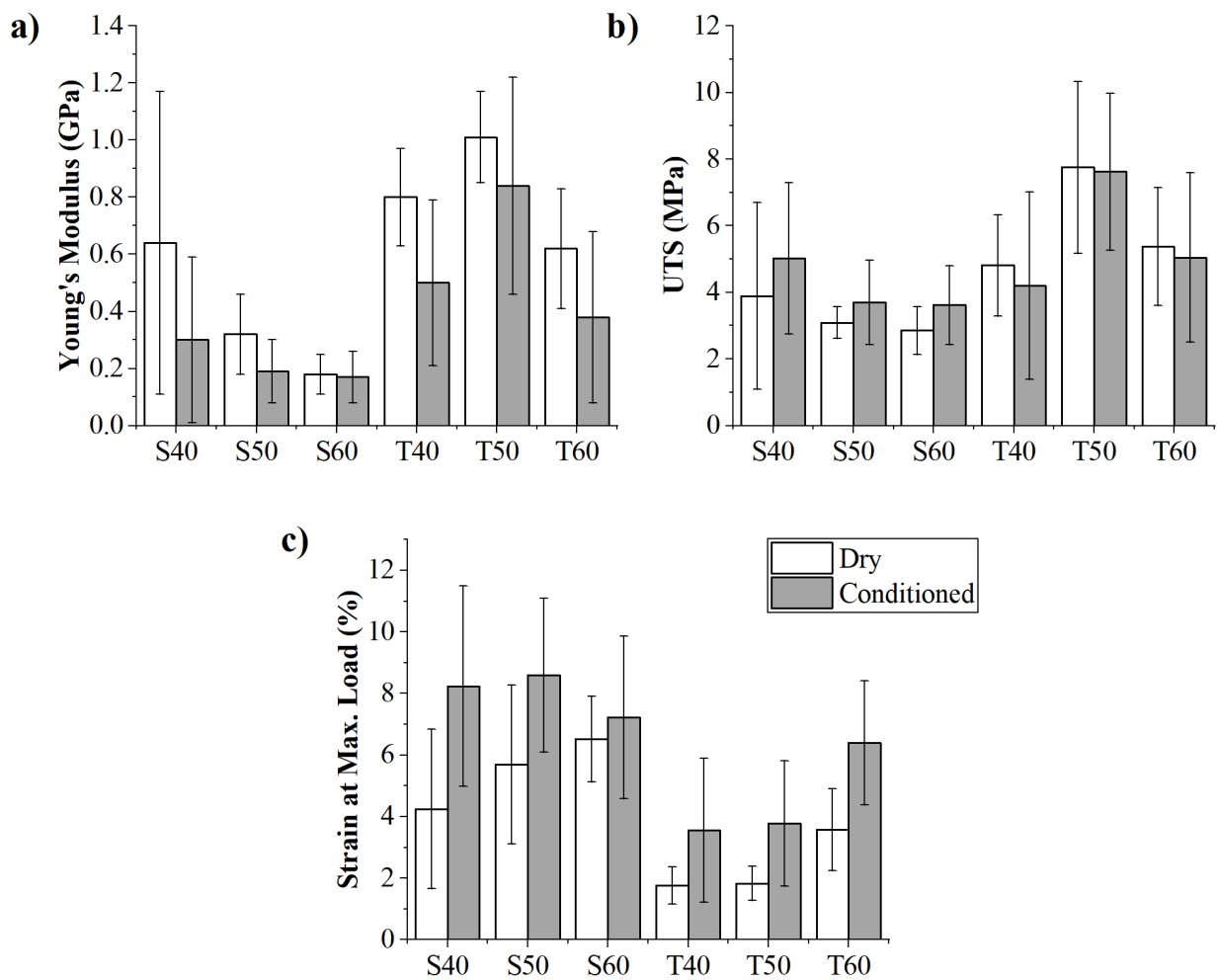


Figure 33. Tensile properties of six different RS/JFa/SPI composites in the weft direction before and after conditioning a) Young's moduli, b) ultimate tensile stress, and c) strain at maximum load.

Table 15. Tensile properties of dry RS/JFa/SPI composites in the weft direction.

Dry Composites	E_y (GPa)	UTS (MPa)	Strain at Max. Load (%)
S40	0.64 ± 0.53	3.89 ± 2.80	4.24 ± 2.59
S50	0.32 ± 0.14	3.09 ± 0.48	5.69 ± 2.58
S60	0.18 ± 0.07	2.85 ± 0.71	6.51 ± 1.39
T40	0.80 ± 0.17	4.81 ± 1.52	1.76 ± 0.60
T50	1.01 ± 0.16	7.75 ± 2.58	1.83 ± 0.55
T60	0.62 ± 0.21	5.38 ± 1.77	3.58 ± 1.33

N= Between 25–33 specimens for each type of composite.

Table 16. Tensile properties of conditioned RS/JFa/SPI composites in the weft direction.

Conditioned Composites	E_y (GPa)	UTS (MPa)	Strain at Max. Load (%)
S40	0.30 ± 0.29	5.02 ± 2.28	8.24 ± 3.25
S50	0.19 ± 0.11	3.70 ± 1.26	8.59 ± 2.50
S60	0.17 ± 0.09	3.62 ± 1.18	7.22 ± 2.64
T40	0.50 ± 0.29	4.20 ± 2.82	3.55 ± 2.34
T50	0.84 ± 0.38	7.62 ± 2.36	3.77 ± 2.04
T60	0.38 ± 0.30	5.04 ± 2.54	6.39 ± 2.02

N= Between 20–42 specimens for each type of composite.

4.3 Flexural properties

Flexural properties at a single point in a composite do not represent the whole composite's flexural response. The reason for this is that fiber-reinforced composites, especially the hybrid ones, are highly anisotropic materials and may exhibit many failure modes.¹³⁹ Also, the failure point may be due to a severe defect overlap at that location.

At the beginning of this research project, a four-point flexural test was employed since it imposes less shear deflection on the flexure area. It also induces a force gradient on the area between the two loading points. Hence, the flexural response that is detected

would be in the area between the four points, as opposed to a single point in the three-point flexural test. However, after conducting many four-point bend tests, the specimen flaw seen in **Figure 34** was observed. Several composite specimens failed to fracture between the two intermediary force points, closer to the edge. The hydrophilic nature of RS/JFa/SPI composites also caused specimens to warp after conditioning. Although warping in conditioned flexural specimens, shown in **Figure 35**, can be barely detected, the warping effect was exaggerated under loads. Thus, causing an imbalanced force distribution as seen in Figure 34.

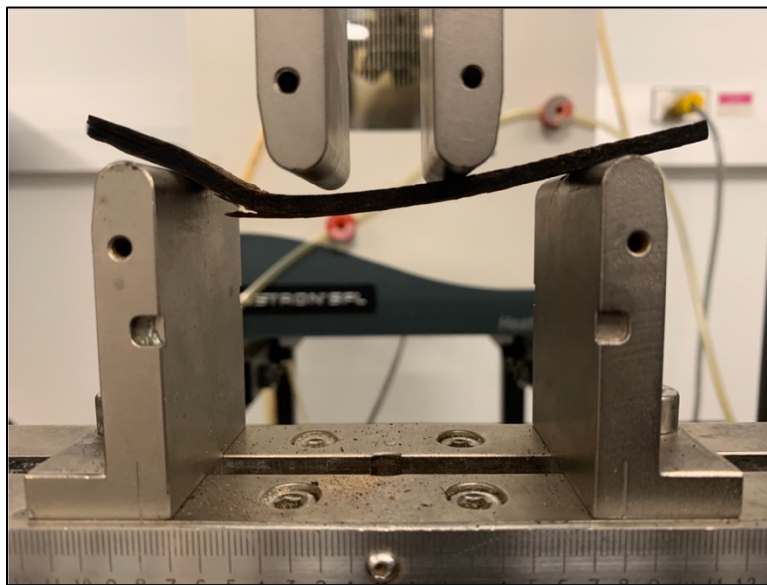


Figure 34. Unsuccessful four-point bend test of RS/JFa/SPI composites.



Figure 35. Side view of a stack of laser-cut RS/JFa/SPI flexural test specimens after conditioning.

The three-point flexural test is at a higher risk of shear stress deflection than the four-point flexural test. These stresses can be minimized by choosing a higher span-to-depth ratio, which was chosen to be between 1:16–1:20. The higher crosshead speed or test rate of 10 mm/min used in these tests can be expected to increase strength and flexural modulus. **Figure 36** shows a T40 composite specimen at flexural break under three-point bend test. It shows the lower face of RS fibers, which are under maximum stress, breaking while some flexibility is seen through the thickness of the specimen in Figure 36a, which is due to the ductile resin and the woven JFa.

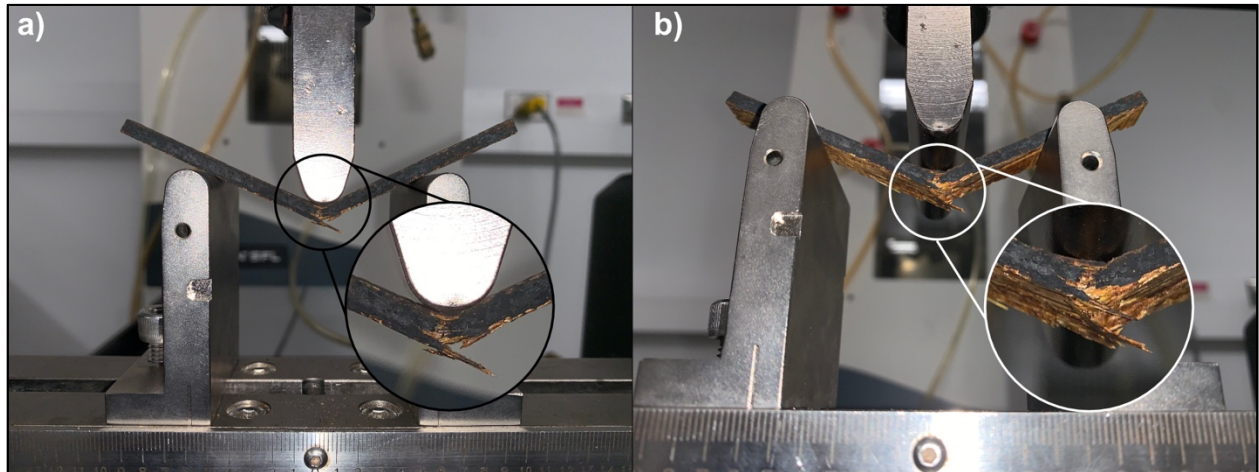


Figure 36. RS/JFa/SPI T40 specimen fracture at the RS face under a three-point bend test, a) front view, b) bottom view.

Figure 37 depicts typical plots obtained from three-point flexural tests. Before conditioning, Figure 37a, T40 and T50 face multiple failure modes illustrated as steps due to the strain gradient through the thickness of the specimen.¹³⁹ Increasing fiber load seems to decrease the number of steps until they reach a minimum at T60 where there are only two distinct failure steps. This may be due to the decrease in thickness of the specimens at higher fiber content (i.e. ~3.58, ~3.23, ~3.10 mm for T40, T50, T60 specimens, respectively), since SPI is considered a bulky resin and fibers can be compressed, particularly the RS. It could also indicate weak fiber/resin interaction due to overloading the resin with fibers. As discussed earlier, resin is insufficient at higher fiber load to surround the fibers effectively. The failure mode is not instant as can be seen and the stress drop is followed by another stress rise. This is a result of the tensile and compressive forces acting simultaneously on the specimen during bending, which were possibly a result of different reinforcement types and layers, and different layers getting loaded. Since these hybrid composites comprised of layered RS (random fibers) and JFa

(woven yarns) reinforcement, the failure mode is expected to change as fracture propagates throughout the depth of the specimen. Plots for T40 and T50 specimens seen in Figure 37a show sharp initial failure modes followed by smoother ones. This sequence agrees with the order of layers carrying the flexural load, RS at the bottom and then alternating with JFa.

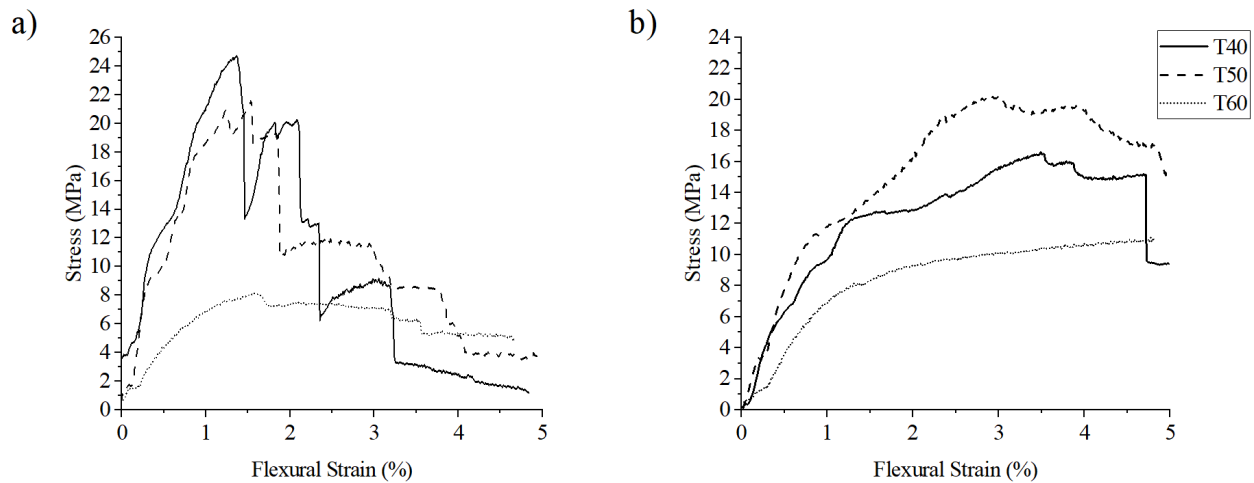


Figure 37. Typical flexural stress-strain plots of RS/JFa/SPI composites obtained from three-point-bend test a) before conditioning and b) after conditioning.

The 5% failure strain cutoff is the ASTM recommendation for reinforced plastics and is meant for specimens that would exhibit flexural rupture before that value. Figure 37b is a clear depiction of the plasticization effect of water. The stepwise failure modes are not found below 5% strain which means that increased resin plasticity has a large effect on how composites would respond to flexural stresses. After conditioning, the lack of sudden drops in stress indicates that the resin is keeping the composite together, enhancing flexibility, and is distributing the load more evenly.

Figure 38 presents the flexural test results side-by-side and the data are summarized in **Table 17** and **Table 18**. Similar to the general tensile property trends, the composites become more compliant and weaker when conditioned, mainly as a result of resin plasticization through absorbed moisture. Also, both E_f and ultimate flexural strength (UFS) decreased with increased fiber load. A trend that supports the earlier argument of exceeding the resin's optimal fiber load capacity, probably around T40 systems. The high anisotropy of these hybrid composites is very clear from the large standard deviations of the flexural properties. The anisotropy and high SD values also suggest that having three layers may not be good enough for real world applications and perhaps, five- or seven-layer composites would perform better. Higher number of layers would also reduce the warping during conditioning. These tests were performed with the RS fibers on the bottom. But in order to design composites with higher flexural moduli, the side with the stiffer fibers (in this case jute fabric) would be placed on the outer side of the composite/panel.^{144,145} There is no significant statistical drop in E_f and UFS for T60 after conditioning. It's higher resistance to water absorption is due to lack of highly hydrophilic SPI resin. As for T40 and T50, their E_f are statistically similar in both dry and conditioned states. The shift of UFS to a higher strain after conditioning is found to be at an increase of 90, 53, and 6% for T40, T50, and T60, respectively.

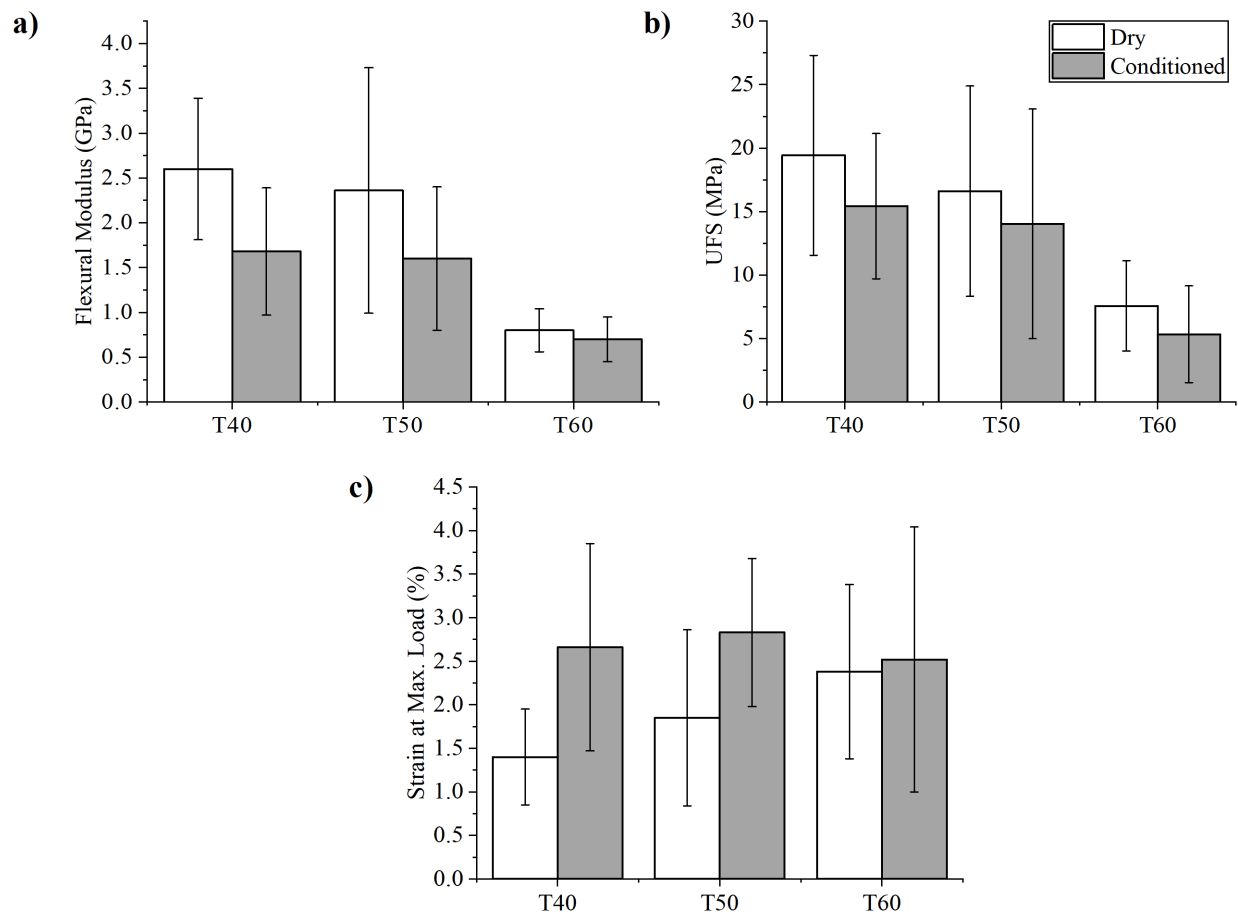


Figure 38. Three-point-bend test results of three different RS/JFa/SPI composites before and after conditioning a) flexural modulus, b) ultimate flexural stress, and c) strain at maximum load.

Table 17. Flexural properties of dry RS/JFa/SPI composites.

Dry Composite	E_f (GPa)	UFS (MPa)	Strain at Max. Load (%)
T40	2.60 ± 0.79	19.43 ± 7.87	1.40 ± 0.55
T50	2.36 ± 1.37	16.61 ± 8.27	1.85 ± 1.01
T60	0.80 ± 0.24	7.57 ± 3.55	2.38 ± 1.00

N= 18–19 specimens for each composite.

Table 18. Flexural properties of conditioned RS/JFa/SPI composites.

Conditioned Composite	E_f (GPa)	UFS (MPa)	Strain at Max. Load (%)
T40	1.68 ± 0.71	15.43 ± 5.72	2.66 ± 1.19
T50	1.60 ± 0.80	14.03 ± 9.04	2.83 ± 0.85
T60	0.70 ± 0.25	5.34 ± 3.81	2.52 ± 1.52

N= 19–21 specimens for each composite.

4.4 Interfacial shear strength (IFSS)

Interactions at the interface between the different phases existing in a composite dictate the composite's overall properties. They most certainly enhance or limit the stress transfer capabilities from broken fibers to intact fibers through the fiber/resin interface depending on the IFSS. This boundary between the resin and fiber exists through:^{99,100}

1. micromechanical interlocking,
2. permanent or transient dipole interactions (e.g. van der Waals or hydrogen bonding),
3. primary bonding (i.e. covalent), or
4. surface energetics (spreading of resin on fiber surfaces).

Unlike common synthetic fibers used in commercial PMCs (such as carbon, glass, aramid, etc.), natural fibers have highly nonuniform morphologies.¹⁴⁶ Therefore, quantifying a system's IFSS through a microbond test is further challenged; especially that rougher segments of fiber surfaces would enhance the mechanical interlocking with the resin bead.

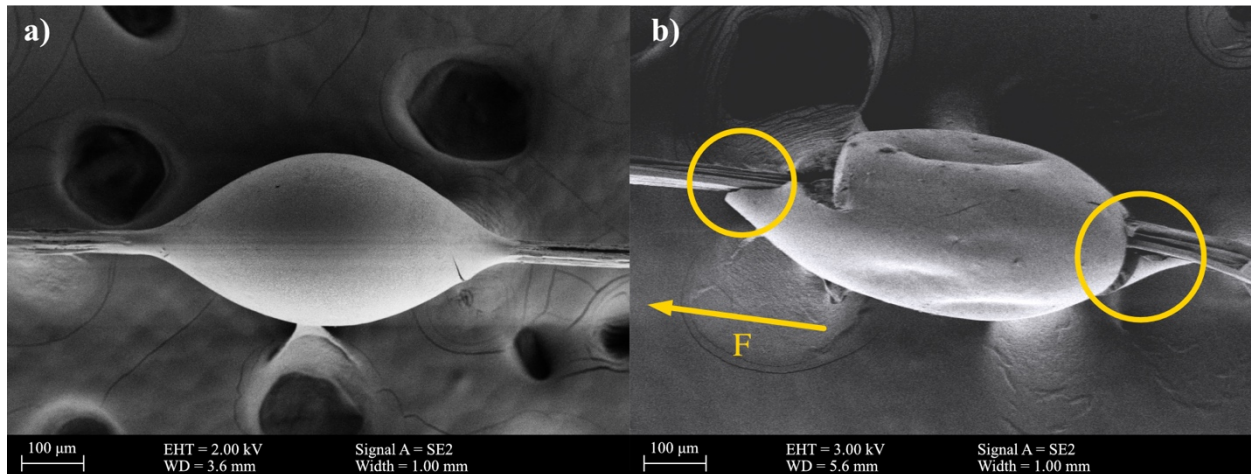


Figure 39. SEM micrographs of a typical cured SPI resin droplet on jute fiber a) before and b) after microbond test.

Figure 39 shows SEM images of a typical fully cured SPI microbead surrounding a jute fiber before and after pullout. The microbead successfully surrounds the fiber as seen in Figure 39a. The hydrophilic compatibility between the fiber and the resin is clear from where the microbead spreads and gradually merges with the fiber. After pullout, complete debonding was observed from the spatial gaps between the bead and fiber that are circled in Figure 39b. There was a certain limitation that this experiment encountered, particularly for jute fibers. The jute fibers were taken from the same jute fabric used to reinforce the composites. Since these staple jute fibers were twisted into yarns during manufacturing, the process of extracting a single strand included delicately untwisting the yarn and choosing longer lengths that could be used for the microbead tests. Even with that practice, most of the jute strands experienced premature failure and broke during the IFSS test. That is because what seemed to be a single strand could in fact be two or more cohesive fibers that detangle with minimal stress. Another possible reason for jute fiber failure before complete debonding may be the imperfect untwisting of the

strand. This test was performed under the assumption of perfect geometries shown earlier in Figure 17, which results in a pure shear stress state. However, with the slightest deviation from a perfect geometry, such as a minor twist or a deviated force vector, the stress state would become more complex and lose its symmetry. Therefore, the induced stress would shift from a pure shear mode acting at the fiber/resin interface area, into a complex case containing normal, hoop, and/or shear stresses. Lastly, the microbond test itself is a modification of a conventional fiber pullout test (a single fiber emerged in resin at one end) to accommodate for shorter fibers' inability to exceed the "critical embedment length".¹⁴⁷ It seems from our experiments that the microbead dimensions have not met the critical length values. The minimum fiber length required to transfer the load for discontinuous fiber reinforcement is known as the critical length (l_c) and is found according to Equation 4.15.^{36,148}

$$l_c = \frac{\sigma_f d}{2 \tau_{max}} \quad (4.15)$$

where σ_f is fiber's fracture strength and d is the diameter of the fiber. For JF/SPI (and based on an averaged $\sigma_f = \sim 583 \text{ MPa}$ ¹⁴⁹), l_c equals 4.4 mm. This length is much higher than the fiber/resin contact length in the JF microbead test ($0.77 \pm 0.12 \text{ mm}$). For those reasons, jute specimens that broke before an extension equal to 90% of fiber/bead contact length were eliminated. Out of the 28 jute/SPI IFSS specimens, only 13 passed the set criterion.

Table 19. Microbond test results of SPI pH 12.5 bead on jute or RS fibers.

Fiber	Contact Area (mm ²)	Max. Force (N)	IFSS (MPa)
Jute fiber	0.16 ± 0.06	0.61 ± 0.17	4.25 ± 1.78
Rice straw	1.99 ± 0.97	4.53 ± 1.98	2.68 ± 1.30

N = 13 for jute and 20 for RS.

Similar criteria were set for RS/SPI IFSS testing as well. However, the failure rate encountered for RS was much less than jute fibers. Out of the 23 specimens, 20 specimens were successful. The higher success rate is mainly due to RS being single continuous fiber specimens as opposed to the mechanically twisted staple jute fibers studied in this research.

Figure 40 illustrates the typical load-displacement curves of the IFSS tests for both RS/SPI and jute/SPI specimens. The steep inclination observed for the jute/SPI specimens indicates a higher surface roughness than RS/SPI. As for RS, a linear region is seen up until approximately half the maximum force. Followed by a low sloped incline in load with continued fiber pullout. This behavior resembles overcoming the rougher or highly bonded fiber/resin segments, followed by a variant surface morphology until successful fiber pullout (note: resin beads had an average length of 2.45 ± 0.55 mm for RS/SPI specimens). Jute load vs. displacement plot is that of a typical shear debonding, while the low slope incline observed for RS resembles droplet slippage as established by *Miller et al. (1987)*.¹⁴⁷

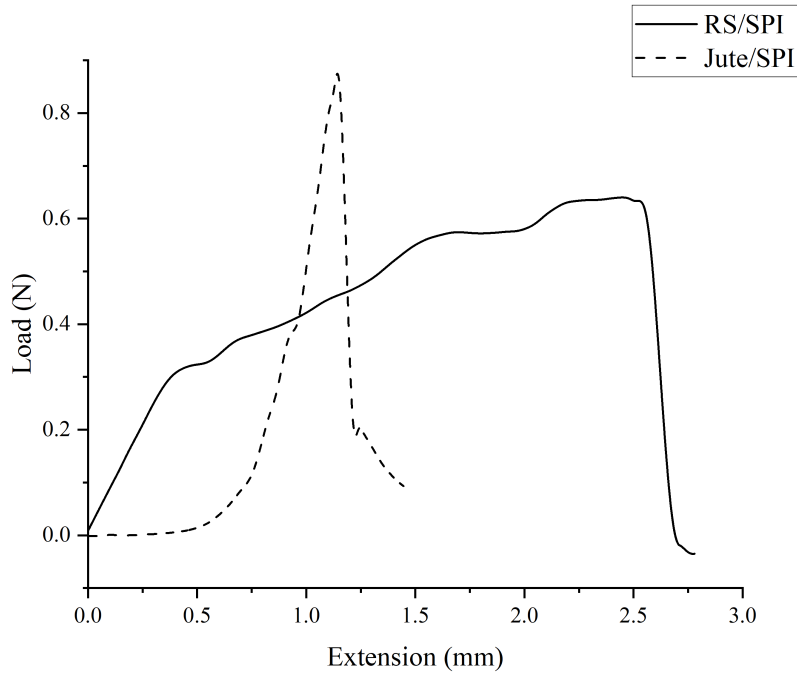


Figure 40. Typical load vs displacement curves of microbond tests for RS/SPI and JF/SPI.

Table 19 summarizes the microbond test results for both RS and jute fibers. The results show a slightly higher IFSS value for jute over RS. This can be a result of the relatively rougher morphology of JF compared to RS as can be seen in the SEM micrographs of the fibers in **Figure 41**. Also, due to the fact that JF is a bundle of fibers or fibrils which increases the surface area available for the resin to bond to. Although the two IFSS values can be statistically distinguishable ($P = 0.012$), IFSS tests have many limitations that would prevent them from quantitatively identifying the IFSS values. These limitations include the difficulty of measuring the fiber and resin bead dimensions, as well as the varying stress matrix components and responsive failure modes.¹⁰⁰

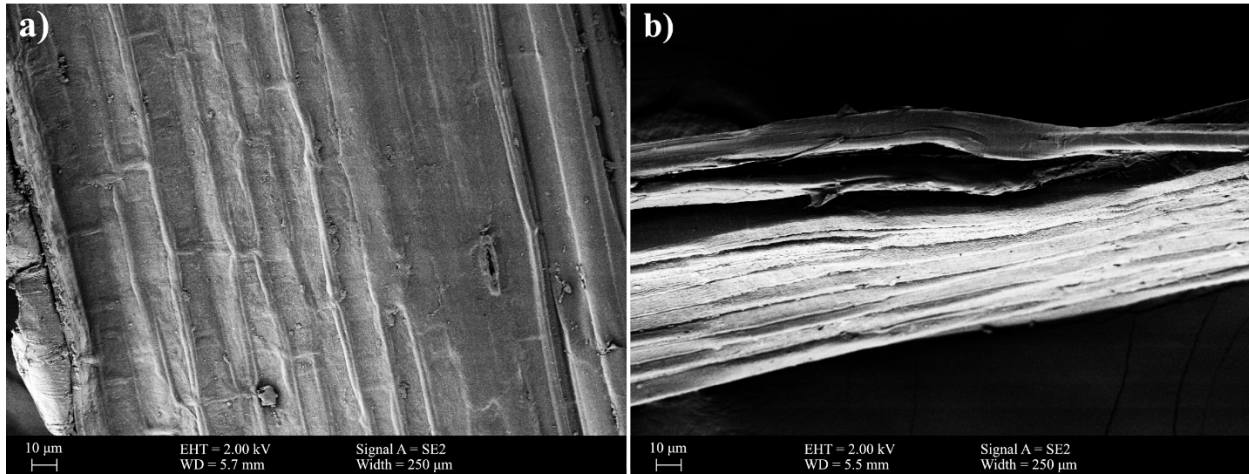


Figure 41. SEM micrographs showing surfaces of a) rice straw and b) jute fiber.

The IFSS values obtained are very low compared to the ones found in the literature for soy-based resins and cellulosic fibers. It is difficult to draw conclusions from results of different resins and different fibers. Nonetheless, IFSS values of noncrosslinked soy proteins with ramie fibers obtained from similar experiments^{36,100} were equal to 22.8 and 29.8 MPa. Another experiment reported by *Huang and Netravali (2007)*¹⁵⁰ reported self-crosslinked soy protein concentrate resins and flax fibers IFSS to be 11.9 MPa. It is worth mentioning that these studies used glycerol as a plasticizer, which has around half the molar mass of D-sorbitol used in the present study. In general, increasing plasticization negatively affects IFSS as the resin becomes much softer. Therefore, with no exclusion to other experimental parameters and limitations, low IFSS exhibited by the fibers and resin in this study may also be attributed to the high plasticization effect water and D-sorbitol had on the SPI microbeads.

The deduction that most concerns this study is that both fibers' IFSS values were lower than the resin's UTS. It can be expected that this would result in composites with higher toughness, but lower strength and stiffness. In the case of resin UTS highly

exceeding IFSS (in this case by a factor of 69% for jute/SPI and 168% for RS/SPI), the failure is expected to always occur at the interface, particularly at RS/SPI interface. Furthermore, the interface absorbs a considerable amount of energy given the hybrid nature of RS/JFa/SPI composites which contains a significant amount of interface. Thus, the hybrid region circled in Figure 29 would extend further due to this low IFSS characteristic. The UTS of the T-type composites in the warp direction exceeds IFSS of JF/SPI which means that even after fiber pullout occurs, the jute yarns (primarily) and rice straws are able to take load, though not for too long. Looking closely at Figure 31b, T40 (composites with the highest resin content of 60 wt%) keep taking load in an almost linear fashion after surpassing IFSS values until it breaks catastrophically after reaching UTS. This suggests that the higher resin volume was able to transfer the load from broken to intact fibers more efficiently. Additionally, the stepwise failure trend in T40 composites suggests the existence of resin/fiber interface beyond UTS, and each step represents a yarn breakage with a small ductile plateauing region, evidently resembling resin extension. The stress-strain plots of composites with higher fiber load (T50 and T60) begin arching around the IFSS value and fail in a more brittle fashion. As for the more ductile weft direction, the stress increases in multiple steps. These steps may indicate straightening of yarns in the weft, which break before they could align as good as the warp. The lowest resin content composite, T60, shows the lowest stiffness and exhibits higher elongation to reach UTS. This behavior possibly indicates the dominance of fiber-fiber interaction which keeps the fiber bundles together beyond IFSS marks.

Figure 42 presents JF/SPI and RS/SPI IFSS values plotted against contact area. IFSS should ideally be constant with varying contact area, since the shear stresses acting on

the fibers would scale with the contact area accordingly. However, that is not the case here. In fact, there seems to be a clear inverse correlation between IFSS and contact area. Two main reasons may be cited for this. First, the experimental fixture used for the tests may not be as ideal as explained previously. Second, smaller beads with lower contact area would have a less destructive effect on the experiment. Meaning, their lower mass, which acts as a stress under gravity, would cause less damage to the non-ideal stress matrix.

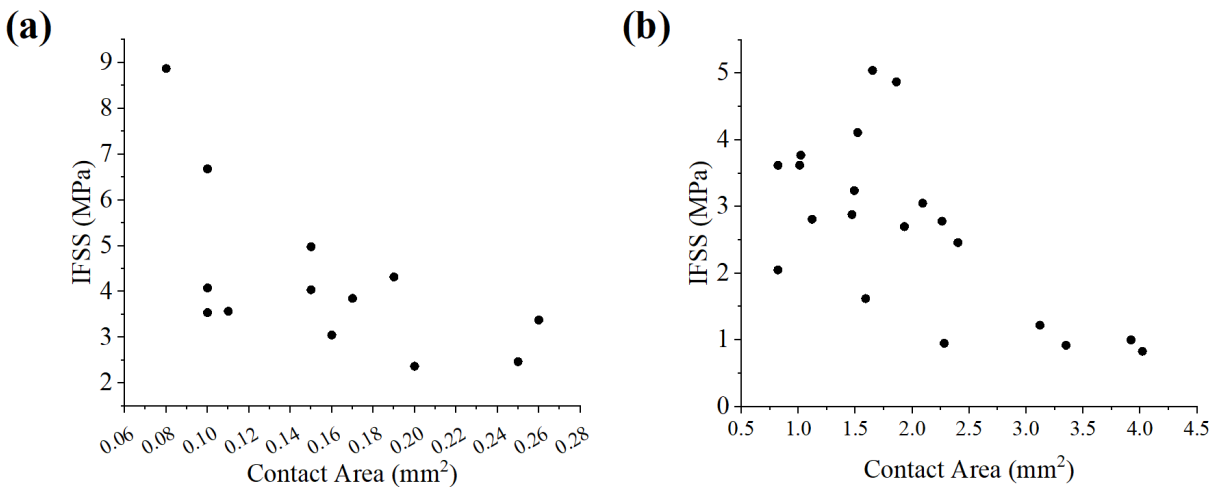


Figure 42. Interfacial shear strength with respect to contact area of a) JF/SPI and b) RS/SPI as obtained from microbond test.

4.5 Dynamic mechanical analysis of composites

The mechanical properties of hybrid PMCs should not be reduced to the static tensile and flexural tests. Most polymer-based resins and plant fibers have both viscous and elastic responses to deformation. Viscoelastic materials are known to exhibit viscoelastic characteristic in a certain temperature range.¹⁵¹ Hence, under an applied

frequency and a temperature ramp-up, characteristic dynamic mechanical properties may be determined. Of particular interest are the loss modulus which characterizes the viscous behavior, and storage modulus which characterizes the elastic characteristic. Finally, the ratio of loss-to-storage moduli known as $\text{Tan } \delta$, which is also an indication of damping in a material. $\text{Tan } \delta$ also provides the glass transition temperature (T_g) of the composite (more specifically the resin).

The plots obtained from DMA for the T-type composites are shown in **Figure 43** and the data are presented in **Table 20**. Loss moduli of the composites have maximums at similar temperatures and their values are within the same range with insignificant statistical differences. The highly randomized RS fiber orientations and lengths may have affected the energy dissipation in the composites. Another statistically insignificant difference was found in the mean storage moduli of the composites. While increased reinforcement is expected to increase the storage modulus at onset, it did not for the tested specimens. This may be attributed to the plasticization effect that water had on the composites which increases the testing variations. In fact, moisture effect is quite drastic in these composites. Since T_g for dry soy protein ranges from 145–176°C,^{152,153} and the T_g values found from these DMA tests are from 80–88°C (from loss modulus peaks) or 100–115.9°C (from $\text{Tan } \delta$). Also, it might confirm the exceedance of optimal fiber load that the resin could adhere, probably by the 40 wt% fiber content. As seen in the elastic moduli along conditioned composites tested in warp direction (Table 14), the values fall within a close range and their means decrease with increased fiber content (0.88 ± 0.27 , 0.67 ± 0.31 , and 0.47 ± 0.10 GPa for T40, T50, and T60 composites, respectively). T40 showed the highest damping and the highest T_g from the $\text{Tan } \delta$ curve. Which is not the general case when the

T_g is expected to increase with increased fiber load.¹⁵⁴ The low and broad $\text{Tan } \delta$ peak height with increased fiber load could mean that the SPI chain mobility is restricted with higher fiber load.^{155,156} The high damping that the composites exhibited further magnifies the difference between Young's moduli and the frequency-dependent storage moduli.

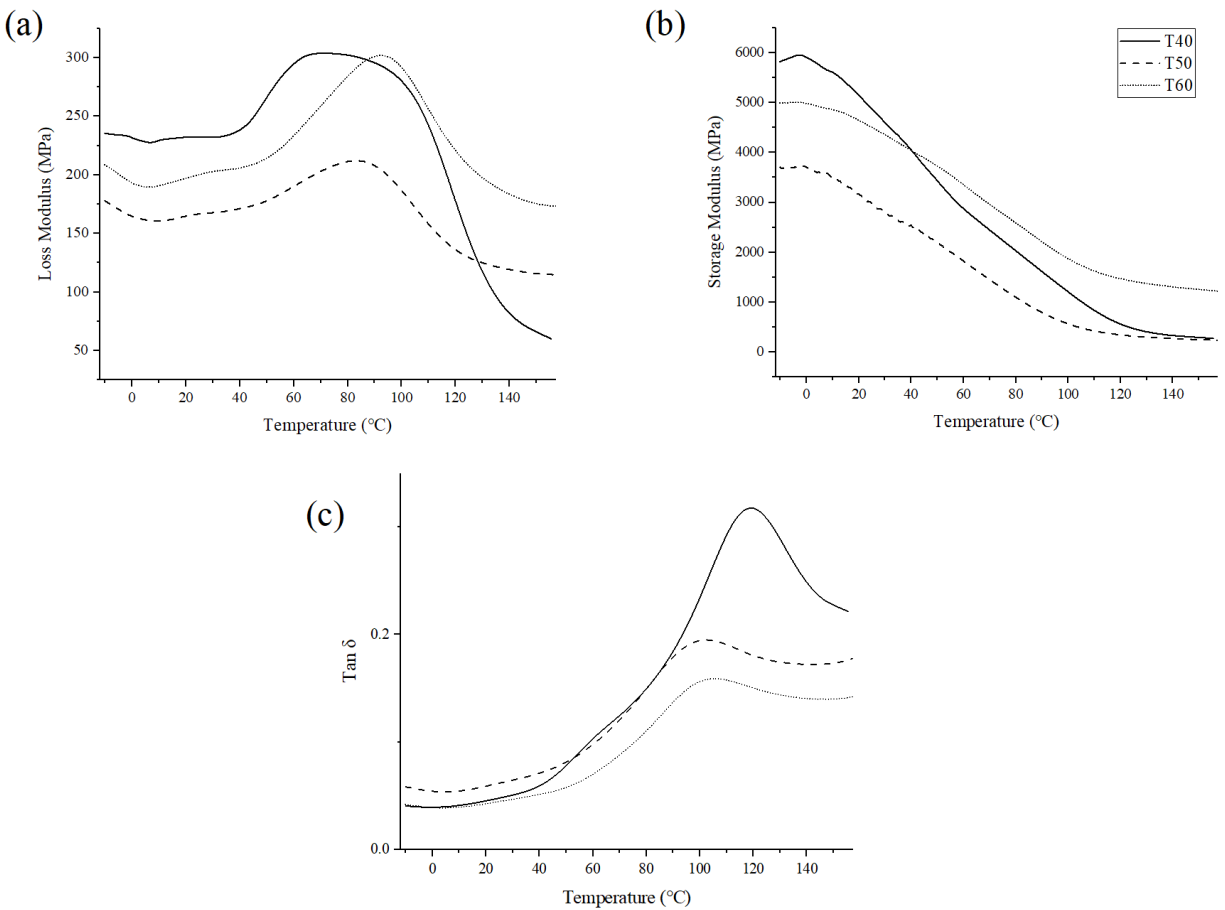


Figure 43. DMA plots of T-type composites, showing a) loss modulus, b) storage modulus, and c) $\text{Tan } \delta$ plots with respect to temperature.

Table 20. Dynamic mechanical analysis test results of T-type composites.

Composite	Loss Modulus		Storage Modulus		Tan δ	
	Max. Value (MPa)	Temp. at Max. Value (°C)	Onset Temp. (°C)	Value at Onset Temp. (MPa)	Max. Value	Temp. at Max. Value (°C)
T40	306.6 ± 33.9	81.9 ± 1.8	9.2 ± 1.5	5477 ± 648	0.318 ± 0.004	115.9 ± 4.8
T50	252.0 ± 66.9	80.0 ± 4.1	8.9 ± 1.3	4134 ± 1546	0.2455 ± 0.042	103.2 ± 1.6
T60	275.7 ± 59.4	88.0 ± 8.8	6.2 ± 3.7	4566 ± 808	0.1513 ± 0.015	100 ± 8.1

N= 3–4 specimens of each composite.

4.6 Fracture analysis by SEM

SPI resins are known to be brittle. The crosslinked three-dimensional proteinic network forms a rigid structure that enhances intermolecular forces, thus limiting protein chain mobility.⁴³ Fracture topography of SPI12-140 is shown in the SEM micrographs in **Figure 44**. The fractographic patterns exemplify a ductile rupture, indicating successful D-sorbitol plasticization. The *wave-like* planes (seen in Figure 44b) which are sheared at an angle, indicate a plastic deformation prior to rupture.

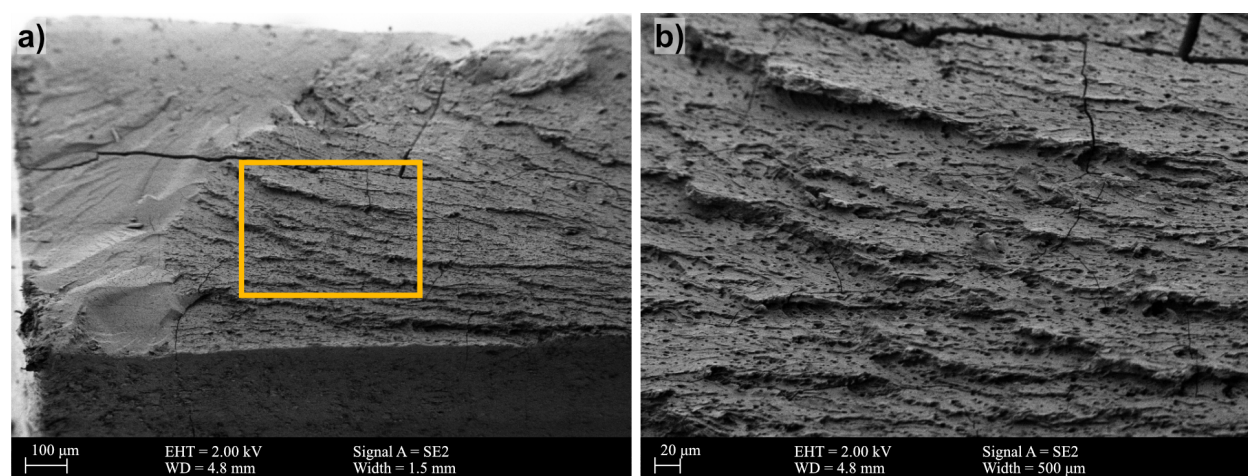


Figure 44. SEM micrographs for fracture surfaces of SPI12-140 resin taken from a 30° tilt angle where a) image taken at 1.5 mm width and b) magnified image of the area indicated with a yellow rectangle on (a).

All the RS/JFa/SPI composites exhibited a brittle fracture mode. Because, as mentioned earlier all components of the green composites, SPI resins, RS, and JFa fracture in a brittle fashion. **Figure 45** shows SEM micrographs of fracture surfaces of T-type composites. Most fracture surfaces seen in T40 specimens follow the patterns shown in Figure 45a and Figure 45b. The fibers are very close to the resin's fracture surfaces. This indicates either a good fiber/resin bonding or the existence of sufficient amounts of resins surrounding the fibers, or both. Given the weak IFSS between SPI and the two fibers, and the fact that the SEM micrographs were taken after fracture; the more probable explanation is that sufficient amounts of resin was present around the fibers. The pulled-out single jute fibers seen in Figure 45b are also covered with the resin, indicating successful resin impregnation into the depths of the composite structure.

As the fiber load increases, the fibers are pulled out further from the resin's fracture axis. For instance, T50 specimens captured in Figure 45c and Figure 45d show grouped fiber bundles that were pulled out altogether from the resin. The "X" marks in Figure 45d point out the edges of the fractured SPI resin. They are far from the fracture axis of the fibers. This shows a possibility of consecutive fracture modes. First, the fiber/resin debonding occurs which can drastically increase the stress on the resins leading them to break. Then fibers (or fiber bundles that have enough resin in between them) are pulled out and share the load to break. A similar but more exaggerated behavior is observed with the T60 specimens in Figure 45e and Figure 45f. Fibers look highly disoriented and there is no obvious fracture axis for both fibers and resin. In this case, the resin content clearly failed to incorporate the extremely high fiber volume present, causing fibers to debond, delaminate, and lose organization.

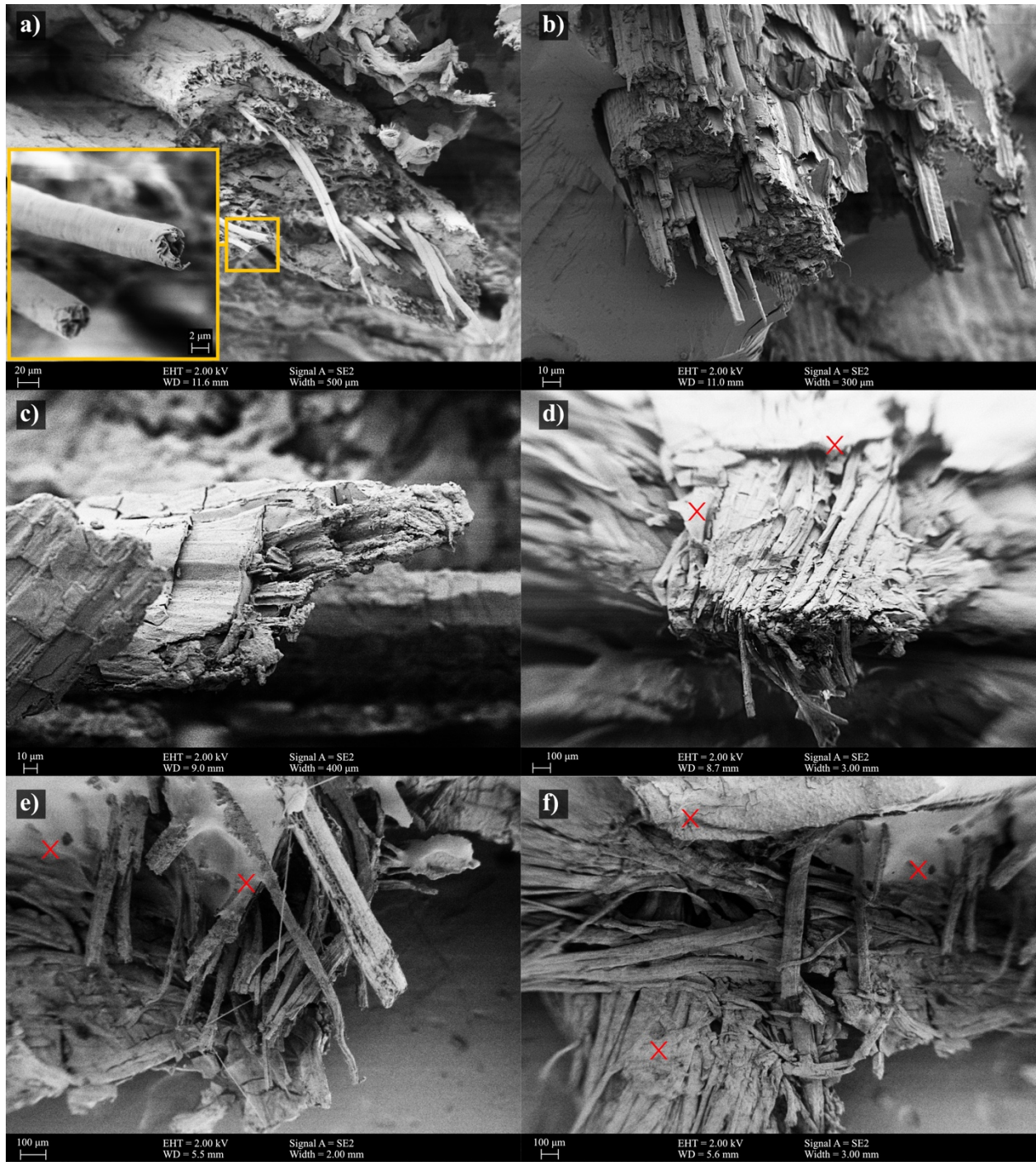


Figure 45. SEM micrographs showing fracture surfaces of RS/JFa/SPI composites for a) and b) T40; c) and d) T50; and e) and f) T60. Note: the red X marks denote SPI resin sites.

4.7 Thermal characterization

4.7.1 DSC of SPI resins

Representative DSC thermograms obtained for the three resins are shown in **Figure 46**. From these thermograms, the transition temperatures (T_1 and T_2) and enthalpies of melting of the three resins were extrapolated and are presented in **Table 21**. The initial endothermic peaks (T_1) represent the denaturing temperatures of 7S and 11S. In their native state (without pre-denaturing), 7S and 11S are reported to have T_1 transitions at 73.8–75 and 88.5–91°C respectively.^{32,55,157} These endothermic peaks were found to shift towards 149.2, 167.0, and 161.3°C for SPI12-120, SPI12-140, and SPI9 resins, respectively, which are much higher than their thermally-induced denaturing temperatures in their native form. That increase in T_1 is attributed primarily to the GA crosslinking of the resin as well as alkali denaturing prior to crosslinking.^{32,158} This suggests a change in protein conformation, in addition to mobility restriction through GA crosslinking resulting in enhanced thermal stability.

SPI12-120 showed the lowest onset of the second endothermic peaks, T_2 . At the same pH level, increasing the hot-press curing temperature to 140°C resulted in a significant increase in T_2 (from 167 to 245.4°C), which indicates enhanced crosslinking at higher pressing temperatures. It is intuitive that curing at higher temperatures would allow for a higher extent of Maillard reactions to occur. This would, in turn, increase crosslinking, chain rigidity, and hence the degradation point of the resin. The thermal stabilities of SPI12-140 and SPI9 are seen to be quite similar, indicating that the extreme alkali denaturing of SPI12-140 was compensated by the higher thermal curing conditions.

Furthermore, SPI12-120 has the highest melting enthalpy, while SPI12-140 and SPI9 encountered lower yet similar enthalpies. This is directly a consequence of crosslinking, which results in decreased crystallinity due to the formation of the three-dimensional proteinic networks, incapable of forming crystals.¹⁵⁹

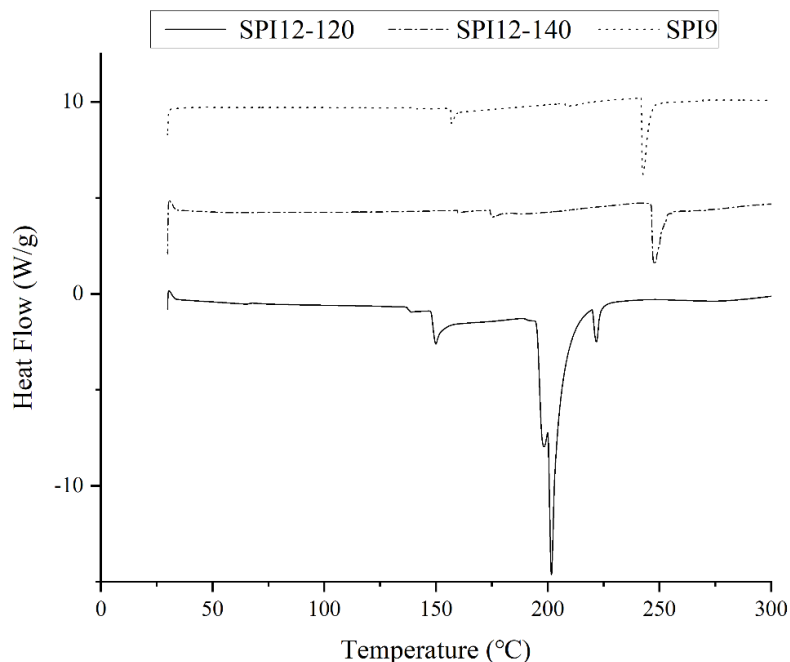


Figure 46. DSC thermograms of three SPI resins prepared at different chemical and/or thermal conditions.

Table 21. Onset temperatures of transitions (T_1 and T_2) and enthalpies of hot-pressed SPI resins.

Resin	T_1 (°C)	T_2 (°C)	Melting Enthalpy (J/g)
SPI12-120	149.2 ± 0.8	194.4 ± 1.7	203.7 ± 15.6
SPI12-140	167.0 ± 7.8	245.4 ± 11.9	55.9 ± 9.9
SPI9	161.3 ± 2.1	246.3 ± 15.2	58.9 ± 3.3

$N=3-4$.

The microbeads produced for the IFSS experiment, as explained earlier, could not be pressed so as to avoid crushing them. Therefore, it was important to match the crosslinking and thermal stabilities of the beads with those of hot-pressed resins. Thus, DSC was used to find T_2 of thermally cured resin droplets and the results are presented in **Table 22** and

Table 23 for SPI pH 12.5 and 9.5 resins, respectively. The SPI pH 12.5 droplets were cured at four different temperatures. It was found that curing microbeads under 110°C for 30 min resulted in a T_2 which was intermediary to that of SPI12-120 and SPI12-140. Furthermore, from

Table 23, we can see that the same curing conditions could be used to represent the hot-pressed SPI9 resin.

Table 22. Onset of melting temperatures of thermally cured SPI pH 12.5 resins.

Curing Temperature (°C)	T_2 (°C)
100	196.5
110	214.5
120	246.3
140	255.9

Table 23. Onset of melting temperatures of thermally cured SPI9 resins.

Curing Temperature (°C)	T_2 (°C)
110	249.5
120	274.9

4.7.2 DSC of composites

DSC thermograms for the RS/JFa/SPI composites are shown in **Figure 47** and the extrapolated T_1 , T_2 , and melting enthalpies are presented in **Table 24**. The three fiber loads have initial protein denaturing peaks within ranges similar to those found in SPI12-140 (Table 21). The increase in the cellulosic content within a composite may affect the degree of crystallinity of a resin by restricting molecular mobility. Although the mean values for T_2 found in Table 24 show an increase in value with increased fiber load, their SD values overlap slightly above T_2 of SPI12-140 ($245.4 \pm 11.9^\circ\text{C}$). This suggests that the fiber reinforcement may have had a minimal to no effect on the crystallinity of the resin.¹⁵ This conclusion is also supported by the minor decrease in enthalpies of melting compared to non-reinforced SPI12-140 resins; indicating a possible slight increase in crystallinity with the presence of lignocellulosic reinforcement.

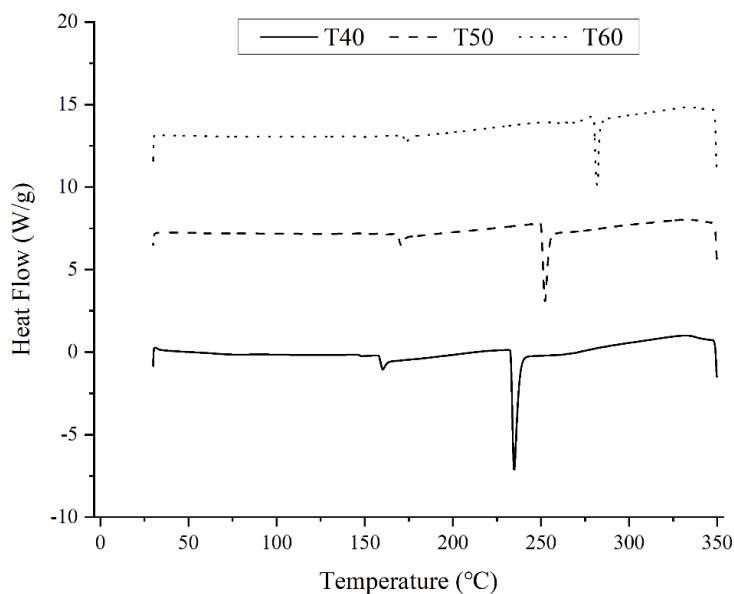


Figure 47. DSC thermographs of RS/JFa/SPI composites with three different fiber loads (40, 50, and 60 wt%).

Table 24. Onset temperature of degradation and enthalpies of RS/JFa/SPI composites.

Composite	T ₁ (°C)	T ₂ (°C)	Melting Enthalpy (J/g)
T40	164.0 ± 4.6	245.3 ± 10.3	45.4 ± 15.6
T50	170.6 ± 5.8	256.2 ± 17.4	49.0 ± 5.1
T60	167.4 ± 4.8	270.1 ± 24.5	52.1 ± 8.9

N=3-4.

4.7.3 TGA of RS, JF, and DPT fibers

The ratios at which plant fiber constituents exist in a fiber influence the thermogravimetric characteristics of a fiber. The three main components arranged from highest to lowest decomposition rates are: hemicellulose, cellulose, and lignin.^{160,161} Hemicelluloses are amorphous, randomly structured, and highly branched, hence, show relative ease to degrade. Cellulose is mostly crystalline, has no branches (i.e., linear), therefore, its onset of degradation temperature (T_d) and maximum weight loss rate are expected to occur at higher temperatures. Lignin's high stability to degradation is mainly due to the abundance of aromatic rings and three-dimensional crosslinked networks.¹³³ Yang *et al.* (2007)¹⁶⁰ characterized the pyrolysis of hemicellulose, cellulose, and lignin. They found that the solid residue of hemicellulose left at 900°C was equivalent to 20 wt%, while cellulose was ~6.5 wt% at 400°C and almost fully pyrolyzed beyond that temperature, and lignin left the highest residue of ~45.7 wt% at 900°C. In addition, the temperatures at which maximum weight loss rates occurred for hemicellulose and cellulose were 268 and 355°C, respectively.

The weight loss percent and the derivative weight loss (%/°C) plots as a function of temperature for RS, JF, and DPT fibers are shown in **Figure 48**. The onsets of degradation

(T_d) and maximum derivative weight loss are presented in **Table 25**. From T_d values found in Table 25, JF shows a distinctly higher degradation onset temperature while RS and DPT fall within the same range. This indicates that JF has the highest cellulose content, while RS and DPT have higher hemicellulose, which agrees with the ratios presented earlier in Table 1. JF shows a sharp $1.14\%/^{\circ}\text{C}$ peak derivative weight loss at 351.8°C that is very close to the cellulose peak location. While for RS, the rate of weight loss peaks were intermediary to those of hemicellulose and cellulose mentioned previously ($0.68\%/^{\circ}\text{C}$ at 312.2°C). As for DPT fibers, there seem to be two distinct peaks, one at 275.1°C and another at 338.8°C , implying a clear separation between hemicellulose and cellulose phases of the specimen. This two-step decomposition is typical for leaf-type fibers such as sisal, as opposed to bast fibers such as jute.²⁸ Table 1 shows that DPT fiber has the highest lignin content of the three fibers, followed by RS which is overlapped by the upper bound of lignin content of JF.^{67,102-106} But from the data for char content at 600°C (22.7, 7.6, and 23% for RS, JF, and DPT, respectively) it can be concluded that the RS and DPT specimens characterized have very similar hemicellulose and lignin contents that largely exceed those found in JF.

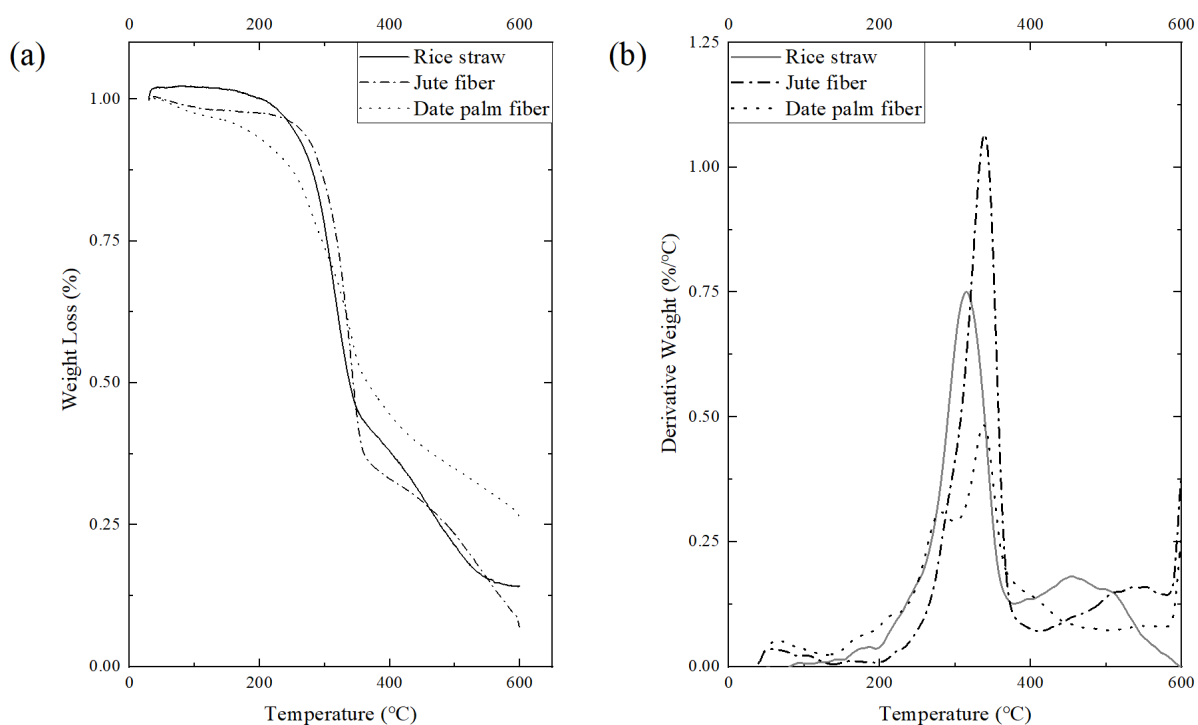


Figure 48. TGA thermograms of rice straw, jute, and date palm tree fibers, showing a) weight loss and b) derivative weight loss with respect to temperature.

Table 25. Onset temperatures of degradation (T_d) and peak derivative weight losses of RS, JF, and DPT.

Sample	T_d onset		Max. Deriv. Weight Loss	
	T (°C)	Weight Loss (%)	T (°C)	Deriv. Weight Loss (%/°C)
RS	249.7 ± 6.3	9.0 ± 3.5	312.2 ± 11.1	0.68 ± 0.12
JF	273.3 ± 3.6	13.2 ± 5.8	351.8 ± 14.5	1.14 ± 0.01
DPT	246.3 ± 1.8	13.6 ± 1.4	338.8 ± 0.2	0.51 ± 0.02

$N=2$.

4.7.4 TGA of resins

Figure 49 and Table 26 present TGA thermograms of SPI resins and certain values extrapolated from the thermograms, i.e., the initial derivative weight loss peak and onsets

of transitions (T_i and T_{ii}). SPI12-120 witnessed its first weight loss peak at a lower temperature (162.4°C) than the other resins (181.2 and 200.3°C for SPI12-140 and SPI9, respectively). This could be an indication of lower crosslinking density and/or higher moisture content in the specimen, since at the initial peak most of the weight loss is evaporated water. Looking at the weight losses at the initial peak, SPI12-120 showed the highest weight loss of 11.6%; although its peak occurred at the lowest temperature. That initial peak was not clear on SPI9 thermograms. The pH 12.5 resins showed almost identical T_{ii} at ~241°C which are lower than those for pH 9.5 resins' T_d (~260.5°C). The char content of SPI12-120, SPI12-140, and SPI9 resins were very similar (24, 27.4, and 26.2%, respectively), with SPI12-120 resin having the least amount of residue at 600°C.

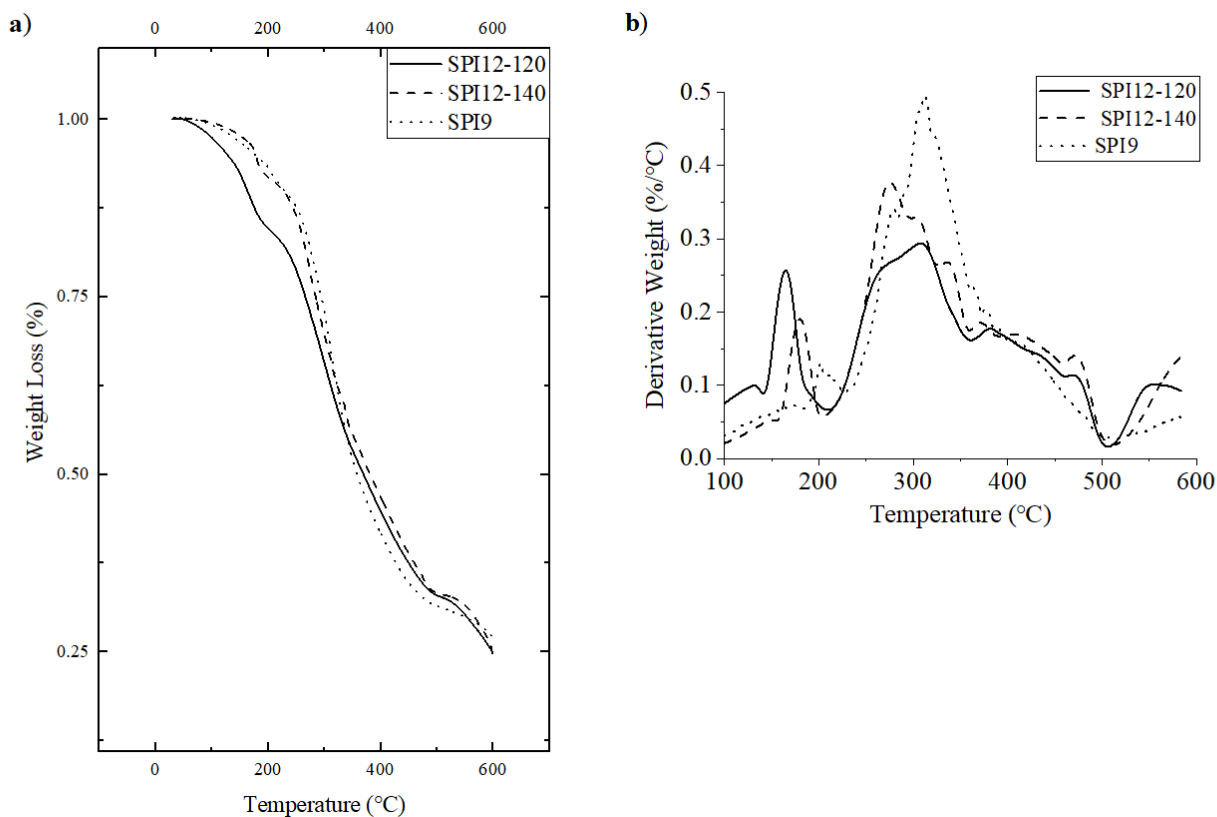


Figure 49. TGA thermograms of the three hot pressed SPI resins, showing a) weight loss plot and b) derivative weight loss plot with respect to temperature.

Table 26. TGA initial derivative weight loss peak and onsets of transition (T_i and T_{ii}) of SPI resins.

Resin	Initial Deriv. Weight Loss Peak		First onset		Second onset	
	T (°C)	Weight loss (%)	T_i (°C)	Weight loss (%)	T_{ii} (°C)	Weight loss (%)
SPI12-120	162.4 ± 1.0	11.6 ± 2.0	156.5 ± 4.3	9.5 ± 3.1	241.4 ± 2.1	21.6 ± 1.3
SPI12-140	181.2 ± 1.9	6.9 ± 1.1	169.7 ± 4.2	4.7 ± 0.5	240.4 ± 1.4	13.1 ± 1.0
SPI9	200.3 ± 18.7	8.6 ± 1.1	—	—	260.5 ± 3.2	15.8 ± 3.2

$N = 3$.

4.7.5 TGA of composites

TGA thermograms and the extrapolated onset temperatures of degradation of the RS/JFa/SPI composites are depicted in **Figure 50**, and data are presented in **Table 27**. The thermograms show a similar behavior to that obtained for SPI12-140 resins as can be seen in their T_d values (Table 27) which are between 239.4–246.1°C. There is a slight increase in T_d for the T60 composites as compared to other composites and SPI12-140 resin. The char content of the composites T40, T50, and T60 resins were 33.3, 30.8, and 27.6%, respectively. It shows about 3% decrease with 10 wt% increase in fiber content, corresponding to the high cellulose content in JF and high hemicellulose content in RS.

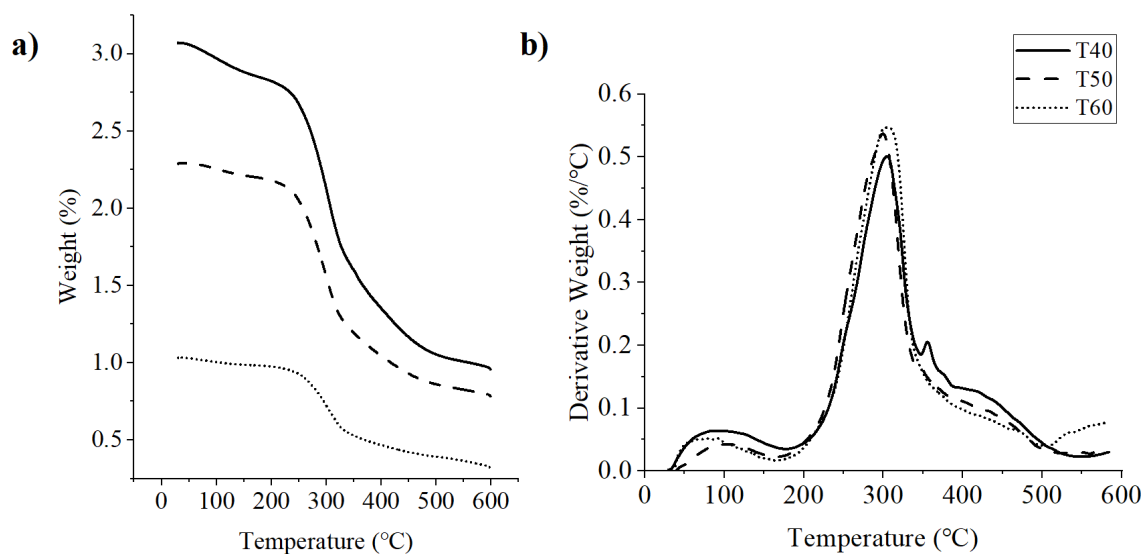


Figure 50. TGA thermograms of RS/JFa/SPI composites, showing a) weight loss plot and b) derivative weight loss plots with respect to temperature.

Table 27. TGA Initial weight loss peak and onset of degradation (T_d) of RS/JFa/SPI composites.

Composite	Onset of Degradation	
	T_d (°C)	Weight Loss (%)
T40	239.4 ± 3.9	11.9 ± 0.4
T50	240.0 ± 1.4	11.9 ± 2.6
T60	246.1 ± 1.4	10.8 ± 0.6

$N = 3$.

4.7.6 ATR-FTIR analysis of alkali-treated DPT fibers

FTIR analysis was performed to characterize the chemical changes occurring in DPT fiber's surface with respect to NaOH treatment time. The FTIR spectra of untreated and alkali treated DPT fibers are shown in **Figure 51**. Absorption peaks at around 3660–2900, ~1724, and 1229 cm^{-1} correspond to the vibrations of bond stretching for O–H and C–H, C=O, and C–O respectively.^{162,163} The polysaccharide OH and CH peak range (3660–2900 cm^{-1}) was found to increase in intensity as fibers were treated for longer time periods. This indicates more effective removal of contaminants including lignin and, thus, giving higher exposure to cellulose and/or hemicellulose. While it is expected that NaOH also removes hemicelluloses,^{105,164} it is difficult to assert that conclusion since carbonyl group intensities increased with treatment time. This can mean that (under this mild NaOH treatment) as hemicelluloses are being removed, higher surfaces of cellulose are actively being exposed along with, perhaps, some lignin. Achieving a higher cellulose content is true especially when comparing the tensile results of nontreated and treated DPT fibers. The observed increase in stiffness and strength after NaOH treatment is directly related to a higher cellulose content.

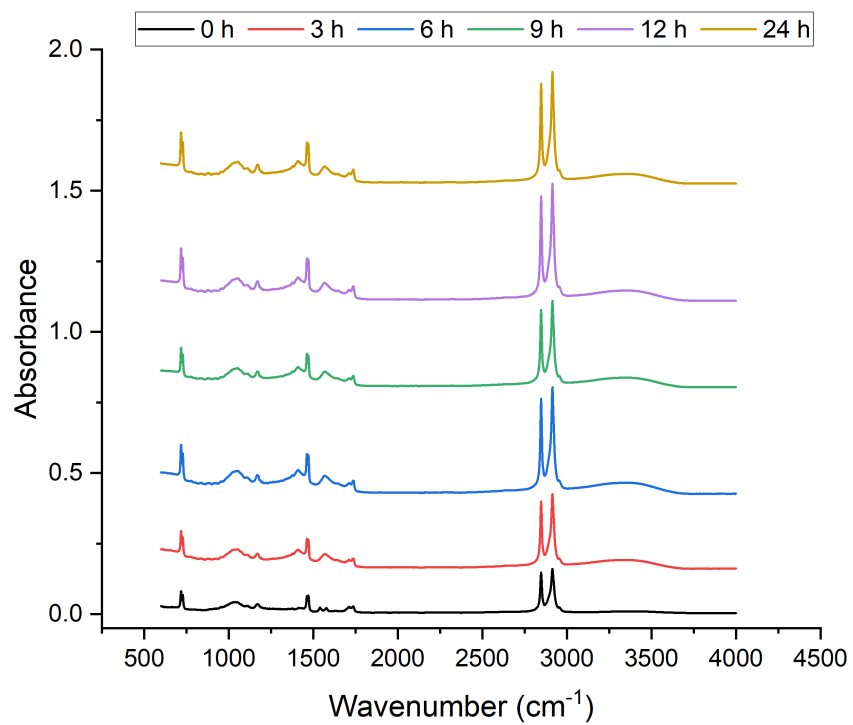


Figure 51. ATR-FTIR spectra of untreated and alkali treated DPT fibers at different treatment times.

CHAPTER 5: CONCLUSIONS

Commercially viable hybrid green composites were fabricated following green chemistry practices. The main components of the composites (i.e., resin and reinforcement) were both plant derived. SPI was alkali-modified then crosslinked with 10 wt% glutaraldehyde and plasticized with 5 wt% D-sorbitol. High volumes of randomly oriented RS at variant lengths were needle-felted into JFa platforms, thus, interlacing the fibers into cohesive hybrid RS/JFa reinforcement mats. Each mat was impregnated with precured SPI resin at three different fiber weight fractions (namely, 40, 50, and 60%) then hot-pressed to fabricate single-layered (S-type) or triple-layered (T-type) composites.

The following conclusions were deduced based on the hygroscopic, mechanical, thermal, and interfacial characterizations that were conducted throughout the course of this study.

Some hybrid composites, e.g. T60, lacked resin content. This was a consequence of the low densities of natural fibers, particularly those of RS. Low density fibers have high relative surface areas, hence, they demand higher resin mass to completely wet the fibers. This low-density feature gave rise to fiber-fiber interactions which turned out to be very prominent, considering for instance, UTS of the composites which always occurred far beyond IFSS, and the fiber-bundle pullout observed from SEM fracture analyses. The primary goal to incorporate high masses of RS into the composites—while it had demonstrated successful needle-felting practices—cost the composites in terms of their mechanical strength and stiffness. The distortion of JFa woven biaxial structure in

addition to the random orientations /lengths of RS provided more load-sharing interfaces in the composite systems but induced structural defects and voids.

IFSS was found to be weak. This may have shifted the load-bearing responsibility towards the resins to some extent. Meaning, the failure majorly occurred at the interface and limited the efficiency of resin-to-reinforcement load transfer, particularly for T60 composites. Weak IFSS was the prime factor in the inverse relationship obtained between increasing fiber content and mechanical properties (i.e., E_y , UTS, E_f , UFS, and storage modulus). In addition, it widened the gap between theoretical tensile properties (predicted by the simple ROHM) and experimental tensile results. **Figure 52** clearly illustrates the gap between theoretical and experimental E_y and UTS, in both warp and weft directions. As an example, E_y experimental results in the warp were 28.5 to 66.4% lower than predicted; that same mismatch was found for UTS in the warp to be between 47.8 and 66.7%. Another factor contributing to this gap was the hydrophilic nature of both the SPI resins (primarily) and cellulosic fibers. Water absorption mass gains were maintained at very similar values for T40, T50, and T60 (9.9, 10.1, and 11.8%, respectively) composites. While thickness gains were found to increase with increased fiber load: 10.4, 12.9, and 22.6% for T40, T50, and T60 composites. This indicates that increased fiber content induced further structural defects and revealed the inability of the resins to wet such volumes of fibers.

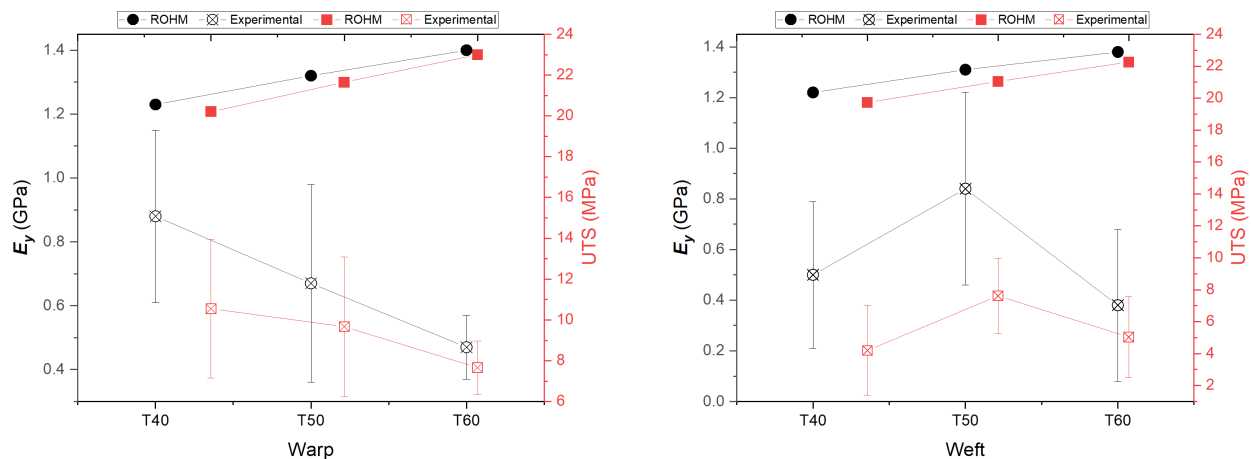


Figure 52. Experimental tensile properties (E_y and UTS) of T-type composites versus theoretical predictions based on ROHM, in two directions, warp (left) and weft (right).

Globular SPI resins were denatured using high alkali conditions in order to improve water-solubility and reduce the precured resin's viscosity to enhance impregnation into the complex hybrid fiber structure. The high alkalinity (pH 12.5) may have affected the resin properties. Especially since reducing the pH level to 9.5 achieved similar crosslinking degrees and mechanical properties to SPI12-140 at a curing temperature that was 20 degrees lower (120°C for pH 9.5 and 140°C for pH 12.5).

Resin properties were limiting the composites' strength, evidenced by how UTS was statistically equal for T-type composites in the warp, and was similar in the weft direction. The relatively weak IFSS could be compensated for by increasing the thermoset resin content, as 40 wt% resulted in relatively the highest E_y , UTS, E_f , and UFS.

Random lengths/orientations of RS and felting dispersed properties across directions. A higher hybridization effect (determined by the deviation from UTS elongation away from JFa's) was observed to be higher in warp than weft, in triple-layered than single-layered composites, and as fiber content increased. Flexural results

showed the effect of specimen thickness and how well plasticized resins can transfer the loads more uniformly.

These composites, using a rice straw waste, have properties that can be applied in low-mechanical resisting structures such as paneling, housing, or packaging. They will be a good replacement for particle boards. The techniques implemented and the results obtained demonstrated that even the weak lignocellulosic waste can be effectively utilized in fabricating green composites.

CHAPTER 6: FUTURE SUGGESTIONS

There is much room to capitalize on this work for further implementation in green composite applications. To better understand the changes in composite structure and properties, it would be beneficial to quantify the densities of constituents and of final composites. Hence, working on further increasing that density would be helpful, through manufacturing or chemical techniques, since hybridization of RS with JFa is expected to produce large amounts of voids. These voids directly affect composite properties as well as testing consistency, resulting in higher variation. One way to increase the ratio of crystalline cellulose per unit volume of composite is the chemical treatment of fibers using benign alkali/acids for longer periods of time or using higher concentrations. This technique removes amorphous materials (i.e., hemicellulose, lignin, pectin) and subsequently increases the density of the composites. It is also easy to implement and could be easily designed in a way that complies to the principles of green chemistry.

The incorporation of lighter plasticizers as to avoid excessive chain sliding or agglomeration of the non-chemically bonded plasticizers in the resin mix would be beneficial. It also ensures homogeneous dispersion across the resin and would enhance the consistency of results.

Mixing SPI with non-petroleum-based hydrophobic monomers to produce a less hydrophilic resin mix, as opposed to the chemically costly techniques (i.e., compatibilization, grafting).

Replacing glutaraldehyde with less toxic crosslinkers, such as plant-derived aldehydes (e.g. vanillin or cinnamaldehyde) for applications where pesticide attack is not

a concern. However, it is understood that such toxicity can protect from microbial-induced structural defects.

Microbead tests can be further optimized by customizing a fixture that fits the space provided by the Instron universal tester. One of the main difficulties of this test was maintaining axial alignment between the specimen, the micro-vice, and the Instron extension clamps.

The hybrid composites' mechanical properties, especially flexural, can be further enhanced by increasing the layers to beyond three. If properly interlaced and cured, extra layers can help averaging out structural defects such as voids, microcracks, fiber discontinuities, and so on. A higher thickness can also lead to flexural strengths.

Fabricating green unidirectional layered DPT/SPI composites, since DPT leaflet waste showed promising mechanical properties. For instance, mildly mercerized DPT fibers (1.25 M NaOH for 12 h) showed an enhancement in E_y and UTS from 6.5 ± 2.5 to 17.1 ± 9.1 GPa (163% increase) and 51.9 ± 12.7 to 107 ± 44.6 MPa (106% increase), respectively.

REFERENCES

1. Netravali, A. *Advanced Green Composites*. vol. 16 (John Wiley & Sons, Inc., 2007).
2. Callister, W. D. and Rethwisch, D. G. *Materials Science and Engineering 9th Edition. Computing in Science & Engineering* (2014). doi:10.1016/j.str.2011.03.005.
3. Bakis, C. E., Bank, L. C., Brown, V. L., Cosenza, E., Davalos, J. F., Lesko, J. J., Machida, A., Rizkalla, S. H. and Triantafillou, T. C. Fiber-Reinforced Polymer Composites for Construction - State-of-the-Art Review. *Perspect. Civ. Eng. Commem. 150th Aniv. Am. Soc. Civ. Eng.* **6**, 369–383 (2003).
4. Yashas Gowda, T. G., Sanjay, M. R., Subrahmanya Bhat, K., Madhu, P., Senthamaraiannan, P. and Yogesha, B. Polymer matrix-natural fiber composites: An overview. *Cogent Eng.* **5**, 1–13 (2018).
5. Faruk, O., Bledzki, A. K., Fink, H. and Sain, M. Biocomposites reinforced with natural fibers : 2000 – 2010. *Prog. Polym. Sci.* **37**, 1552–1596 (2012).
6. Netravali, A. N. and Chabba, S. Composites get greener. *Mater. Today* **6**, 22–29 (2003).
7. Chamas, A., Moon, H., Zheng, J., Qiu, Y., Tabassum, T., Jang, J. H., Abu-Omar, M., Scott, S. L. and Suh, S. Degradation Rates of Plastics in the Environment. *ACS Sustain. Chem. Eng.* **8**, 3494–3511 (2020).
8. Zheng, J. and Suh, S. Strategies to reduce the global carbon footprint of plastics. *Nat. Clim. Chang.* **9**, 374–378 (2019).
9. Geyer, R., Jambeck, J. R. and Law, K. L. Production, use, and fate of all plastics ever made. *Sci. Adv.* **3**, 25–29 (2017).
10. Verma, R., Vinoda, K. S., Papireddy, M. and Gowda, A. N. S. Toxic Pollutants from Plastic Waste- A Review. *Procedia Environ. Sci.* **35**, 701–708 (2016).
11. Mohanty, A. K., Vivekanandhan, S., Pin, J. M. and Misra, M. Composites from renewable and sustainable resources: Challenges and innovations. *Science (80-.)*. **362**, 536–542 (2018).
12. Alay, E., Duran, K. and Korlu, A. A sample work on green manufacturing in textile industry. *Sustain. Chem. Pharm.* **3**, 39–46 (2016).
13. Eryuruk, S. H. Greening of the textile and clothing industry. *Fibres Text. East. Eur.* **95**, 22–27 (2012).
14. Jia, L., Evans, S. and Linden, S. van der. Motivating actions to mitigate plastic pollution. *Nat. Commun.* **10**, 9–11 (2019).
15. Luo, S. and Netravali, A. N. Mechanical and thermal properties of environment-friendly 'green' composites made from pineapple leaf fibers and poly(hydroxybutyrate-co-valerate) resin. *Polym. Compos.* **20**, 367–378 (1999).

16. Luo, S. and Netravali, A. N. Interfacial and mechanical properties of environment-friendly “green” composites made from pineapple fibers and poly(hydroxybutyrate-co-valerate) resin. *J. Mater. Sci.* **34**, 3709–3719 (1999).
17. Bayart, M., Gauvin, F., Foruzanmehr, M. R., Elkoun, S. and Robert, M. Mechanical and moisture absorption characterization of PLA composites reinforced with nano-coated flax fibers. *Fibers Polym.* **18**, 1288–1295 (2017).
18. Hossain, M. K., Dewan, M. W., Hosur, M. and Jeelani, S. Mechanical performances of surface modified jute fiber reinforced biopol nanophased green composites. *Compos. Part B Eng.* **42**, 1701–1707 (2011).
19. Dashtizadeh, Z., Khalina, A., Cardona, F. and Lee, C. H. Mechanical Characteristics of Green Composites of Short Kenaf Bast Fiber Reinforced in Cardanol. *Adv. Mater. Sci. Eng.* **2019**, (2019).
20. Totaro, G., Sisti, L., Fiorini, M., Lancellotti, I., Andreola, F. N. and Saccani, A. Formulation of Green Particulate Composites from PLA and PBS Matrix and Wastes Deriving from the Coffee Production. *J. Polym. Environ.* **27**, 1488–1496 (2019).
21. Sangregorio, A., Guigo, N., van der Waal, J. C. and Sbirrazzuoli, N. All ‘green’ composites comprising flax fibres and humins’ resins. *Compos. Sci. Technol.* **171**, 70–77 (2019).
22. Deka, H., Misra, M. and Mohanty, A. Renewable resource based ‘all green composites’ from kenaf biofiber and poly(furfuryl alcohol) bioresin. *Ind. Crops Prod.* **41**, 94–101 (2013).
23. Shih, Y. F., Chang, W. C., Liu, W. C., Lee, C. C., Kuan, C. S. and Yu, Y. H. Pineapple leaf/ recycled disposable chopstick hybrid fiber-reinforced biodegradable composites. *J. Taiwan Inst. Chem. Eng.* **45**, 2039–2046 (2014).
24. Wattanakornsiri, A., Pachana, K., Kaewpirom, S., Traina, M. and Migliaresi, C. Preparation and Properties of Green Composites Based on Tapioca Starch and Differently Recycled Paper Cellulose Fibers. *J. Polym. Environ.* **20**, 801–809 (2012).
25. Anastas, P. T. and Warner, J. C. *Green chemistry: theory and practice*. (Oxford University Press, 1998).
26. Anastas, P. and Eghbali, N. Green Chemistry: Principles and Practice. *Chem. Soc. Rev.* **39**, 301–312 (2010).
27. Abdul Khalil, H. P. S., Bhat, A. H. and Ireana Yusra, A. F. Green composites from sustainable cellulose nanofibrils: A review. *Carbohydr. Polym.* **87**, 963–979 (2012).
28. Burrola-Núñez, H., Herrera-Franco, P. J., Rodríguez-Félix, D. E., Soto-Valdez, H. and Madera-Santana, T. J. Surface modification and performance of jute fibers as reinforcement on polymer matrix: an overview. *J. Nat. Fibers* **16**, 944–960 (2019).
29. Kiliñç, A. Ç., Durmuşkahya, C. and Seydibeyoğlu, M. Ö. Natural fibers. in *Fiber Technology for Fiber-Reinforced Composites* 209–235 (Elsevier, 2017). doi:10.1016/B978-0-08-101871-2.00010-2.

30. Truax, T. R. *The gluing of wood*. (U.S. Dept. of Agriculture, 1929). doi:10.5962/bhl.title.108492.
31. Liu, C., Zhang, Y., Li, X., Luo, J., Gao, Q. and Li, J. "Green" bio-thermoset resins derived from soy protein isolate and condensed tannins. *Ind. Crops Prod.* **108**, 363–370 (2017).
32. Yang, Z., Peng, H., Wang, W. and Liu, T. Crystallization behavior of poly(ϵ -caprolactone)/layered double hydroxide nanocomposites. *J. Appl. Polym. Sci.* **116**, 2658–2667 (2010).
33. USDA Economic Research Service: Soybeans & Oil Crops. <https://www.ers.usda.gov/topics/crops/soybeans-oil-crops/>.
34. Reddy, N. A review on completely biodegradable composites developed using soy-based matrices. *J. Reinf. Plast. Compos.* **34**, 1457–1475 (2015).
35. Netravali, A. N., Huang, X. and Mizuta, K. Advanced 'green' composites. *Adv. Compos. Mater.* **16**, 269–282 (2007).
36. Lodha, P. and Netravali, A. N. Characterization of interfacial and mechanical properties of 'green' composites with soy protein isolate and ramie fiber. *J. Mater. Sci.* **37**, 3657–3665 (2002).
37. Petruccelli, S. and Añón, M. C. Soy Protein Isolate Components and Their Interactions. *J. Agric. Food Chem.* **43**, 1762–1767 (1995).
38. Silva, N. H. C. S., Vilela, C., Marrucho, I. M., Freire, C. S. R., Pascoal Neto, C. and Silvestre, A. J. D. Protein-based materials: From sources to innovative sustainable materials for biomedical applications. *J. Mater. Chem. B* **2**, 3715–3740 (2014).
39. Song, F., Tang, D. L., Wang, X. L. and Wang, Y. Z. Biodegradable soy protein isolate-based materials: A review. *Biomacromolecules* **12**, 3369–3380 (2011).
40. Wang, Y., Deng, L. and Fan, Y. Preparation of Soy-Based Adhesive Enhanced by Waterborne Polyurethane: Optimization by Response Surface Methodology. *Adv. Mater. Sci. Eng.* **2018**, (2018).
41. Chabba, S. and Netravali, A. N. 'Green' composites part 1: Characterization of flax fabric and glutaraldehyde modified soy protein concentrate composites. *J. Mater. Sci.* **40**, 6263–6273 (2005).
42. Hettiarachchy, N. S., Kalapathy, U. and Myers, D. J. Alkali-modified soy protein with improved adhesive and hydrophobic properties. *J. Am. Oil Chem. Soc.* **72**, 1461–1464 (1995).
43. KM, D. and VK, S. Soy Protein Based Green Composite: A Review. *Res. Rev. J. Mater. Sci.* **05**, 66–77 (2017).
44. Gennadios, A., Brandenburg, A. H., Weller, C. L. and Testin, R. F. Effect of pH on Properties of Wheat Gluten and Soy Protein Isolate Films. *J. Agric. Food Chem.* **41**, 1835–1839 (1993).

45. Dastidar, T. G., Netravali, A. N., Ghosh Dastidar, T. and Netravali, A. N. A soy flour based thermoset resin without the use of any external crosslinker. *Green Chem.* **15**, 3243–3251 (2013).
46. Yasir, S. B. M., Sutton, K. H., Newberry, M. P., Andrews, N. R. and Gerrard, J. A. The impact of Maillard cross-linking on soy proteins and tofu texture. *Food Chem.* **104**, 1502–1508 (2007).
47. Lubasova, D., Mullerova, J. and Netravali, A. N. Water-resistant plant protein-based nanofiber membranes. *J. Appl. Polym. Sci.* **132**, 1–9 (2015).
48. Patil, N. V, Rahman, M. M. and Netravali, A. N. “Green” composites using bioresins from agro-wastes and modified sisal fibers. *Polym. Compos.* **40**, 99–108 (2019).
49. Huang, X. and Netravali, A. Biodegradable green composites made using bamboo micro/nano-fibrils and chemically modified soy protein resin. *Compos. Sci. Technol.* **69**, 1009–1015 (2009).
50. Lodha, P. and Netravali, A. N. Characterization of phytigel® modified soy protein isolate resin and unidirectional flax yarn reinforced ‘Green’ composites. *Polym. Compos.* **26**, 647–659 (2005).
51. Kim, J. R. and Netravali, A. N. Comparison of thermoset soy protein resin toughening by natural rubber and epoxidized natural rubber. *J. Appl. Polym. Sci.* **134**, 1–13 (2017).
52. Kim, J. R. and Netravali, A. N. Self-Healing Properties of Protein Resin with Soy Protein Isolate-Loaded Poly(d,l-lactide-co-glycolide) Microcapsules. *Adv. Funct. Mater.* **26**, 4786–4796 (2016).
53. Patil, N. V. and Netravali, A. N. Enhancing Strength of Wool Fiber Using a Soy Flour Sugar-Based ‘green’ Cross-linker. *ACS Omega* **4**, 5392–5401 (2019).
54. Lodha, P. and Netravali, A. N. Thermal and mechanical properties of environment-friendly ‘green’ plastics from stearic acid modified-soy protein isolate. *Ind. Crops Prod.* **21**, 49–64 (2005).
55. Lodha, P. and Netravali, A. N. Characterization of stearic acid modified soy protein isolate resin and ramie fiber reinforced ‘green’ composites. *Compos. Sci. Technol.* **65**, 1211–1225 (2005).
56. Ghosh Dastidar, T. and Netravali, A. Cross-linked waxy maize starch-based ‘green’ composites. *ACS Sustain. Chem. Eng.* **1**, 1537–1544 (2013).
57. Patil, N. V. and Netravali, A. N. Microfibrillated cellulose-reinforced nonedible starch-based thermoset biocomposites. *J. Appl. Polym. Sci.* **133**, 1–9 (2016).
58. Fosket, D. E. *Plant growth and development : a molecular approach*. (Academic Press, 1994).
59. Sorieul, M., Dickson, A., Hill, S. J. and Pearson, H. *Plant fibre: Molecular structure and biomechanical properties, of a complex living material, influencing its deconstruction towards a*

- biobased composite. Materials* vol. 9 (2016).
60. Rytioja, J., Hildén, K., Yuzon, J., Hatakka, A., de Vries, R. P. and Mäkelä, M. R. Plant-Polysaccharide-Degrading Enzymes from Basidiomycetes. *Microbiol. Mol. Biol. Rev.* **78**, 614–649 (2014).
 61. Han, J. S. and Rowell, J. S. *Paper and Composites from Agro-Based Resources. Chapter 5: Chemical Composition of Fibers* (CRC Press, Inc., 1997).
 62. Mwaikambo, L. Y. and Ansell, M. P. Mechanical properties of alkali treated plant fibres and their potential as reinforcement materials. I. hemp fibres. *J. Mater. Sci.* **41**, 2483–2496 (2006).
 63. Ramezani, M. G. and Golchinfar, B. Mechanical Properties of Cellulose Nanocrystal (CNC) Bundles: Coarse-Grained Molecular Dynamic Simulation. *J. Compos. Sci.* **3**, 57 (2019).
 64. Wu, X., Wagner, R., Raman, A., Moon, R. and Martini, A. Elastic deformation mechanics of cellulose nanocrystals. *TMS Annu. Meet.* **2**, 689–696 (2010).
 65. Wu, X., Moon, R. J. and Martini, A. Tensile strength of I β crystalline cellulose predicted by molecular dynamics simulation. *Cellulose* **21**, 2233–2245 (2014).
 66. Aulin, C. Novel oil resistant cellulosic materials. (Royal Institute of Technology, 2009).
 67. Fuqua, M. A., Huo, S. and Ulven, C. A. Natural fiber reinforced composites. *Polym. Rev.* **52**, 259–320 (2012).
 68. Nishiyama, Y., Sugiyama, J., Chanzy, H. and Langan, P. Crystal Structure and Hydrogen Bonding System in Cellulose I α from Synchrotron X-ray and Neutron Fiber Diffraction. *J. Am. Chem. Soc.* **125**, 14300–14306 (2003).
 69. Huber, T., Müssig, J., Curnow, O., Pang, S., Bickerton, S. and Staiger, M. P. A critical review of all-cellulose composites. *J. Mater. Sci.* **47**, 1171–1186 (2012).
 70. Scheller, H. V. and Ulvskov, P. Hemicelluloses. *Annu. Rev. Plant Biol.* **61**, 263–289 (2010).
 71. Cousins, W. J. Young's modulus of hemicellulose as related to moisture content. *Wood Sci. Technol.* **12**, 161–167 (1978).
 72. Chatterjee, S., Clingenpeel, A., McKenna, A., Rios, O. and Johs, A. Synthesis and characterization of lignin-based carbon materials with tunable microstructure. *RSC Adv.* **4**, 4743–4753 (2014).
 73. Liu, Q., Luo, L. and Zheng, L. Lignins: Biosynthesis and biological functions in plants. *Int. J. Mol. Sci.* **19**, (2018).
 74. Fagerstedt, K. V., Kukkola, E. M., Koistinen, V. V. T., Takahashi, J. and Marjamaa, K. Cell wall lignin is polymerised by class III secretable plant peroxidases in Norway spruce. *J. Integr. Plant Biol.* **52**, 186–194 (2010).

75. Lu, Y., Lu, Y.-C., Hu, H.-Q., Xie, F.-J., Wei, X.-Y. and Fan, X. Structural Characterization of Lignin and Its Degradation Products with Spectroscopic Methods. (2017) doi:10.1155/2017/8951658.
76. Mohnen, D. Pectin structure and biosynthesis. *Curr. Opin. Plant Biol.* **11**, 266–277 (2008).
77. Ochoa-Villarreal, M., Aispuro-Hernandez, E., Vargas-Arispuro, I. and Ngel, M. Plant Cell Wall Polymers: Function, Structure and Biological Activity of Their Derivatives. in *Polymerization 13* (InTech, 2012). doi:10.5772/46094.
78. Sreekala, M. S., Kumaran, M. G. and Thomas, S. Water sorption in oil palm fiber reinforced phenol formaldehyde composites. *Compos. - Part A Appl. Sci. Manuf.* **33**, 763–777 (2002).
79. Mishra, S., Mohanty, A. K., Drzal, L. T., Misra, M., Parija, S., Nayak, S. K. and Tripathy, S. S. Studies on mechanical performance of biofibre/glass reinforced polyester hybrid composites. *Compos. Sci. Technol.* **63**, 1377–1385 (2003).
80. Patel, V. A. and Parsania, P. H. Performance Evaluation of Alkali and Acrylic Acid Treated-Untreated Jute Composites of Mixed Epoxy-Phenolic Resins. *J. Reinf. Plast. Compos.* **29**, 725–730 (2010).
81. Islam, M. S., Pickering, K. L. and Foreman, N. J. Influence of accelerated ageing on the physico-mechanical properties of alkali-treated industrial hemp fibre reinforced poly(lactic acid) (PLA) composites. *Polym. Degrad. Stab.* **95**, 59–65 (2010).
82. Sahu, P. and Gupta, M. K. A review on the properties of natural fibres and its bio-composites: Effect of alkali treatment. *Proc. Inst. Mech. Eng. Part L J. Mater. Des. Appl.* **234**, 198–217 (2020).
83. Silva, C. G., Campini, P. A. L., Rocha, D. B. and Rosa, D. S. The influence of treated eucalyptus microfibers on the properties of PLA biocomposites. *Compos. Sci. Technol.* **179**, 54–62 (2019).
84. Chanda, A. K., Hazra, A., Praveen Kumar, M., Neogi, S. and Neogi, S. Chemical treatments of rice husk filler and jute fiber for the use in green composites. *Fibers Polym.* **16**, 902–910 (2015).
85. Ismail, S. H. and Abu Bakar, A. Effects of chemical modification of paper sludge filled Polypropylene (PP)/Ethylene Propylene Diene Terpolymer (EPDM) composites. *J. Reinf. Plast. Compos.* **25**, 43–58 (2006).
86. Alix, S., Philippe, E., Bessadok, A., Lebrun, L., Morvan, C. and Marais, S. Effect of chemical treatments on water sorption and mechanical properties of flax fibres. *Bioresour. Technol.* **100**, 4742–4749 (2009).
87. Sreekala, M. S. and Thomas, S. Effect of fibre surface modification on water-sorption characteristics of oil palm fibres. *Compos. Sci. Technol.* **63**, 861–869 (2003).
88. Lee, T. S., Choi, H. Y., Choi, H. N., Lee, K. Y., Kim, S. H., Lee, S. G. and Yong, D. K. Effect of surface treatment of ramie fiber on the interfacial adhesion of ramie/acetlylated

- epoxidized soybean oil (AESO) green composite. *J. Adhes. Sci. Technol.* **27**, 1335–1347 (2013).
89. Saenghirunwattana, P., Noomhorm, A. and Rungsardthong, V. Mechanical properties of soy protein based 'green' composites reinforced with surface modified cornhusk fiber. *Ind. Crops Prod.* **60**, 144–150 (2014).
 90. Bledzki, A. and Gassan, J. Composites reinforced with cellulose based fibres. *Prog. Polym. Sci.* **24**, 221–274 (1999).
 91. Das, S., Saha, A. K., Choudhury, P. K., Basak, R. K., Mitra, B. C., Todd, T., Lang, S. and Rowell, R. M. Effect of steam pretreatment of jute fiber on dimensional stability of jute composite. *J. Appl. Polym. Sci.* **76**, 1652–1661 (2000).
 92. Mesquita, R. G. de A., César, A. A. da S., Mendes, R. F., Mendes, L. M., Marconcini, J. M., Glenn, G. and Tonoli, G. H. D. Polyester Composites Reinforced with Corona-Treated Fibers from Pine, Eucalyptus and Sugarcane Bagasse. *J. Polym. Environ.* **25**, 800–811 (2017).
 93. Mukhopadhyay, S. and Figueiro, R. Physical modification of natural fibers and thermoplastic films for composites - A review. *J. Thermoplast. Compos. Mater.* **22**, 135–162 (2009).
 94. Belgacem, M. N., Bataille, P. and Sapiéha, S. Effect of corona modification on the mechanical properties of polypropylene/cellulose composites. *J. Appl. Polym. Sci.* **53**, 379–385 (1994).
 95. Valášek, P., Müller, M. and Šleger, V. Influence of plasma treatment on mechanical properties of cellulose-based fibres and their interfacial interaction in composite systems. *BioResources* **12**, 5449–5461 (2017).
 96. Gibeop, N., Lee, D. W., Prasad, C. V., Toru, F., Kim, B. S. and Song, J. Il. Effect of plasma treatment on mechanical properties of jute fiber/poly (lactic acid) biodegradable composites. *Adv. Compos. Mater.* **22**, 389–399 (2013).
 97. Sari, P. S., Thomas, S., Spatenka, P., Ghanam, Z. and Jenikova, Z. Effect of plasma modification of polyethylene on natural fibre composites prepared via rotational moulding. *Compos. Part B Eng.* **177**, 107344 (2019).
 98. Nakamura, K., Hatakeyama, T. and Hatakeyama, H. Studies on Bound Water of Cellulose by Differential Scanning Calorimetry. *Text. Res. J.* **51**, 607–613 (1981).
 99. Netravali, A. N., Henstenburg, R. B., Phoenix, S. L. and Schwartz, P. Interfacial shear strength studies using the single-filament-composite test. I: Experiments on graphite fibers in epoxy. *Polym. Compos.* **10**, 226–241 (1989).
 100. Kalita, D. and Netravali, A. N. Interfaces in Green Composites: A Critical Review. *Rev. Adhes. Adhes.* **3**, 386–443 (2015).
 101. Zini, E. and Scandola, M. Green composites: An overview. *Polym. Compos.* **32**, 1905–1915 (2011).

102. Domínguez-Escribá, L. and Porcar, M. Rice straw management: the big waste. *Biofuels, Bioprod. Biorefining* **4**, 154–159 (2010).
103. Bassyouni, M. and Waheed Ul Hasan, S. The use of rice straw and husk fibers as reinforcements in composites. in *Biofiber Reinforcements in Composite Materials* 385–422 (Elsevier, 2015). doi:10.1533/9781782421276.4.385.
104. Al-Oqla, F. M. and Sapuan, S. M. Natural fiber reinforced polymer composites in industrial applications: Feasibility of date palm fibers for sustainable automotive industry. *J. Clean. Prod.* **66**, 347–354 (2014).
105. Al-Khanbashi, A., Al-Kaabi, K. and Hammami, A. Date palm fibers as polymeric matrix reinforcement: Fiber characterization. *Polym. Compos.* **26**, 486–497 (2005).
106. Siqueira, G., Bras, J. and Dufresne, A. Cellulosic bionanocomposites: A review of preparation, properties and applications. *Polymers (Basel)*. **2**, 728–765 (2010).
107. Jariwala, H. and Jain, P. A review on mechanical behavior of natural fiber reinforced polymer composites and its applications. *J. Reinf. Plast. Compos.* **38**, 441–453 (2019).
108. Summerscales, J., Dissanayake, N. P. J., Virk, A. S. and Hall, W. A review of bast fibres and their composites. Part 1 - Fibres as reinforcements. *Compos. Part A Appl. Sci. Manuf.* **41**, 1329–1335 (2010).
109. Hiziroglu, S., Bauchongkol, P., Fueangvivat, V., Soontonbura, W. and Jarusombuti, S. Selected properties of medium density fiberboard (MDF) panels made from bamboo and rice straw. *For. Prod. J.* **57**, 46–50 (2007).
110. Ratna Prasad, A. V., Murali Mohan Rao, K., Mohan Rao, K. and Gupta, A. V. S. S. K. S. Tensile and impact behaviour of rice straw-polyester composites. *Indian J. Fibre Text. Res.* **32**, 399–403 (2007).
111. Liu, Z., Xu, A. and Long, B. Energy from Combustion of Rice Straw: Status and Challenges to China. *Energy Power Eng.* **03**, 325–331 (2011).
112. Nguyen, H. Van, Nguyen, C. D., Tran, T. Van, Hau, H. D., Nguyen, N. T. and Gummert, M. Energy efficiency, greenhouse gas emissions, and cost of rice straw collection in the mekong river delta of vietnam. *F. Crop. Res.* **198**, 16–22 (2016).
113. Das, B., Chakrabarti, K., Tripathi, S. and Chakraborty, A. Review of Some Factors Influencing Jute Fiber Quality. *J. Nat. Fibers* **11**, 268–281 (2014).
114. Mohanty, A. K. and Misra, M. Studies on Jute Composites—a Literature Review. *Polym. Plast. Technol. Eng.* **34**, 729–792 (1995).
115. Van Soest, P. J. Rice straw, the role of silica and treatments to improve quality. *Anim. Feed Sci. Technol.* **130**, 137–171 (2006).
116. Gadde, B., Menke, C. and Wassmann, R. Rice straw as a renewable energy source in India, Thailand, and the Philippines: Overall potential and limitations for energy contribution

- and greenhouse gas mitigation. *Biomass and Bioenergy* **33**, 1532–1546 (2009).
117. Ren, J., Yu, P. and Xu, X. Straw utilization in China-status and recommendations. *Sustain.* **11**, 1–17 (2019).
 118. Ranjan, C., Ahmed, Z., Raj Kumar, S., Kumar, A., Kumar, A. and Kumar, K. Fabrication and strength analysis of rice straw fibers reinforced epoxy biodegradable composite. *Mater. Today Proc.* 2–6 (2020) doi:10.1016/j.matpr.2020.08.299.
 119. Khandanlou, R., Ahmad, M. B., Shamel, K., Hussein, M. Z., Zainuddin, N. and Kalantari, K. Effect of unmodified rice straw on the properties of rice straw/polycaprolactone composites. *Res. Chem. Intermed.* **41**, 6371–6384 (2015).
 120. Bassyouni, M., Taha, I., Abdel-Hamid, S. M. S. and Steuernagel, L. Physico-mechanical properties of chemically treated polypropylene rice straw bio-composites. *J. Reinf. Plast. Compos.* **31**, 303–312 (2012).
 121. Ming-Zhu, P., Chang-Tong, M., Xu-Bing, Z. and Yun-Lei, P. Effects of rice straw fiber morphology and content on the mechanical and thermal properties of rice straw fiber-high density polyethylene composites. *J. Appl. Polym. Sci.* **121**, 2900–2907 (2011).
 122. Ortiz-Urbe, N., Salomón-Torres, R. and Krueger, R. Date palm status and perspective in Mexico. *Agric.* **9**, 1–15 (2019).
 123. Ghori, W., Saba, N., Jawaid, M. and Asim, M. A review on date palm (Phoenix dactylifera) fibers and its polymer composites. *IOP Conf. Ser. Mater. Sci. Eng.* **368**, (2018).
 124. Food and Agriculture Organization of the United Nations. *FAOSTAT Crops* <http://www.fao.org/faostat/en/#data/QC> (2020).
 125. Chandrasekaran, M. and Bahkali, A. H. Valorization of date palm (Phoenix dactylifera) fruit processing by-products and wastes using bioprocess technology - Review. *Saudi J. Biol. Sci.* **20**, 105–120 (2013).
 126. Khanlou, H. M., Hall, W., Woodfield, P., Summerscales, J. and Francucci, G. The mechanical properties of flax fibre reinforced poly(lactic acid) bio-composites exposed to wet, freezing and humid environments. doi:10.1177/0021998317714857.
 127. Zamri, M. H., Akil, H. M., Bakar, A. A., Ishak, Z. A. M. and Cheng, L. W. Effect of water absorption on pultruded jute/glass fiber-reinforced unsaturated polyester hybrid composites. *J. Compos. Mater.* **46**, 51–61 (2012).
 128. Pan, N. and Brookstein, D. Physical properties of twisted structures. II. Industrial yarns, cords, and ropes. *J. Appl. Polym. Sci.* **83**, 610–630 (2002).
 129. Rao, Y. and Farris, R. J. Modeling and experimental study of the influence of twist on the mechanical properties of high-performance fiber yarns. *J. Appl. Polym. Sci.* **77**, 1938–1949 (2000).
 130. Jeon, B. S. Evaluation of the structural properties of plain fabrics woven from various fibers

- using Peirce's model. *Fibers Polym.* **13**, 130–134 (2012).
131. Yao, Y., Zhu, D., Zhang, H., Li, G. and Mobasher, B. Tensile Behaviors of Basalt, Carbon, Glass, and Aramid Fabrics under Various Strain Rates. *J. Mater. Civ. Eng.* **28**, 04016081 (2016).
 132. Budtova, T. and Navard, P. Cellulose in NaOH–water based solvents: a review. *Cellulose* **23**, 5–55 (2016).
 133. Krishnaiah, P., Ratnam, C. T. and Manickam, S. Enhancements in crystallinity, thermal stability, tensile modulus and strength of sisal fibres and their PP composites induced by the synergistic effects of alkali and high intensity ultrasound (HIU) treatments. *Ultrason. Sonochem.* **34**, 729–742 (2017).
 134. Kim, J. R. and Netravali, A. N. Self-healing green composites based on soy protein and microfibrillated cellulose. *Compos. Sci. Technol.* **143**, 22–30 (2017).
 135. Mirbagheri, J., Tajvidi, M., Hermanson, J. C. and Ghasemi, I. Tensile properties of wood flour/kenaf fiber polypropylene hybrid composites. *J. Appl. Polym. Sci.* **105**, 3054–3059 (2007).
 136. Fu, S. Y., Xu, G. and Mai, Y. W. On the elastic modulus of hybrid particle/short-fiber/polymer composites. *Compos. Part B Engineering* **33**, 291–299 (2002).
 137. Venkateshwaran, N., Elayaperumal, A. and Sathiya, G. K. Prediction of tensile properties of hybrid-natural fiber composites. *Compos. Part B Eng.* **43**, 793–796 (2012).
 138. Baker, S. Chapter 9: Elastic Behavior of Composites. in *Mechanical properties of materials, processing, and design, lecture notes* (Cornell University, 2020).
 139. Kretsis, G. A review of the tensile, compressive, flexural and shear properties of hybrid fibre-reinforced plastics. *Composites* **18**, 13–23 (1987).
 140. Mansor, M. R., Sapuan, S. M., Zainudin, E. S., Nuraini, A. A. and Hambali, A. Stiffness prediction of hybrid kenaf/glass fiber reinforced polypropylene composites using rule of mixtures (ROM) and rule of hybrid mixtures (RoHM). *J. Polym. Mater.* **30**, 321–334 (2013).
 141. Rouchon, J. Certification of large aircraft composite structures, recent progress and new trends in compliance philosophy. *17th ICAS Congress* vol. 1 1439–1447 (1990).
 142. Lopes, C. S., González, C., Falcó, O., Naya, F., LLorca, J. and Tijs, B. Multiscale virtual testing: the roadmap to efficient design of composites for damage resistance and tolerance. *CEAS Aeronaut. J.* **7**, 607–619 (2016).
 143. Punyamurthy, R., Sampathkumar, D., Bennehalli, B., Ranganagowda, R. P., Badyankal, P. vasudeva and Venkateshappa, S. C. Abaca Fiber Reinforced Hybrid Composites. *Int. J. Appl. Eng. Res.* **9**, 20273–20286 (2014).
 144. Mallick, P. K. and Broutman, L. J. Static and Impact Properties of Laminated Hybrid Composites. *J. Test. Eval.* **5**, 190–200 (1977).

145. Nunna, S., Chandra, P. R., Shrivastava, S. and Jalan, A. K. A review on mechanical behavior of natural fiber based hybrid composites. *J. Reinf. Plast. Compos.* **31**, 759–769 (2012).
146. Kim, H., Okubo, K., Fujii, T. and Takemura, K. Influence of fiber extraction and surface modification on mechanical properties of green composites with bamboo fiber. *J. Adhes. Sci. Technol.* **27**, 1348–1358 (2013).
147. Miller, B., Muri, P. and Rebenfeld, L. A microbond method for determination of the shear strength of a fiber / resin interface. *Compos. Sci. Technol.* **28**, 17–32 (1987).
148. Kelly, A. and Tyson, W. R. Tensile properties of fibre-reinforced metals: Copper / tungsten and copper / molybdenum. *J. Mech. Phys. Solids* **13**, (1965).
149. Kumar, A. and Srivastava, A. Preparation and Mechanical Properties of Jute Fiber Reinforced Epoxy Composites. *Ind. Eng. Manag.* **06**, 4–7 (2017).
150. Huang, X. and Netravali, A. Characterization of flax fiber reinforced soy protein resin based green composites modified with nano-clay particles. *Compos. Sci. Technol.* **67**, 2005–2014 (2007).
151. Gupta, V. and Kothari, V. *Manufactured Fibre Technology*. (1997). doi:10.1007/978-94-011-5854-1.
152. Zhang, J., Mungara, P. and Jane, J. Mechanical and thermal properties of extruded soy protein sheets. *Polymer (Guildf)*. **42**, 2569–2578 (2001).
153. Verbeek, C. J. R. and Van Den Berg, L. E. Extrusion processing and properties of protein-based thermoplastics. *Macromol. Mater. Eng.* **295**, 10–21 (2010).
154. Gupta, M. K. Multi layers glass fibres reinforced epoxy composite: Dynamic mechanical analysis. *Adv. Mater. Proc.* **2**, 518–520 (2017).
155. Huda, M. S., Mohanty, A. K., Drzal, L. T., Schut, E. and Misra, M. 'Green' composites from recycled cellulose and poly(lactic acid): Physico-mechanical and morphological properties evaluation. *J. Mater. Sci.* **40**, 4221–4229 (2005).
156. Liu, X., Dever, M., Fair, N. and Benson, R. S. Thermal and mechanical properties of poly(lactic acid) and poly(ethylene/butylene succinate) blends. *J. Environ. Polym. Degrad.* **5**, 225–235 (1997).
157. Scilingo, A. A. and Añón, M. C. Calorimetric Study of Soybean Protein Isolates: Effect of Calcium and Thermal Treatments. *J. Agric. Food Chem.* **44**, 3751–3756 (1996).
158. Park, S. K., Bae, D. H. and Rhee, K. C. Soy protein biopolymers cross-linked with glutaraldehyde. *JAOCS, J. Am. Oil Chem. Soc.* **77**, 879–884 (2000).
159. Xia, C., Wang, L., Dong, Y., Zhang, S., Shi, S. Q., Cai, L. and Li, J. Soy protein isolate-based films cross-linked by epoxidized soybean oil. *RSC Adv.* **5**, 82765–82771 (2015).
160. Yang, H., Yan, R., Chen, H., Lee, D. H. and Zheng, C. Characteristics of hemicellulose,

- cellulose and lignin pyrolysis. *Fuel* **86**, 1781–1788 (2007).
161. Burhenne, L., Messmer, J., Aicher, T. and Laborie, M. P. The effect of the biomass components lignin, cellulose and hemicellulose on TGA and fixed bed pyrolysis. *J. Anal. Appl. Pyrolysis* **101**, 177–184 (2013).
 162. *Fourier Transform - Materials Analysis*. (InTech, 2012). doi:10.5772/2659.
 163. Huda, M. S., Drzal, L. T., Mohanty, A. K. and Misra, M. Effect of chemical modifications of the pineapple leaf fiber surfaces on the interfacial and mechanical properties of laminated biocomposites. *Compos. Interfaces* **15**, 169–191 (2008).
 164. Fu, D. and Netravali, A. N. Green composites based on avocado seed starch and nano- and micro-scale cellulose. *Polym. Compos.* **41**, 4631–4648 (2020).